SEEKING THE LOCAL CONVERGENCE DEPTH

A Dissertation

Presented to the Faculty of the Graduate School

of Cornell University

in Partial Fulfillment of the Requirements for the Degree of

Doctor of Philosophy

by

Daniel Allen Dale

August 1998

SEEKING THE LOCAL CONVERGENCE DEPTH

Daniel Allen Dale, Ph.D.

Cornell University 1998

We have compiled Tully-Fisher (TF) measurements for 522 late-type galaxies in the fields of 52 rich Abell clusters distributed throughout the sky between $\sim$50 and $200h^{-1}$ Mpc. Galaxy fluxes and rotational velocity widths are determined from I band photometry and optical rotation curves, with the latter data supplemented by HI profiles. The data are applied to the construction of an I band TF template, resulting in a relation with a kinematical zero-point accurate to 0.02 magnitudes. Individual cluster TF relations are referred to the template to compute cluster peculiar motions. The line-of-sight dispersion in the peculiar motions is 341 ± 43 km s^{-1}.

The reflex motion of our Local Group of galaxies is measured with respect to the reference frame defined by our cluster sample and the distant portion of the Giovanelli *et al.* (1998a) cluster set. We find the Local Group motion in this frame to be 564$\pm$113 km s^{-1} in the direction $(l, b) = (267°, 26°) \pm 11°$ when peculiar velocities are weighted according to their errors. After optimizing the dipole calculation to sample equal volumes fairly, the vector is 499 ± 217 km s^{-1} towards $(256°, 45°) \pm 36°$. Both solutions agree, at the 1σ level or better, with the

best estimates for the Local Group motion in the CMB frame. In other words, the cluster sample as a whole moves slowly in the CMB reference frame; the bulk flow of the cluster frame is at most $\sim$200 km s^{-1}. In contrast to recent claims, our results suggest that the bulk of the local peculiar motion stems from relatively nearby mass inhomogeneities.

Finally, we apply the combined sample of our peculiar velocities and the 24 peculiar velocities from Giovanelli *et al.* (1998a) to a test of the putative Hubble bubble recently claimed by Zehavi and coworkers. In contrast to their findings, our data supports a relatively quiescent Hubble flow beyond $\sim 30h^{-1}$ Mpc.

Biographical Sketch

Daniel Allen Dale was born September 26, 1970 near Princeton, Minnesota, a small village on the outskirts of Lake Wobegon. After an early series of head-crackings from literally tripping over his own feet, Danny decided it would be wise to take better care of his brain. This was a small but important step in his desire to study space.

Danny's mother apparently was not as convinced of his cogitative potential. Despite motherly urgings for him to learn the alphabet and how to tie his own shoes before kindergarten, Danny reportedly refused: "Only my *teacher* is supposed to teach me!" His mother was therefore justifiably surprised when his first grade teacher remarked to her, "Danny is so smart he will be able to do whatever he chooses." Convinced that not only the teachers, but now his own mother believed in his ability, Danny thought to himself, "Ok, now it's time to start on my career." This logically led to a requisite viewing of the film *Star Wars*. His enthusiasm for space truly burgeoning at this stage, Danny made another important career move by collecting 92 Star Wars action figures. The rest is history.

Danny supplemented his impressive but raw resume by taking an active interest in school and athletics. A typical day involved seven hours at school, two hours at the baseball field or hockey rink, and time spent with books (eventually falling asleep with the bedroom light on, much to the chagrin of his father). As he grew older, other activities began to interest Danny. He also enjoyed chorus, cross-country running, golf, tennis, and girls, though not necessarily in that order. Danny met Kim in September of 1987 and he hasn't stopped loving her since! The spring of 1989 saw Danny deliver a valedictory address entitled "Ode to PHS," a poem that must rank as one of the strangest ever written.

Attracted by the high standards and the offer of a "free" ride, Danny applied to the service academies and was accepted to attend the U.S. Naval Academy. This subversive attempt to derail a promising astronomy career was luckily soon thwarted when Danny departed Annapolis during the first academic term, possibly the most difficult and wise decision for him to date. The next four years were spent up on the hill at the University of Minnesota at Duluth, feverishly developing a strong background for a future astrophysics career. Throw in three years of condensed matter research in Professor Sydor's experimental laboratory and a choir trip to Scandinavia and Eastern Europe, hindsight shows the time at UMD was well spent. Danny graduated *summa cum laude* with high honors in May 1993, a degree in physics and mathematics the final reward.

In August of 1993, the opportunity to seriously study astrophysics finally arose when Danny arrived in Ithaca as a fresh-faced Cornell physics graduate student. Beginning only with a vague idea of what astronomers do, five years later he finds his interest for the science has blossomed into a passion. Meanwhile, a newly found joy for teaching brought a Clark Award, Cornell's highest teaching honor, and a stint as lecturer at a local community college. He hopes to continue pedagogy pursuits in life after Cornell; Danny and Kim departed in July 1998 to start a postdoc at IPAC, the Infrared Processing and Analysis Center on the CalTech campus. Danny will be working on an ISO key project dealing with the interstellar medium of normal galaxies.

To my family

I find the great thing in this world

is not so much where we stand,

as in what direction we are moving

Oliver Wendell Holmes, Sr.

Acknowledgements

It is truly an honor to acknowledge the guidance of my mentor, Riccardo Giovanelli. Seldom have I encountered a comparable source of talent, curiosity, and unbridled enthusiasm. Since my professional knowledge of astronomy was essentially constructed from scratch while in graduate school, I attribute all (the positive aspects) of my expertise to Riccardo. I am fortunate to have worked with such an inspiring role model.

A wise person once opined: "Let it be said that ne'er again shall Giovanelli and Haynes be referenced separately." I concur. Any student who begins their astronomy career under Riccardo or Martha quickly realizes the other is a de facto advisor. Because of her considerable knowledge of all things astronomical and her forthright co-leadership of the ExtraGalactic Group, Martha has been key to the success of this thesis. Her continual and cheerful help is topped only by her energy.

Eduardo Hardy and Luis Campusano played a major role throughout this enterprise and were a joy to collaborate with. They were crucial in obtaining data from the southern skies and provided helpful suggestions that led to important improvements of this work. Saul Teukolsky and Joe Rogers also deserve my appreciation for sitting on my committee and reading through thesis drafts.

I am grateful to have worked with the kind observatory staffs at Mt. Palomar and CTIO. Rick Burress and Juan Carrasco at Palomar and Patricio Ugarte and Mauricio Fernandez of CTIO kept me awake on many nights with interesting stories and music. Stefano Borgani unselfishly provided the N-body simulations we used to quantify the effect of the Milky Way's disk on our calculations. Jill Morrison and Deb Hatfield have been generous with their gracious assistance throughout my stay in Ithaca. Thanks also goes to both the physics and astronomy departments for facilitating a physics Ph.D. based on astronomical research.

My time in Ithaca has been wonderful, mainly because of my friends. I'm still amazed that Lincoln, Tong, Phil, Ole, Aaron, and Robert all made it out to Minnesota for the wedding. Add Dustin, Matt, Jamie, Oskar, Stephen, and Giovanni to the list and it becomes obvious why volleyball, golf, softball, soccer, flag football and cross-country running filled much of my time away from school. The time I did spend at work didn't seem so much like work because of Marco, Katie, Liese, Sue, Julie, Jeremy, Dave, and Katrin. These people have made the last five years the most stimulating in my life. I hope they all get a chance to visit Pasadena!

I dedicate this work to my family. At the top of the list are my parents, Glenn and Merrily, and my wife, Kim. Without them I would not be who I am today. My mother and father have been unconditional supporters since day one. For the incessant drives to far-flung hockey arenas to the simple reunions we enjoy, to them I am deeply indebted. Luckily, I consider my closest friend to be my wife. Kim allowed my personal and professional lives, unfortunately but inevitably heavily intertwined as a physics graduate student, to coexist successfully. I am

also proud to be the brother of Pam, Denise, and Melanie, three sisters who always have time for me and likewise have not wavered in their encouragement. Lastly, I am happy to say that the family support network does not stop there but extends to many dear relatives, foremost among them Aunt Sue and Grandpa and Grandma Rundquist. Much of my strength is rooted in my family. My sincere thanks goes to them.

The results presented here are based on observations carried out at the Palomar Observatory (PO), at the Kitt Peak National Observatory (KPNO), at the Cerro Tololo Inter–American Observatory (CTIO), the (late) 300' telescope of the National Radio Astronomy Observatory (NRAO), and the Arecibo Observatory, which is part of the National Astronomy and Ionosphere Center (NAIC). KPNO and CTI0 are operated by Associated Universities for Research in Astronomy and NAIC is operated by Cornell University, all under cooperative agreements with the National Science Foundation. The Hale telescope at the PO is operated by the California Institute of Technology under a cooperative agreement with Cornell University and the Jet Propulsion Laboratory. NRAO is operated by Associated Universities, Inc. under a management agreement with NSF. This research has also made use of the NASA/IPAC Extragalactic Database which is operated by the Jet Propulsion Laboratory, California Institute of Technology, under contract with the National Aeronautics and Space Administration. This work has been supported through NSF grants AST94–20505 and AST96-17069 to Riccardo Giovanelli, and AST95–28860 to Martha Haynes.

Table of Contents

List of Tables

List of Figures

Chapter 1

Introduction

1.1 Cosmological Motivations

Important paradigm shifts in cosmology over the centuries have shaped the way we view our place in the Universe. From Copernicus' claim in the 1500s of a heliocentric solar system, to the discovery earlier this century that we reside in the outskirts of one of a multitude of "island universes," we have resigned ourselves to an increasingly unremarkable role. Perhaps the latest in this series of moves away from an Aristotelian universe comes from the discovery of a dipole anisotropy signature in the cosmic microwave background (CMB), the cool (2.75 K) remnant radiation of the Big Bang. Widely interpreted as a Doppler shift, the dipole's amplitude of $\sim$3 mK reflects the Sun's motion with respect to the CMB and thus indirectly implies that our Local Group (LG) of galaxies is moving in the same reference frame at a rate of 620 km s^{-1}. If gravity governs the motions of systems on large scales, it is clear that other systems direct our motion, reaffirming our cosmological insignificance. The spatial extent to which coherent motions persist is the matter of inquiry here.

Smooth Hubble expansion is expressed by the relation

$$cz = H_\circ r \tag{1.1}$$

where the quantities z (assumed above to be <<1) and r respectively indicate a galaxy's redshift and distance. The Hubble constant $H_\circ = 100h$ km s^{-1} Mpc^{-1} is the current epoch's expansion parameter, and h is a convenient scale factor which we will frequently use hereafter (the value of h is widely debated, but most estimates place it between 0.4 and 0.8). In the absence of density inhomogeneities, a galaxy should exactly follow smooth Hubble flow according to Equation 1.1. This is rarely the case, though, as it is well-known that matter tends to cluster together; it is the clumpy distribution of matter that leads to peculiar motions, or deviations from Hubble flow. Qualitatively, a "convergence depth" is the distance out to which significant contributions to a galaxy's peculiar motion are made.

Mathematically, the convergence depth can be easily understood when linear perturbations are assumed in the gravitational instability picture. Consider for example a test particle at the center of the sketch in Figure 1.1. Included in the drawing are cross-sections of two concentric, spherical shells centered on the test particle and the outline of a possible matter distribution. In linear theory, the fraction of the peculiar velocity of the test particle, contributed by the mass distribution within a radius R, can be written as

$$\mathbf{V}(R) \simeq \frac{H_\circ \Omega_\circ^{0.6}}{4\pi} \int \delta(\mathbf{r}) \frac{\hat{\mathbf{r}}}{r^2} W(R) d^3\mathbf{r}, \tag{1.2}$$

where $\Omega_\circ$ is the cosmological matter density parameter, δ is the mass overdensity, and $W(R)$ is a window function of width R, for example a Gaussian or tophat, centered at r=0 (Peebles 1993). If the distribution of matter more closely approximates homogeneity on larger scales, then contributions to the peculiar velocity

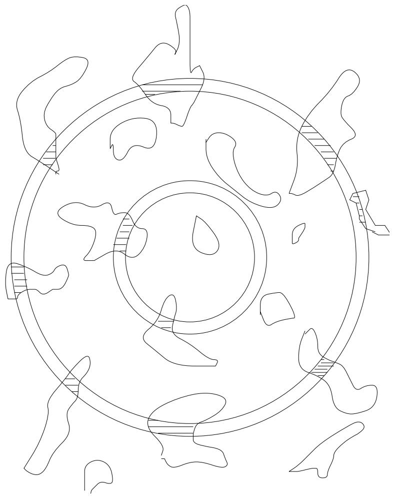

Figure 1.1 A pictorial guide to the notion of a convergence depth is sketched above. A possible matter distribution is outlined along with the cross-sectional views of two spherical shells. Compared to the mass within the inner shell, the mass in the outer shell is distributed more smoothly and thus contributes less to the motion of an object at the origin of the reference frame.

will decrease with distance from the test particle. In the example drawn above, the net gravitational force on the test particle due to the mass distributed in the outer shell is smaller than due to the mass in the inner shell. The convergence depth is the depth to which the matter distribution minimally affects the test particle's peculiar velocity. A quantitative, working definition of the convergence depth is the distance at which V approaches a large fraction (e.g. 90%) of its asymptotic value $V(R \rightarrow \infty)$. Gravity is a long-range force, however, so it is not to be expected that the convergence depth matches the effective length scale of density inhomogeneities.

1.2 The Local Convergence Depth as a Measurable Quantity

Observational estimations of the local convergence depth are facilitated through measurements of the reflex motion of the LG with respect to a series of spherical shells of increasing radii (note that it can similarly be determined in the CMB frame by estimating the distance to the nearest spherical shell whose bulk motion is indistinguishable from zero). The first such program was carried out by Rubin *et al.* (1976) on an all-sky sample of 96 Sc galaxies between redshifts of 3500 and 6500 km s^{-1}. They utilized the Hubble modulus $HM = \log cz - 0.2m$, where m is the apparent magnitude, to find the dipole motion; in essence, they computed a flux dipole. They reported the motion of the LG with respect to the shell of galaxies was 454$\pm$125 km s^{-1} towards $(l, b) = (163°, -11°)$. This differs substantially from the CMB dipole, suggesting a large bulk flow for the shell and a convergence depth significantly larger than $\sim 50h^{-1}$ Mpc. Subsequent work in this area has yielded conflicting results.

The situation can be grossly expressed into two main views. A picture of a *small* convergence depth ($cz < 5000$ km s^{-1}) is best represented by the Great Attractor (GA) model, in which the largest fraction of the velocity of the LG with respect to the CMB rest frame is explained by a mass concentration at $cz{\sim}4300$ km s^{-1} from us. A sphere of that radius, centered on the GA, would subtend a volume with global overdensity $\delta{\sim}1.3$ in a $\Omega_\circ{\sim}0.15$ universe (or $\delta{\sim}0.4$ for $\Omega_\circ{=}1$). This picture of a small convergence depth was first delineated using a sample of bright elliptical galaxies by Dressler *et al.* (1987) and Lynden–Bell *et al.* (1988), and it is also supported by the characteristics of the distribution of IRAS and optical galaxies (Lahav, Lynden-Bell, & Rowan-Robinson 1988; Lynden-Bell, Lahav, & Burstein 1989; Strauss *et al.* 1992; Hudson 1993). It should be mentioned, however, that some IRAS dipoles suggest significant contributions to the Local Group motion arise from the distribution of objects between 5000 and 10,000 km s^{-1} (e.g. Rowan-Robinson *et al.* 1990). The latter studies profit from flux dipoles or a peculiar velocity field that is iteratively solved for, initially supposing recessional velocities are indicative of distance. Assuming that the density of matter is linearly related to the density of galaxies, i.e. $\delta_{\rm gal}(r) = b\delta(r)$, the iterative process runs as follows: an initial density distribution is calculated, a generalized form of Equation 1.2 is applied to the distribution to generate a peculiar velocity field, the galaxy distances are then updated which leads to a new density distribution, and so on until tolerably small changes occur between iterations. The cumulative LG peculiar velocity (Equation 1.2) can then be plotted versus distance. After an appropriate scaling of the ratio $\Omega_\circ/b$ to match the asymptotic amplitude of the LG motion to the one we observe, the above listed observational programs that utilize this technique find 80% or more of the LG motion derives from matter within $\sim$50h^{-1} Mpc.

Proposals for a *large* convergence depth ($cz > 10,000$ km s^{-1}; Scaramella, Vettolani, & Zamorani 1994; Tini-Brunozzi *et al.* 1995; Branchini & Plionis 1996; Plionis & Kolokotronis 1998), mainly resulting from a similar analysis of the distribution of clusters of galaxies, suggest that much of our motion may be produced by mass concentrations as far as $\sim$13,000 km s^{-1} (e.g. the "Shapley Supercluster"). The latter view is corroborated by reports of bulk motion in the local universe (within 6000 km s^{-1}) via Tully–Fisher (TF) measurements by Willick (1990), Courteau *et al.* (1993) and Mathewson, Ford, & Buckhorn (1992), and by the recent analysis of the dipole of cluster brightest ellipticals by Lauer and Postman (1994, henceforth LP). The LP claim, based on the peculiar motions of all Abell clusters to 15,000 km s^{-1}, suggests the local volume of space within $\sim 100h^{-1}$ Mpc is traveling towards $(l, b) = (343°, +52°)$ at 689 km s^{-1}. The disagreement between these competing views of the convergence depth scale is wide, with important implications for cosmological models, which are generally unable to accommodate bulk flows with scales as implied by the large convergence depth camp.

1.3 The Tully-Fisher Relation

The most widely applied methods for the determination of redshift-independent distances of galaxies rely on the combination of photometric (distance dependent) and kinematic (distance independent) parameters. Among them, and arguably the most accurate, are the TF and D_n–σ (or fundamental plane, FP) relations, used for spiral and elliptical galaxies, respectively (studies utilizing SN Ia light curves yield more accurate distances to individual galaxies, but the volume sampling is rather sparse in comparison). With both these methods distances for individual galaxies, and therefore peculiar velocities, are computed by comparison with a fiducial *template* relation which must be observationally derived. In other words, the template relation defines the rest reference frame, against which peculiar velocities are to be measured. The importance of accurately calibrating such a tool cannot be overemphasized. It is in fact quite likely that the discrepancies between different claims of bulk motions may be related to insufficiently well determined template relations. Also, the vast majority of TF and FP samples do not probe redshifts larger than about 8000–10,000 km s^{-1}, and hence are not well suited to test the reality of large values of the convergence depth which, as argued by Scaramella, Vettolani, & Zamorani (1994), may not be reached until probing to 18,000 km s^{-1}.

TF is a powerful technique because it is one of the few distance indicators that can accurately probe velocity fields beyond $\sim 100h^{-1}$ Mpc. It is, however, a secondary distance indicator – the determination of absolute physical distances ultimately relies on the calibration of the relation using distances to nearby galaxies obtained from a primary distance indicator (e.g. HST Cepheid studies). The limited number of useful nearby calibrators (i.e. gas rich, inclined spiral galaxies) in turn limits the accuracy of such absolute distances. In a sense we can circumvent this problem by concerning ourselves with relative distances only and expressing distances in units of kilometers per second. Throughout this work we thus will use the concepts of distance and recessional velocity interchangeably.

1.3.1 The Physical Basis of the Tully-Fisher Relation

The TF relation is purely empirical, but it is instructive to consider its physical underpinnings. Consider a circularly rotating, pure exponential disk with scalelength $r_{\rm d}$ and central intensity $I(0)$. The luminosity of such a system is

$$L_{\rm d} = \int_0^\infty I(0) e^{-r/r_{\rm d}} dr \int_0^{2\pi} r d\theta = 2\pi I(0) r_{\rm d}^2 \tag{1.3}$$

A length scale dependence also arises in the relation for the mass contained within a radial distance r: $M(r) = V_{\rm rot}(r)^2 r/G$. Spiral galaxy rotation curves typically level off in the outer disk regions, allowing us to easily relate the total mass to the constant disk rotational speed: $M \propto V_{\rm d}^2 r_{\rm d}$. If $\Gamma = M_{\rm d}/M$ is the disk's fraction of the total mass, and if we let $M_{\rm d}/L_{\rm d}$ be the disk mass to light ratio, then

$$L_{\rm d}\left(\frac{M_{\rm d}}{L_{\rm d}}\right)\Gamma^{-1} \propto V_{\rm d}^2 r_{\rm d} \tag{1.4}$$

Combining the above results yields

$$L_{\rm d} \propto \frac{\Gamma^2}{(M_{\rm d}/L_{\rm d})^2 I(0)} V_{\rm d}^4 \tag{1.5}$$

Equation 1.5 reduces to $L_{\rm d} \propto V_{\rm d}^4$ when a number of assumptions are made, namely that Γ, $M_{\rm d}/L_{\rm d}$, and $I(0)$ are all constant. The first two assumptions seem unlikely in the face of observational and theoretical constraints (Whitmore, Forbes, & Rubin 1988; Arbolino & Ruffini 1988; Persic, Salucci, & Stel 1996; Navarro, Frenk, & White 1996). The last assumption of a constant central brightness received early support 30 years ago in the form of Freeman's Law (Freeman 1970), but it has since been acknowledged to be a sample selection effect (e.g. Disney 1976; Gilmore, Hodge, van der Kruit 1990; Giovanelli *et al.* 1994; McGaugh, Schombert, & Bothun 1995). The three parameters combined, however, apparently conspire to yield a rather tight TF relation, but with the exponent for $V_{\rm d}$ generally found to be slightly less than 4.

A familiar form of the TF relation is found by taking the logarithm of Equation 1.5,

$$M_\lambda = a \log_{10} W + b \tag{1.6}$$

where M_λ is the absolute magnitude in the λ passband and W the full rotational velocity width of the disk. There are no firm reasons for Equation 1.6 to be exactly linear. In fact, some evidence exists for a knee in the TF relation for low velocity widths (Aaronson *et al.* 1986; Hoffman & Salpeter 1996; G97b). We shall see later, though, that this end of the TF relation has a large scatter and is thus more difficult to confidently interpret.

1.3.2 Tully-Fisher Ingredients

The primary TF ingredients for determining the distance to a galaxy are the galaxy's flux (apparent magnitude), recessional velocity (redshift), and disk rotational velocity, the last requiring an estimate of the disk inclination to the line-of-sight. Measuring the apparent magnitude of a galaxy at moderate redshift is feasible with a small telescope (1 m class). The earliest TF studies were done at optical wavelengths but it was soon realized that both Galactic and internal extinction corrections to the fluxes are minimized at longer wavelengths. Apart from some previous near-IR, H band programs (e.g. Aaronson *et al.* 1986), the TF relation has enjoyed most of its success at wavelengths at the optical/near-IR boundary, i.e. the R and I bands. This wavelength regime offers several benefits. The stars that supply this light are distributed smoothly throughout the disk (compared to the patchy appearance of bluer stars preferentially located in star forming regions), thus allowing for accurate disk inclination determinations. In addition, CCD detectors are highly efficient at R and I, and the data is fast to acquire and process, versus relatively laborious near-IR work.

Velocity width observations require long integration times, large telescopes, or both (accurate redshifts being acquired simultaneously with velocity widths). Any kinematical tracer of the rotating disk is useful, but by far the most reliable and popular methods rely on the 21 cm line from neutral hydrogen (HI) regions or optical emission lines from ionized hydrogen (HII) regions, most notably the Hα 6563Å line. Velocity widths from HI profiles are desirable because cold hydrogen gas is typically distributed throughout the optically-observable disk and well beyond, thus promoting fair sampling of the maximum rotational speed in the disk without worry for the disk's position angle. On the other hand, as TF studies progress to higher redshifts or focus on denser environments (clusters), source confusion favors the use of optical rotation curves. The radio telescopes with the highest spatial resolution, arrays, unfortunately lack the necessary sensitivity and bandwidth coverage. Large single dishes such as those at Arecibo and Nançay would be useful, but they simply do not map the entire sky.

There are constraints on TF candidates. Foremost among them are the requirements of a gas rich, rapidly spinning disk inclined to the line of sight by $40°$ or more. Face-on disks are useless rotational velocity indicators, and slowly spinning disks ($V_{\rm rot} \lesssim 80$ km s^{-1}) exhibit such large scatter in a TF diagram that they are unreliable for peculiar velocity work. Another important limitation to TF work is the correction for internal extinction, the absorption of light within the disks of external galaxies. Such a correction is highly sensitive to disk inclination measures, and the recipes found in the literature unfortunately vary significantly, leading to possible spurious signatures in peculiar velocity fields. There are other concerns to consider in the construction of the TF template, and we discuss several of them next.

1.3.3 The Calibration of the Tully-Fisher Relation

Accurate peculiar velocities require an accurate reference template. We reiterate that this template should represent the kinematic rest frame but it need not indicate absolute distances. For the linear TF relation this involves tailoring the sample selection to facilitate reliable measures of the slope and magnitude offset, or "zero point." The slope of the TF relation is best determined by a sample that maximizes the dynamic range in $(M, \log W)$, i.e. one that preferentially includes nearby objects. On the other hand, the magnitude offset of the relation is best obtained from a sample of distant objects for which a peculiar motion of given amplitude translates into a small magnitude shift. It has been common practice to calibrate the TF relation using one relatively distant cluster of galaxies, for example the rich Coma cluster at $cz{\sim}7200$ km s^{-1}. The justification for such a choice relies on the assumption that galaxies within a cluster are essentially at the same redshift – any differences in their radial velocities are attributed to the cluster's virial stretch. Thus, they all equally participate in the local peculiar velocity field and they should all obey the same local TF relation; multiple measures improve distance estimates. Another reason to choose a cluster like Coma for calibration is, as mentioned above, the selection of a distant object limits the impact of the object's peculiar velocity V, at least to the extent the physical size of the cluster is small in comparison to its mean distance; peculiar velocities introduce relative distortions of redshifts that are larger for nearby objects than for distant ones. In terms of magnitude, if $V{<<}cz$, the zero point will only be off by $\Delta b \simeq -2.17V/cz$ (cf. Equation 7.1).

There are several problems with the above calibration scheme. First, a "template" cluster needs to have a large sample of spiral galaxies. Second, the chosen cluster must fairly represent the global TF relation. The galaxy density profile, the morphological distribution, and the strength of the intracluster medium vary from cluster to cluster. Each of these factors may alter the coefficients of the TF relation. Finally, even for a cluster as distant as Coma, typical cosmic velocities may bias the relation's offset. If the cluster were moving at a plausible speed of 500 km s^{-1}, then all other estimates of peculiar velocities that use the template will systematically be off by $500(cz/cz_{\rm template})$, regardless of statistical uncertainties. The error increases with redshift.

To avoid such systematics in the TF relation, Giovanelli *et al.* (1997a,b, hereafter G97a, G97b) use a "basket of clusters" approach. Their template is derived from an average of the TF relations extracted from 555 galaxies in 24 separate clusters distributed throughout the sky between 1000 and 9000 km s^{-1}. The sample is referred to as the "SCI" sample. This method is obviously more likely to recover the true rest frame than the use of a single cluster would, even if this volume of space exhibits bulk motion. The proximity of the SCI sample provides the stretch in galactic properties necessary to determine accurately the TF slope. Also, the large database afforded by the SCI allows the statistical uncertainty of the magnitude offset to be determined to $0.02-0.03$ magnitudes. The systematic uncertainty in the offset is larger. For a sample of N objects with an rms velocity of $\langle V^2\rangle^{1/2}$ at a mean redshift of $\langle cz\rangle$, the expected accuracy of the zero point is limited by systematic concerns to

$$\sigma_b \approx \frac{2.17\,\langle V^2\rangle^{1/2}}{\langle cz\rangle\,\sqrt{N}}. \tag{1.7}$$

G97b conclude the SCI systematics only allows the univeral TF zero point to be determined to within 0.04 magnitudes. Thus the overall zero point accuracy obtainable from the SCI sample is ~0.05 magnitudes. To improve upon this figure, and to sensitively test claims of a large convergence depth, we look to a more distant set of clusters.

1.4 The Project

The claims of large amplitude, coherent flows on scales up to $100h^{-1}$ Mpc mentioned in Section 1.2 are difficult to accomodate with current cosmological scenarios (Gramann *et al.* 1995). Observationally, the LP claim has been challenged as well. Riess, Press, & Kirshner (1995) used 13 SN Ia observations and found evidence for a small local bulk flow. Giovanelli *et al.* (1996) similarly excluded the LP solution, on the basis of TF measurements of field galaxies. In a recent contribution based on TF distances of about 2000 galaxies within 9500 km s^{-1}, Giovanelli *et al.* (1998a; G98a) similarly report evidence against the existence of large scale flows as described above, and support for a relatively small convergence depth. Yet a clear-cut solution of the disagreement is still wanting, because the sample of supernova type Ia of Riess *et al.* (1995) is too sparse (Watkins & Feldman 1995) and the Tully-Fisher (TF) sample of G98a is of limited depth. The G98a sample of peculiar velocities obtained using the TF method is referred to a template relation based on the SCI (G97b). If the peculiar velocity field is characterized by strong spatial gradients, a shallow sample would not provide a quantitatively effective test of large-scale flows; not until the volume from which the template is extracted is as large as that over which bulk flows are claimed, will such conclusions be legitimately be corroborated. This is particularly important in view of the claims (Scaramella, Vettolani, & Zamorani 1994, Tini Brunozzi *et al.* 1995, and Branchini & Plionis 1996) that asymptotic convergence of the Local Group reflex motion may only be reached at distances in excess of 10,000 km s^{-1}. It is therefore possible that our global understanding of large scale motions is strongly biased by the (poor) reliability of the currently available reference frames. This work aims at the direct determination of the TF relation for an all-sky cluster set extending to distances exceeding the highest reported values of the convergence depth.

A second issue of concern regards the amplitude of systematic errors in the TF template relation used to measure peculiar velocities, as outlined in Section 1.3.3. Though the SCI is an ideal sample to measure the TF slope, it conversely works against pinning down the relation's zero point offset. Thus, the benefits of measuring peculiar velocities at higher redshifts are twofold: the contribution to the Local Group velocity field arising at large scales is better understood *and* the (offset) accuracy of all peculiar velocity measurements improves. To accomplish this goal, we undertook a vigorous observational program to probe the large scale peculiar velocity field to $\sim 200h^{-1}$ Mpc. In the process we have obtained velocity profiles and I band photometry for an all-sky sample of 522 galaxies from the fields of 52 clusters between $\sim$50 and $200h^{-1}$ Mpc. We coin this sample SCII.

The overall scatter of the I band TF relation, approximately $0.3 - 0.4$ magnitudes, determines how accurate peculiar velocities can be measured. TF is accurate to about 15%. This means that for an individual galaxy at, say 15,000 km s^{-1}, the method is able to predict the distance to within 2250 km s^{-1}. This value is considerably larger than the typical value of peculiar velocities, which are of order 500 km s^{-1} or less. Even if 50 objects per cluster were to be measured, however, the distance of the cluster at 15,000 km s^{-1} would not be characterized to better than $2250/\sqrt{50} \sim 300$ km s^{-1}, and we measured on average 8-9 of them. The purpose of this study is thus *not* the determination of *individual* distances of remote clusters. The combination of measurements in many clusters does, however, allow a global solution for a dipole of the velocity field, verifying whether the sample as a whole moves with respect to the CMB (or the LG) to within 150–200 km/s.

The remainder of this thesis is devoted to a complete description of our work on this project over the past three years, from the first observing run to the recent determination of the local convergence depth. Details of the sample and its selection are covered in Chapter 2. In Chapters 3 and 4 we review our observational approach to the photometry and spectroscopy for this project, as well as outline how physical parameters are estimated from the data. Chapter 5 presents the data and Chapter 6 covers the construction of the TF template relation. A variety of results from the peculiar velocity sample are given in Chapter 7, and we review them in Chapter 8.

Chapter 2

Sample Selection

2.1 Introduction

An important step at the beginning of any observational study is the definition and selection of the sample and the methodology for executing the observational program. Careful considerations at an early juncture of what to observe encourage a more focussed project and help to eliminate, or at least diminish, selection biases that will later need to be accounted for. This chapter details our approach to defining the SCII sample. Section 2.2 gives a historical background for clusters of galaxies, including the catalog from which our sample originates. Section 2.3 covers cluster and galaxy selection and Section 2.4 reviews some of the properties of the clusters chosen for this work.

2.2 Clusters of Galaxies

2.2.1 The Abell Catalog

The Abell catalog of galaxy clusters was developed in the 1950's by George Abell at the University of California, Los Angeles (Abell 1958). This catalog, coupled with its southern extension (Abell, Corwin, and Olowin 1989; hereafter ACO), continues to serve as the industry standard as a source for large-scale structure studies. To generate the northern catalog Abell used the Palomar Observatory Sky Survey plates to search for aggregates of galaxies; ACO employed plates obtained with the Schmidt telescope at Siding Spring. The goal of the catalogs was to provide a complete listing of all rich clusters visible on the survey plates. A set of galaxies qualified for entry into the Abell/ACO catalog if the following criterion was met: at least 30 galaxies with apparent magnitudes between m_3 and m_3+2 were found within a canonical physical distance from the apparent cluster center, where m_3 is the apparent magnitude of the third brightest galaxy in the cluster.[1] It was later found that this standard "counting radius" is $1.48h^{-1}$ Mpc, a radius we will hereafter refer to as the Abell radius. A typical cluster contains 80% of its mass within one Abell radius (Oemler 1974). Figure 2.1 displays the 4073 clusters of the Abell/ACO catalog. Three characteristics of the catalog are immediately apparent. The first is the lack of objects about zero degrees Galactic latitude. This region is the so-called "Zone of Avoidance" (ZoA) and is merely the effect of large line-of-sight extinction in the plane of the Milky Way. The Abell/ACO catalog thus misses clusters in one third of the sky. We will return to

[1] A numerical classification scheme was devised to rank clusters by their number counts. The Abell richness classes are R=0, 1, 2, 3, 4, 5 for $N(m_3+2>m>m_3) \geq$ 30, 50, 80, 130, 200, 300.

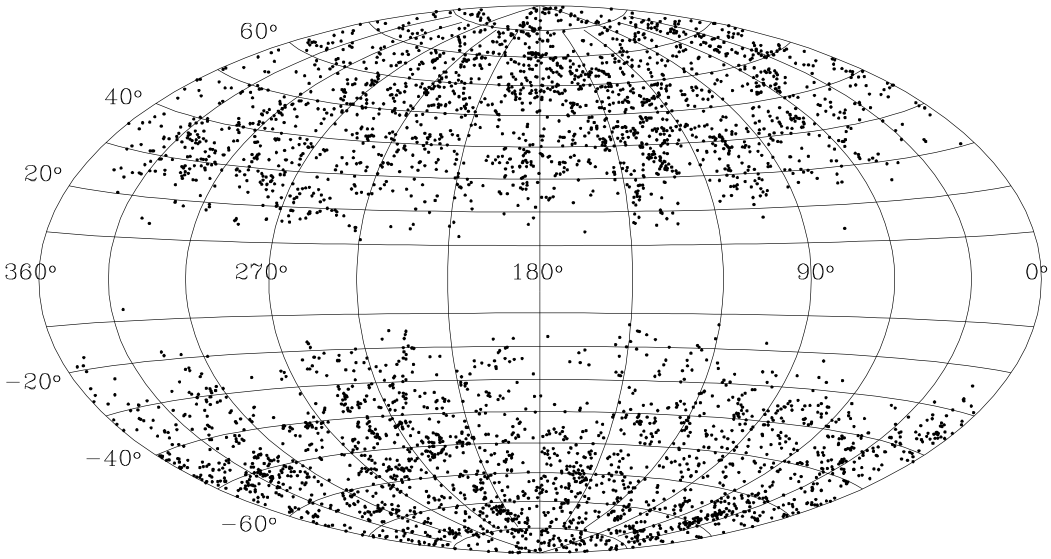

Figure 2.1 The all-sky distribution, in galactic coordinates, of the 4073 clusters of galaxies that make up the Abell/ACO catalog. The central gap in the distribution arises from line-of-sight extinction in the Milky Way.

a discussion of this omission in Chapter 7 when we consider its effect on peculiar velocity dipole calculations. Another striking characteristic of the catalog is the complete sky coverage of the cluster distribution outside of the ZoA. The third immediately apparent quality is the structure seen amongst the clusters. Even viewed in projection, clustering in their distribution is obvious. These last two aspects of the distribution are the reasons that so many cosmology endeavors consider the Abell catalog to be their primary resource. The Abell catalog is from which our sample stems.

2.2.2 Clusters of Galaxies as Cosmological Tools

The reputation of clusters of galaxies as useful systems for cosmology has been on the rise for several years. The recent literature has shown that clusters can be used to advantage for a variety of large scale problems. N-Body computations tell us that cluster peculiar velocities are known to efficiently recover the large scale velocity and potential fields (Gramann *et al.* 1995). Further simulations by N. Bahcall and collaborators indicate the cluster peculiar velocity distribution reliably matches that of the underlying smoothed matter's velocity distribution. This holds as well for large scale bulk motions: for a given bulk motion of the underlying matter, cluster peculiar velocities reproduce consistent measures of the flow (Bahcall *et al.* 1994a,b; Gramann *et al.* 1995). Furthermore, though clusters of galaxies only sparsely sample the large scale velocity field, they do so much more accurately than individual galaxies can. This advantage arises because measurements of many galaxies *within a single bound system* can be made. Precise comparisons of observed large scale peculiar velocities can then be made with those predicted by cosmological theories (Watkins & Feldman 1995; Cen *et al.* 1994; Feldman & Watkins 1994; Strauss *et al.* 1995; Croft & Efstathiou 1994; Borgani *et al.* 1997), assuming that peculiar velocities originate from the gravitational growth of cosmic structures.

Peculiar motions are not the only properties of clusters that help to constrain cosmological models: the *distribution* of clusters is also crucial to understanding the origin of large scale structure. Assuming again the gravitational instability picture holds, the typical separation between clusters in the present epoch is much greater than expected deviations from their primordial locations. In other words, the current distribution of clusters should provide us with information on the Universe's original power spectrum (Borgani *et al.* 1995; Branchini & Plionis 1996; Tini Brunozzi *et al.* 1995; Plionis & Valdarnini 1991; Moscardini *et al.* 1996). Moreover, since the distribution of clusters represents the peaks in the matter distribution, we preferentially use clusters to explore large scale structure at high redshifts. One example of the importance of this fact is the ability to map velocity fields on extremely large scales using the Sunyaev-Zel'dovich effect, whereby the Doppler-shifted CMB radiation passing through the hot intracluster medium is an indication of motion with respect to the CMB. In general, as observational cosmology continues to search higher and higher look-back times, astronomers are increasingly relying on clusters of galaxies to serve as physical probes.

2.3 Sample Definition

Clusters of galaxies are practical TF targets. The core ingredient for TF work is a sample of gas rich and thus typically late-type spiral galaxies. Considerations of observational overhead alone favor studying galaxies in the context of rich clusters. While it is known that disk systems dominate the field population, a given cluster usually is home to a substantial number of spiral galaxies as well (see, for example, the reviews by Sarazin 1986 or Dressler 1984). The exact ratio of the spiral to elliptical galaxy population fractions varies from cluster to cluster and is a function of cluster richness, but the peripheries of a cluster frequently are populated with late-type galaxies. Thus, a small number of wide-field images from a modest-sized telescope can effectively "map" a cluster, and they will likely contain numerous promising TF candidates.

A second consideration that suggests the use of clusters in TF experiments is the determination of the TF template. As outlined in Chapter 1, the template is preferentially measured within a cluster, or determined as an average of templates from measurements in separate clusters. We reiterate here that the slope can only be accurately measured if a broad dynamic range of TF parameters can be observed, a fact which suggests the measurement of the slope is preferentially obtained from a relatively nearby sample. In contrast, the kinematical offset is better characterized at higher redshifts, where cosmic peculiar motions play a smaller role in shifting objects away from the template. Our motive of improving the TF offset accuracy plays an important role in characterizing the redshift distribution of our sample.

A third advantage to using clusters of galaxies in TF work is the $\sim\sqrt{N}$ increase in statistical accuracy per cluster they afford if N TF measurements per cluster are available. The typical scatter in the TF relation, excluding the effect of peculiar motions, is ~0.35 mags (G97b) and translates to an uncertainty of 15% in redshift-independent distance measurements. The estimate of a system's peculiar motion is of course more accurate when information from a large number of objects within the system is used. However, if an all-sky survey of peculiar motions is the goal, concentrating observations to a single cluster or to a small number of clusters parallels an increase in overall sample sparseness. The choice between a densely sampled volume of low accuracy peculiar velocities, and a sparse sample of accurate peculiar velocities ultimately depends on the particular goals of the study. We investigated what sample characteristics would facilitate the most accurate determination of the TF offset and the local bulk flow, as discussed next.

2.3.1 Monte Carlo Simulations of Sample Selection

To ascertain the optimal distribution of clusters and number of galaxies per cluster to observe, in order to achieve the desired goals, we relied on numerical simulations. The only limitation enforced was the total number of objects that could be observed, for a reasonable thesis timescale. A wide range in the number of clusters and the number of objects per cluster was explored. A variety of models of the peculiar velocity field (multi-attractor, linear bulk flows, quiescent, etc.) was imposed, and different models for the shape of the ZoA were considered. TF errors were assigned using random Gaussian deviates of the scatter distribution in G97b. The results, which took into consideration that clusters of galaxies have positions that are correlated in space (and therefore a random choice of N clusters does not guarantee that N independent points are sampled!), suggested that about 50 clusters of galaxies needed to be observed, with measurements of at least 7-8 TF galaxy distances in each.

2.3.2 Cluster Selection

The initial characterization of the SCII cluster sample predates this study and originates from preparatory work done by R. Giovanelli for the SCI nearby cluster TF study. Clusters were selected using the Abell/ACO rich cluster catalog as a guide. Expediency played a major role in choosing the parent sample of clusters, of which this thesis sample is a subset. Nearby clusters ($cz \lesssim$ 10,000 km s^{-1}) with preexisting HI velocity widths and I band fluxes were favored, and the more distant clusters ($cz \gtrsim$ 10,000 km s^{-1}) that already had a large number of redshifts available were likewise strongly considered. Table 2.1 lists the main parameters of the 52 chosen clusters for this work. The table has the following organization:

Column 1: Standard name according to Abell/ACO catalog.

Columns 2 and 3: Adopted coordinates of the cluster center, for the epoch 1950; they are obtained from ACO, except for the entries A1983b and A2295b, systems found to be slightly offset from A1983 and A2295 in both sky position and redshift.

Columns 4 and 5: systemic velocities in the heliocentric and in the cosmic microwave background reference frame (Kogut *et al.* 1993), respectively. For all the clusters we derived a new systemic velocity, combining the redshift measurements available in the NED[2] database with our own measurements. An estimated error for the systemic velocity is parenthesized after the heliocentric figure.

Column 6: the number of cluster member redshifts used in determining systemic velocities.

Column 7: Abell richness class.

Column 8: Bautz-Morgan code (Bautz & Morgan 1970) listed in ACO.[3]

Figure 2.2 displays the sample in Galactic coordinates. The symbol sizes are inversely proportional to the cluster redshifts; two examples are given in the lower left for scale. The distribution is similar in many respects to that given in Figure 2.1 of the entire Abell catalog, except for the clear discrepancy in sky sampling rate. An alternative display of the sample is shown in Figure 2.3, a stereographic view of the sample in Galactic Cartesian coordinates. The dashed circles have

[2]The NASA/IPAC Extragalactic Database is operated by the Jet Propulsion Laboratory, California Institute of Technology, under contract with the National Aeronautics and Space Administration.

[3]The Bautz-Morgan type is a morphological classification, running from cD-dominated clusters (I) to clusters with no overly-luminous members (III). A colon indicates an uncertain type.

Table 2.1 The SCII Cluster Sample

Cluster	R.A. B1950	Dec. B1950	(l, b) B1950	$cz_{\rm helio}$ km s^{-1}	$cz_{\rm cmb}$ km s^{-1}	N_z	R	B-M
A2806	003754	−562600	(306,−61)	8019(080)	7867	27	0	I-II
A114	005112	−215800	(128,−85)	17436(143)	17144	41	0	—
A119	005348	−013200	(126,−64)	13470(085)	13141	73	1	II-III
A2877	010736	−461000	(293,−71)	7165(058)	6974	130	0	I
A2877b	010736	−461000	(293,−71)	9231(048)	9040	37	-	—
A160	011012	+151500	(131,−47)	12390(141)	12072	32	0	III
A168	011236	−000100	(136,−62)	13365(058)	13049	67	2	II-III:
A194	012300	−014600	(142,−63)	5342(037)	5037	123	0	II
A260	014900	+325500	(137,−28)	10924(111)	10664	45	1	II
A397	025412	+154500	(162,−37)	9803(078)	9594	42	0	III
A3193	035654	−522900	(262,−47)	10559(112)	10522	32	0	I
A3266	043030	−613500	(272,−40)	17775(061)	17782	328	2	I-II
A496	043118	−132100	(210,−36)	9860(059)	9809	148	1	I:
A3381	060806	−333500	(240,−23)	11410(048)	11510	41	1	I
A3407	070342	−490000	(259,−18)	12714(136)	12861	14	1	I
A569	070524	+484200	(169,+23)	5927(043)	6011	55	0	II:
A634	081030	+581200	(159,+34)	7822(042)	7922	51	0	III
A671	082524	+303500	(193,+33)	15092(194)	15307	26	0	II-III:
A754	090624	−092600	(239,+25)	16282(082)	16599	90	2	I-II:
A779	091648	+335900	(191,+44)	6967(101)	7211	50	0	I-II:
A957	101124	−004000	(243,+43)	13464(120)	13819	43	1	I-II:
A1139	105530	+014600	(251,+53)	11851(071)	12216	26	0	III
A1177	110648	+215800	(221,+66)	9755(081)	10079	8	0	I
A1213	111348	+293200	(202,+69)	14006(090)	14304	36	1	III
A1228	111848	+343600	(187,+69)	10517(034)	10794	41	1	II-III
A1314	113206	+491900	(152,+64)	9764(154)	9970	28	0	III
A3528	125136	−284500	(304,+34)	16459(139)	16770	30	1	II
A1736	132406	−265100	(313,+35)	10397(050)	10690	62	0	III
A1736b	132406	−265100	(313,+35)	13724(084)	14017	116	-	—
A3558	132506	−311400	(312,+31)	14342(044)	14626	482	4	I
A3566	133606	−351800	(314,+26)	15370(087)	15636	32	2	II
A3581	140436	−264700	(323,+33)	6865(126)	7122	31	0	I
A1983b	144724	+170600	(019,+61)	11332(062)	11524	27	-	—
A1983	145024	+165700	(019,+60)	13527(045)	13715	88	1	III:
A2022	150212	+283700	(043,+61)	17262(072)	17412	24	1	III
A2040	151018	+073700	(009,+51)	13440(061)	13616	37	1	III
A2063	152036	+084900	(013,+50)	10445(053)	10605	125	1	II:
A2147	160000	+160200	(029,+44)	10493(085)	10588	93	1	III

Table 2.1 (Continued)

Cluster	R.A. B1950	Dec. B1950	(l, b) B1950	$cz_{\rm helio}$ km s^{-1}	$cz_{\rm cmb}$ km s^{-1}	N_z	R	B-M
A2151	160300	+175300	(032,+45)	11005(059)	11093	143	2	III
A2256	170636	+784700	(111,+32)	17442(132)	17401	94	2	II-III:
A2295b	175900	+691600	(100,+30)	18701(082)	18633	6	-	—
A2295	180018	+691300	(099,+30)	24622(199)	24554	9	0	II-III
A3656	195712	−384000	(002,−29)	5750(064)	5586	31	0	I-II
A3667	200830	−565800	(341,−33)	16582(094)	16477	128	2	I-II
A3716	204754	−525400	(346,−39)	13763(064)	13618	174	1	I-II:
A3744	210418	−254100	(021,−40)	11386(089)	11123	42	1	II-III
A2457	223312	+011300	(069,−47)	17643(110)	17280	20	1	I-II:
A2572	231554	+182800	(094,−39)	11857(100)	11495	38	0	III
A2589	232130	+163300	(095,−41)	12288(095)	11925	58	0	I
A2593	232200	+142200	(093,−43)	12414(086)	12049	67	0	II
A2657	234218	+085200	(097,−50)	12028(137)	11662	40	1	III
A4038	234506	−282500	(025,−76)	9012(063)	8713	180	2	III

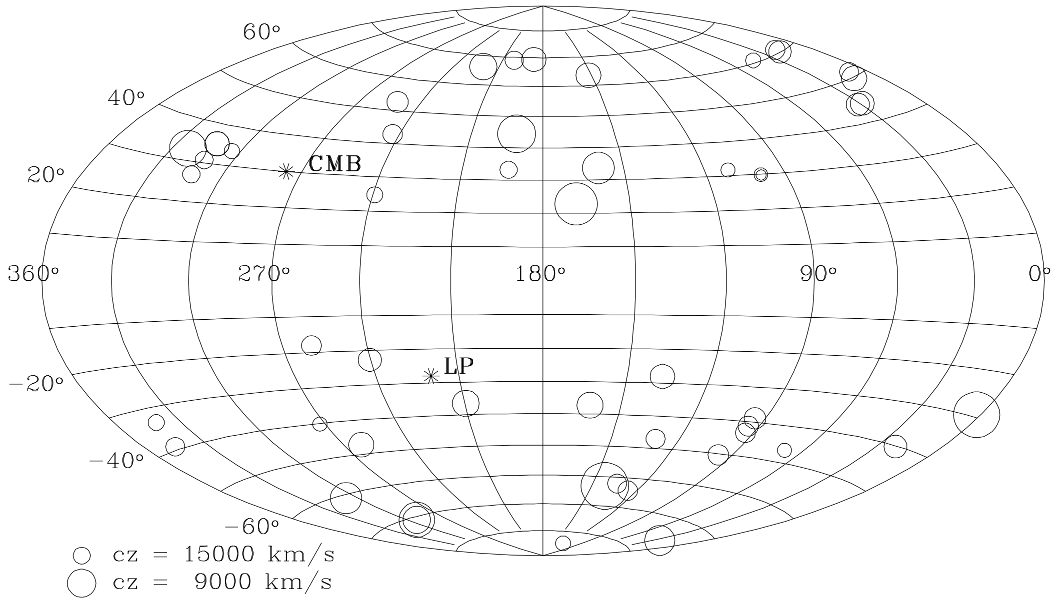

Figure 2.2 The all-sky distribution of the SCII sample in Galactic coordinates. The circles are drawn inversely proportional to the cluster redshifts. The two examples in the lower left give the scale. Asterisks mark the apices of the motion of the Local Group with respect to the CMB and the LP cluster inertial frame.

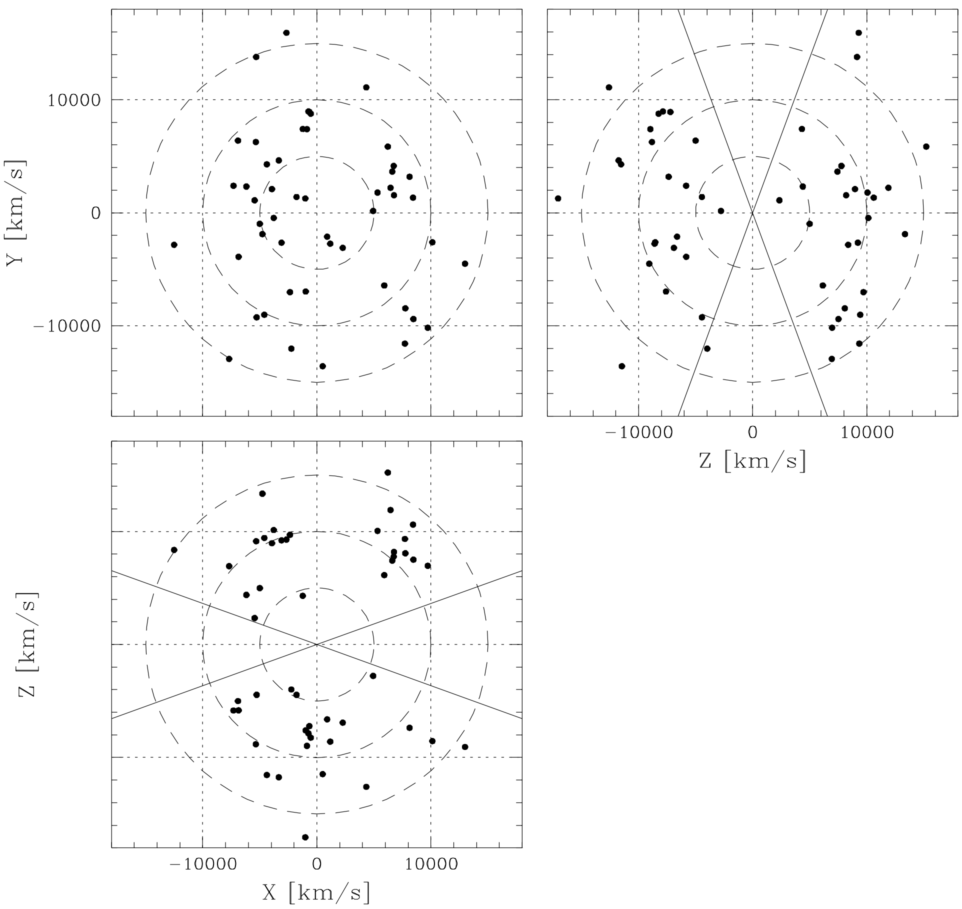

Figure 2.3 The stereographic representation in Galactic Cartesian coordinates of the 52 clusters of galaxies that make up the SCII sample. The dashed circles have radii of 5000, 10000, and 15000 km s^{-1}. The solid lines in the [X,Z] and [Z,Y] plots indicate $|b| = 20°$, the approximate extent of the Zone of Avoidance.

radii of 5, 10, and 15 thousand km s^{-1} and the solid lines in the [X,Z] and [Z,Y] plots are for $|b| = 20°$ and indicate the size of the ZoA. This distribution recalls our first criterion in selecting the sample.

(i) The data set should uniformly sample as much of the sky as prudently feasible. Since the main thrusts of this work are to recover a bulk flow measurement and to accurately determine a kinematical offset even in the presence of such a flow, an all-sky sample is required. Unfortunately, the paucity of clusters and the large and uncertain extinctions seen in the direction of the ZoA prohibit us from sampling that portion of the sky. In addition, the likelihood of foreground star contamination increases dramatically for objects at low galactic latitudes. Our formal criterion was to select clusters at $|b| \gtrsim 20°$ from the whole sky.

A second characteristic of the sample is its redshift distribution.

(ii) The range of redshifts runs from 5000 km s^{-1} to 25,000 km s^{-1}, with fully 90% of the clusters lying between 7000 km s^{-1} and 19,000 km s^{-1} (see Figure 2.4). As mentioned previously, our goal is a precise TF offset. Though the proximity of the G97a,b sample provides the stretch in galactic properties necessary to determine accurately the TF slope, it conversely works against pinning down the relation's zero point offset; peculiar velocities introduce relative distortions of redshifts that are larger for nearby galaxies than for distant ones. A second motivation for our particular redshift distribution arises from recent claims of the extent of the convergence depth. There have been suggestions (cf. Chapter 1) that significant contributions to our Local Group's motion through the CMB may originate from as far away as 18,000 km s^{-1}. This fact was kept in mind during cluster selection. Lastly, we remark that an impetus for this study was the result of LP, that the local volume of radius 8000 - 11,000 km s^{-1} is participating in a bulk motion of amplitude 700 km s^{-1}. Claims of large bulk flows and large convergence depths cannot be adequately tested until the volumes over which the claims are made are sampled. It is evident from Figure 2.4 that our sample's distance range provides an opportunity to effectively test the above claims.

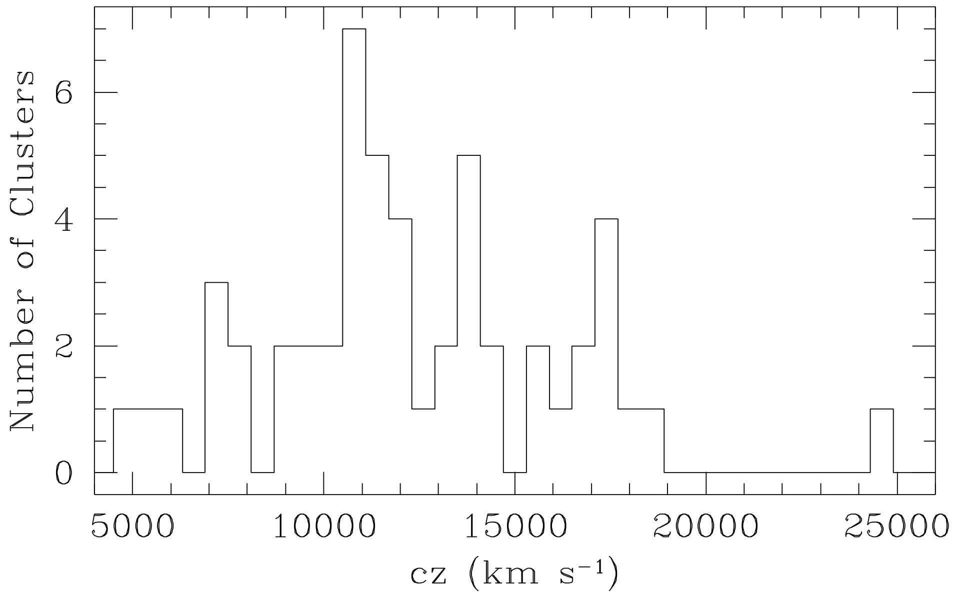

Figure 2.4 The redshift distribution of the clusters.

2.3.3 Galaxy Selection

To determine locations of target fields to be imaged, we visually scanned the Palomar Observatory Sky Survey plates for regions in the clusters containing promising disk systems appropriate for TF work. The selection of target galaxies for this study stemmed directly from the images obtained. A discussion of the imaging for this project is contained in Chapter 3. Each image in clusters chosen for spectroscopy was searched for spiral disks with the following properties:

(i) disk inclinations $\gtrsim 40°$;

(ii) lack of dominating bulges – bulgy disk systems tend to be gas deficient and thus undesirable for Hα spectroscopy. Moreover, it is preferable to select a more homogeneous sample to limit morphological bias effects, as we will see in Chapter 6;

(iii) no apparent warps/interacting neighbors; and

(iv) no nearby bright stars which may affect flux measurements.

It should be noted that the above properties served as guidelines for selecting TF candidates, but occasionally the guidelines were not strictly followed, as occasionally our hand was forced by the vagaries of telescope allocation committees e.g. a small number of our galaxies are bulgy disk systems, most likely of morphological type Sab or earlier. Coordinates and position angles for approximately 2250 TF candidates were obtained from the Digitized Sky Survey[4] and are accurate to better than $2''$.

2.4 Cluster Characteristics

As in all observational efforts, there are some variations in the characteristics of the data. Some average properties differ from cluster to cluster, and traits within a single cluster deviate from galaxy to galaxy. One manifestation of a cluster-to-cluster dissimilarity is the number of TF measurements for a cluster. Within a given cluster, departures from uniformity may exist, for example, in the physical extent of the rotation curves. While selection bias is an unavoidable problem, the success of a campaign relies in the clear understanding of the bias characteristics. To begin to understand if these variations depend on environment, it is useful to have a background knowledge of the general characteristics of each cluster. What follows is a brief summary of individual cluster properties, as determined from the literature and our own work. The clusters are described in order of increasing Right Ascension.

[4]The Digitized Sky Surveys were produced at the Space Telescope Institute under U.S. Government grant NAG W-2166. The images of these surveys are based on photographic data obtained using the Oschin Schmidt Telescope on Palomar Mountain and the UK Schmidt Telescope.

Abell 2806

Abell 2806 is a richness class 0 cluster with most of the spiral galaxies located in the cluster's peripheral regions. There are few redshifts presently available in the literature.

Abell 114

This cluster is spiral rich. It is situated between A133 and A2824, the two other clusters that comprise the central portion of a supercluster (Postman, Huchra, & Geller 1992).

Abell 119

This cluster is dominated by a D cluster. Evidence for velocity substructure was found by Fabricant *et al.* (1993), but it was disputed by Girardi *et al.* (1997), who used a larger redshift sample. The cluster has a rather high X-ray luminosity ($\sim$3 $\times 10^{44}$ ergs s^{-1}) in the 0.3-3.5 keV band (Fabricant *et al.* 1993; Melnick & Quintana 1981). Dressler (1980) gives the ratio E/S0/S: 31/46/23. A119, A147, and A168 form the core of a supercluster (Postman, Huchra, & Geller 1992).

Abell 2877

We use data from the fields of both Abell 2870 and Abell 2877 here. There is significant substructure in this region (Girardi *et al.* 1997). We detect three condensations projected onto the sky near the core of A2877 (to the North, North-east, and to the South [A2870]) and one substructure behind A2877 in redshift space. We coin this background group as "A2877b".

Abell 160

This is a low density cluster whose central region contains a first ranked galaxy with four optical components, possibly due to multiple nuclei or a satellite system

(Giovannini *et al.* 1987). The associated radio source is in the form of a $\sim 8'$ long collimated two-sided jet.

Abell 168

Abell 168 is a low density cluster rich with spiral galaxies to which Dressler (1980) gives the morphological ratio E/S0/S as 22/40/38. Surprisingly, this cluster also has a well-defined core and is rather regular. There is tentative evidence for a somewhat flat faint end LF for this system (Dressler 1978; Oegerle *et al.* 1986) and both Dressler and Ulmer *et al.* (1992) present evidence that A168 has an unusual core. Dressler points out that the BCG is well-removed from the optical central concentration, and Ulmer and coworkers verify a serious discrepancy between the optical and the X-ray centers. This suggests that A168 is a merging cluster, though Tomita *et al.* (1996) did not find a line of starbursting galaxies between the cores of the two substructures, a phenomenon that would support a merger scenario. This cluster is in the center of a supercluster along with A119 and A147 (Postman, Huchra, & Geller 1992).

Abell 194

This is a regular but linear cluster - the brightest members (mostly S0s) form a filamentary structure. Several studies have been undertaken to better understand the implications of the structure. Nemiroff *et al.* (1985) quantified the non-spherical nature of A194: the cluster has a minor/major axis ratio of $b/a = 0.72$, with the major axis at a position angle of $128°$. Though not conclusively, the individual galaxy PAs tend to line up either parallel or perpendicular to the cluster filamentary chain. More recent work by Chapman *et al.* (1988) found no support for a "pancake" model of cluster formation, as the distribution of galaxy PAs was established to be consistent with isotropy. Finally, Chapman and collaborators found no evidence for morphological segregation, in the velocity or spatial distributions. Dressler (1980) and Oemler (1974) give a similar spiral fraction for A194: E/S0/S = 26/48/26 and 18/56/26, respectively.

Abell 260

This cluster is a Bautz-Morgan type II. It is well behind the Perseus-Pisces Supercluster.

Abell 397

A spiral rich cluster in the direction of large line-of-sight Galactic extinction ($\sim$0.3 mags in I band).

Abell 3193

A cD-dominated cluster probably associated with A3202.

Abell 3266

Abell 3266 is a richness class 2 cluster and was one of the first X-ray sources found at southern declinations. It has a central dumb-bell galaxy with cD properties. Quintana *et al.* (1996) carried out a detailed analysis of the velocity dispersion in A3266: σ = 1306 km s^{-1} for the inner 1.25h^{-1} Mpc, 800 km s^{-1} outside of 1.5h^{-1} Mpc, and 1084 km s^{-1} overall. They found evidence for a merger in the cluster in the form of significant substructure, and merger models show the dumb-bell would be the result of two BCGs. Such a merger picture is consistent with the distorted X-ray profile. Supernova 1997A was discovered in a cluster galaxy by J. Maza *et al.* (1997).

Abell 496

Abell 496 is a favorite source for cooling flow studies. Several studies suggest the cooling accretion rate is $\sim$200 $M_\odot$ yr^{-1} onto the cD (Nulsen *et al.* 1982; Mushotzky & Szymkowiak 1988; Canizares *et al.* 1988). Further work on the intracluster medium (ICM) near the cluster core indicates that it is the site of metal enhancement (White *et al.* 1994; MacKenzie, Schlegel, & Mushotzky 1996) and that it is bound to the cD (Quintana and Ramirez 1990). There is some evidence for a background satellite group to the NW (this work and Mazure *et al.* 1986). Dressler gives the following morphological ratios: 22/50/28. There is rather large line-of-sight Galactic extinction in this direction ($\sim$0.3 mags in I band).

Abell 3381

A richness class 1 cluster with a possible foreground group in its field.

Abell 3407

We use data from the fields of both Abell 3407 and Abell 3408 here. These clusters are at low galactic latitude ($-18°$), and possibly are associated with the clusters S0601 and S0602. Campusano, Kneib, & Hardy (1998) discovered a gravitational arc (z=0.073) in A3408, and they tentatively consider the source to be a background spiral galaxy.

Abell 569

This is a Bautz-Morgan type II cluster possessing a dominant elliptical galaxy associated with a wide-angle tail radio source (Feretti *et al.* 1985). There is a group/cluster of galaxies just to the north (declination 50°) which Fanti *et al.* (1982) claim is at a similar redshift. The cluster is possibly connected, through the ZoA, to the Pisces-Perseus Supercluster (Chamaraux *et al.* 1990).

Abell 634

This is a type III Bautz-Morgan cluster that is quite well-defined both spatially and dynamically.

Abell 671

Abell 671 contains a number of gas rich spirals within one Abell radius.

Abell 754

Abell 754 is a classic case of a cluster merger. Numerical and observational studies indicate that an off-axis merger between two clusters have recently merged to form the present cluster (Roettiger *et al.* 1998; Henriksen & Markevitch 1996; Zabludoff & Zaritsky 1995; Henry & Briel 1995). The evidence comes in many forms, namely: (i) the disparate X-ray and optical distributions, (ii) the peak of the X-ray gas forms a line that is perpendicular to the purported collision axis, and (iii) an X-ray component is among the hottest observed in any cluster, suggesting compression-heated gas. Dressler (1980) gives the following morphological ratios: E/S0/S: 18/53/29

Abell 779

This is a cD cluster, with the dominant core members being of S0 and E morphologies (Fanti *et al.* 1982). A sparse cloud of galaxies between one and two Abell radii surrounds the core. Some radio sources are associated with the brightest members (Wilson & Vallee 1982). A large sample of HI (Haynes *et al.* 1997) and RC profiles (Vogt 1995) were available previous to this study.

Abell 957

This is an Abell richness 1 cluster with a dominant cD galaxy. Dressler (1980) gives the following morphological ratios: E/S0/S=12/48/40.

Abell 1139

This is a Bautz-Morgan type III cluster with the following morphological ratios: E/S0/S=5/45/50 (Dressler 1980).

Abell 1177

This is a very low density cD cluster. The three clusters A1177, A1185, and A1267 are the dominant members of a local supercluster (Postman, Huchra, & Geller 1992).

Abell 1213

A study of the core of Abell 1213 by Egikian *et al.* (1985) revealed that roughly half of the total luminosity is within the central 0.5 Mpc. A strongly polarized radio source is associated with the central twin pair of elliptical galaxies (Fanti *et al.* 1982). Abell 1185 is a nearby foreground cluster.

Abell 1228

This is a richness class 1 irregular cluster that has a high proportion of spirals; Oemler (1974) claims the morphological ratios are similar to those found in the field: E/S0/S=14/25/63.

Abell 1314

This is a regular cluster with many ellipticals — E/S0/S = 38/43/19 (Oemler 1974). Radio surveys have found no "relics" (i.e. radio sources with no optical counterparts; Vallee & Roger 1989) and one very interesting radio source: Abell 1314 is home to an extreme head-tail source, with a length of $17'$, or $\sim 350h^{-1}$ kpc (Vallee & Roger (1987).

Abell 3528

Abell 3528 is a richness class I cluster behind the core of the Shapley Supercluster, the richest nearby supercluster of galaxies. There is strong evidence for

A3528 to be a merger in progress, with high ICM gas temperature between the two subclusters, tailed radio morphologies, and steep radio spectra as supporting characteristics (Schindler 1996; Reid, Hunstead, & Pierre 1998).

Abell 1736

This cluster is a spiral rich system (E/S0/S=14/37/49; Dressler 1980) that is part of the Shapley Supercluster. There are at least two structures in the field of A1736 (this work and Dressler & Schectman 1988); we refer to the background system as "A1736b."

Abell 3558

Abell 3558, along with A3556 and A3562, is part of a single elongated structure that represents the core of the Shapley Supercluster (Bardelli *et al.* 1994; Bardelli *et al.* 1996). A3558 itself is the second richest cluster in the Abell catalog and contains significant substructure, with a bimodal X-ray core as one property that suggests a merger scenario (Dantas, de Carvalho, & Capelato 1997; Markevitch & Vikhlinin 1997).

Abell 3566

We use data from the fields of both Abell 3564 and Abell 3566 here. This is yet another region of the Shapley Supercluster (Quintana *et al.* 1997).

Abell 3581

This is a sparse cluster well in front of the Shapley Supercluster (Quintana *et al.* 1997).

Abell 1983

The field of A1983 is spiral rich (E/S0/S=18/36/46; Dressler 1980) and contains two condensations, the closer of which we call "A1983b." In addition, our eponymous "A1983" may have substructure as well (Girardi *et al.* 1997). Dressler & Schectman (1988) show that the velocity dispersion of A1983 drops monotonically with cluster radius, except for the cold core.

Abell 2022

This cluster has a sparse collection of spiral galaxies.

Abell 2040

Abell 2040 is a spiral rich cluster: E/S0/S=15/35/50 (Dressler 1980). Abell 2055 is a foreground system to the SE.

Abell 2063

This cluster is spiral rich out to two Abell radii. Evidence for significant substructure is given by Girardi *et al.* (1997). Dressler (1980) gives the following morphological ratios: E/S0/S=14/49/37.

Abell 2147

The clusters A2147, A2151 and A2152 form the Hercules cluster. A2147 is a cluster without a true core and has a spiral population that tends to eschew the central regions. This cluster is also spiral rich (Tarenghi *et al.* (1980) give E/S0/S as 27/31/42) and has a strong X-ray emitting gas, making this cluster a favorite laboratory for the study of galaxy-ICM interaction studies (Giovanelli, Chincarini, & Haynes 1981).

Abell 2151

This is the dominant member of the three clusters comprising the Hercules Supercluster, a system that is possibly gravitationally bound (Barmby & Huchra 1998). A2151 is also quite spiral rich, but unlike A2147, most of the spiral population is within one Abell radius of the cluster center. A recent CCD-based morphological study by Maccagni, Garilli, & Tarenghi (1995) indicates an extremely high spiral fraction in A2151: E/S0/S=15/20/65. Evidence for gas stripping is also present in A2151 (see, for example, Huang & Sarazin 1996).

Abell 2256

Abell 2256 is a rich, relaxed cluster that is similar to the Coma cluster in X-ray luminosity, mass, and galactic distribution (Fabricant, Kent, & Kurtz 1989). It is one of the most well-studied clusters in the Abell catalog thanks to its dense ICM. Interesting properties include a northern radio halo, several head-tail radio sources, and aspherical X-ray and optical mass distributions (Rottgering *et al.* 1994; Fabian & Daines 1991; Fabricant, Kent, & Kurtz 1989). This cluster is strongly associated with A2271 and A2296 (Postman, Huchra, & Geller 1992). A Sunyaev-Zel'dovich detection is available (Myers *et al.* 1997).

Abell 2295

This field is spiral rich, comprised of two superimposed clusters well separated in redshift. We have dubbed the further cluster, the most distant system in our sample, as "A2295," while the nearer cluster is referred to as "A2295b." Only one object was found at the nominal redshift listed in ACO ($z \sim$0.05).

Abell 3656

This is a richness class 0, Bautz-Morgan type I-II cluster. Our work suggests the presence of two background clusters.

Abell 3667

This is a flattened, dynamically regular cluster dominated by two D type galaxies. X-ray data suggest that the group of galaxies surrounding the fainter D galaxy is merging with the main cluster (Knopp, Henry, & Briel 1996; Sodre *et al.* 1992).

Abell 3716

This is a spiral rich cluster, with a probable subcluster to the north of and behind the main cluster (Girardi *et al.* 1997).

Abell 3744

Dominated by several early type galaxies in the core, Abell 3744 is another example of a cluster with many gas rich spirals. Substructure exists, and is most obvious to the north.

Abell 2457

Abell 2457 is a richness class 1 cluster. Most spirals are outside the core.

Abell 2572

Abell 2572 is most likely a group of galaxies that has been mislabeled as a cluster due to the presence of Hickson's Compact Group 94 (HCG94), which in turn is probably the true "cluster" in this region (Ebeling *et al.* 1995). The combined system A2572/HCG94 is in the northwestern portion of a supercluster that also contains A2589, A2593, and A2657 (Postman, Huchra, & Geller 1992).

Abell 2589

Abell 2589 is part of the supercluster described above; A2572, A2589, and A2593 form the core of this large-scale system. This cluster is Bautz-Morgan type I and has morphological ratios of E/S0/S=19/55/26 (Dressler 1980).

Abell 2593

Abell 2593 is also a member in the supercluster described above. There are numerous gas-rich spiral galaxies in this cluster.

Abell 2657

This is the remaining member of the supercluster mentioned above, but is not within the supercluster "core." Most of the gas rich spiral galaxies in A2657 are about one Abell radius from the nominal cluster center. Dressler (1980) quotes the morphological ratios as E/S0/S=18/48/36. There is rather large line-of-sight Galactic extinction in this direction ($\sim$0.25 mags in I band).

Abell 4038

Abell 4038 is a spiral rich, regular cluster with a large redshift database available. We find possible evidence for substructure at 9300 km s^{-1} and 10,000 km s^{-1}.

Chapter 3

Imaging

3.1 Introduction

This study essentially is a comparison between a distance-dependent parameter (galaxy flux) and a distance-independent quantity (galaxy rotational velocity). Direct imaging provides the distance-dependent measurement and spectroscopy yields the distance-independent variable. This chapter details the imaging performed and the methods used to process the data, from the original "raw" state obtained at the telescope to the final "reduced" state from which physical quantities are extracted. Section 3.2 summarizes the observing setup and the techniques used to reduce the optical images. Section 3.3 explains the necessary corrections we apply to I band magnitudes and Section 3.4 details how we account for seeing-affected ellipticities. The last section covers our checks for internal consistency in the photometry.

Table 3.1 Imaging Observing Runs

	Run 1,2,4,6-9	Run 3,5	Run 10-12,14	Run 13
Telescope	KPNO 0.9 m	CTIO 0.9 m	KPNO 0.9 m	CTIO 0.9 m
CCD	T2KA	Tek2k3	T2KA	Tek1k3
Pixels	2048 x 2048	2048 x 2048	2048 x 2048	1024 x 1024
Read-out noise	4 e^-	4 e^-	4 e^-	5.8 e^-
Gain	5.4 e^-/DU	3.21 e^-/DU	3.6 e^-/DU	3.70 e^-/DU
Pixel scale	0.68″	0.396″	0.68″	0.396″
Field of view	23.2' x 23.2'	13.5' x 13.5'	23.2' x 23.2'	6.8' x 6.8'

	Run 1[a]	Run 2[a]	Run 3	Run 4
Dates	4/12-4/19/94	10/5-10/16/94	2/1-2/8/95	2/27-3/6/95
Phot. nights	4	6	4	0
Marg. nights	2	3	3	1
Galaxies	29	13	46	7

	Run 5	Run 6	Run 7	Run 8
Dates	8/28-9/4/95	9/14-10/1/95	11/20-11/26/95	2/13-2/19/96
Phot. nights	7	6	2	2
Marg. nights	0	3	2	1
Galaxies	113	120	33	82

	Run 9	Run 10[a]	Run 11[a]	Run 12[a]
Dates	4/8-4/13/96	10/31-11/13/96	2/4-2/16/97	4/9-4/15/97
Phot. nights	4	6	7	4
Marg. nights	1	2	1	0
Galaxies	26	5	7	15

	Run 13[a]	Run 14[a,b]		
Dates	4/28-5/2/97	5/20-5/24/98		
Phot. nights	4	2		
Marg. nights	1	2		
Galaxies	3	5		

[a] Observing run mainly dedicated to a different project; only a small portion of telescope time dedicated to this project.
[b] This most recent KPNO run used a 8kx8k engineering-grade CCD to image A3581. The pixel size was 0.40″, the field of view 59′.

3.2 I Band Imaging

The imaging was carried out at the Kitt Peak National Observatory (KPNO) and the Cerro Tololo Inter-American Observatory (CTIO) 0.9 m telescopes[1]. All photometric observations were carried out in the I band (Kron-Cousins filter, central wavelength of 8075 Å [8290 Å] and passband of 1500 Å [1950 Å] for the CTIO [KPNO] observations) to match the observations of the nearby cluster Tully-Fisher study of G97a,b and for the reasons outlined therein. Table 3.1 highlights pertinent information for the runs associated with this work. The cluster fields that have been imaged are discussed in Chapter 5 and can be seen in the collection of figures given in the appendix. Exposures for each frame amounted to 600 seconds, a time sufficient to reliably reach isophotal levels near 24.5 mag arcsec^{-2} and generally not long enough to produce saturated galactic cores. The only significant difference between imaging at KPNO and CTIO for our cluster sample is the higher spatial resolution for the data taken at the CTIO 0.9 m telescope ($0.4''$ pixel^{-1} vs. $0.68''$ pixel^{-1}), and a smaller field of view ($14' \times 14'$ vs $23' \times 23'$) for the 2048^2 pixel CCDs. The seeing conditions for our data is displayed in Fig. 3.1. The average FWHM seeing for the images was $1.6'' \pm 0.3''$ at KPNO and $1.4'' \pm 0.2''$ at CTIO; however, the nights with the best seeing conditions were preferentially devoted to the more distant clusters. The majority of the data presented here were taken in good photometric conditions, for which the photometric zero-point calibration could be determined with an accuracy of 0.02 mag or better. In a minority of cases (2%), photometric conditions were of

[1]KPNO and CTIO, National Optical Astronomy Observatories (NOAO), are operated by the Association of Universities for Research in Astronomy, Inc., under a cooperative agreement with the National Science Foundation.

inferior quality. In those cases, frames were taken with a substantial sky overlap with images taken in good photometric conditions, so that fluxes of at least 12 field stars could be measured in the overlap region, thus guaranteeing calibration to the ∼0.03 mag level.

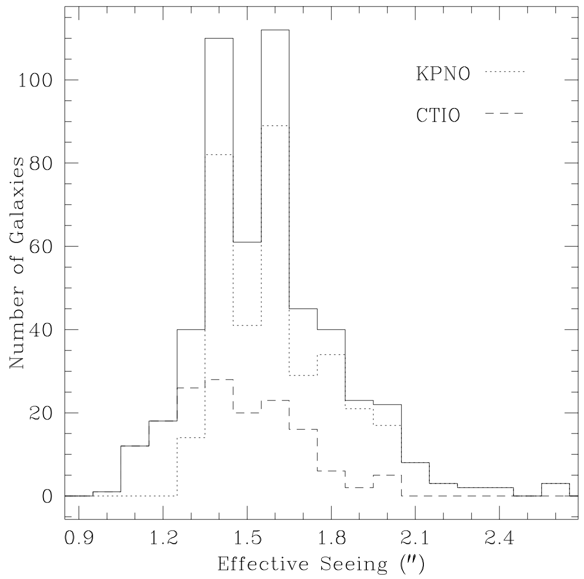

Figure 3.1 The distribution of effective seeing for the galaxy observations. The dotted line is for KPNO observations, the dashed line is for CTIO observations, and the solid line is the sum of the two distributions.

3.2.1 Data Reduction

We have made an effort to employ a method of data reduction consistent with the G97 reductions. Both standard and customized IRAF[2] packages are used. All frames are first bias subtracted to remove any unwanted signal that arises during CCD readout. This is done through the use of a median-combined frame of ∼30 zero second exposures. For the CCDs used, this structure only varies by

[2]IRAF (Image Reduction and Analysis Facility) is distributed by the National Optical Astronomy Observatories, which are operated by the Association of Universities for Research in Astronomy, Inc. (AURA), under a cooperative agreement with the National Science Foundation.

a few counts ($< 1\%$) across the entire CCD. The frames are then trimmed to include only sufficiently illuminated portions of the chip.

The next step is to obtain adequately "flat" images, the process whereby spurious structure from pixel-to-pixel variations in quantum efficiency, non-uniform illumination, or dust shadows is removed. This process is among the most crucial of the reduction tasks, due to the increased sky fluctuations present in the infrared, relative to the optical bands. Sky flats are not adequate at this wavelength due to the large number of frames required and the limited amount of available twilight. As such, we create flat-field templates by median-combining 30-50 frames that are free from relatively bright stars and relatively large galaxies. The construction of the R band flat, necessary for the standard star frames taken at that wavelength, is relatively straightforward. A simple median combination of 5-7 twilight flats taken during dusk or dawn is sufficient to create a good flat field image. Once flat-fielded, each galaxy frame is background corrected by subtracting off the mean value of several sky regions near the galaxy that are free from stars or significant cosmic ray hits. This step is done separately for each galaxy in a 500×500 pixel frame – reducing the galaxy frame size eases book-keeping and cpu strain. The uncertainty in the sky background is less than 0.2%. Moreover, cosmic rays and also any stars near the galaxy are masked to prevent distortions of the ensuing isophotal ellipse fitting, a procedure that interpolates over masked regions.

3.2.2 Isophotal Ellipse Fits

The procedure of ellipse fitting employs the GALPHOT surface photometry package written for IRAF/STDAS[3] by W. Freudling, J. Salzer, and M.P. Haynes. We fit ellipses to increasing galactic radii until the background is reached. The bulk of the instrumental magnitude is determined from data within the outermost isophote, but a small yet non-zero contribution, found by extrapolating the "curve of growth" of the surface magnitude of each spiral galaxy to eight (face-on) disk scalelengths (assuming the light drops like that of an exponential disk), is also included (see Giovanelli *et al.* 1994, hereafter G94, for details on this procedure) to infer a "total" magnitude, m_∞. This contribution is typically a few hundredths of a magnitude. The reason for extrapolating to only $8r_{\rm d}^{\circ}$ instead of to infinity comes from such work as van der Kruit & Searle (1981) and Corbelli, Schneider, & Salpeter (1989), who find that disk profiles generally are truncated at radii of order 5 scalelengths. Figure 3.2 displays surface brightness profiles for the first sixteen galaxies in the sample. The vertical dashed line refers to the optical radius, r_{83}, the distance along the major axis to the isophote containing 83% of the I band flux. The solid line drawn along the disk is the fit to the disk over the range of radii assumed to cover the exponential portion of the disk. We have also calculated the values of the isophotal magnitude, $m_{23.5}$, measured at the 23.5 mag arcsec^{-2} isophote. Errors on $m_{23.5}$ and m_∞ (denoted σ_∞) typically hover between 0.02 and 0.04 mag – the corrections for internal extinction introduce further uncertainty, as discussed in the next section.

[3]STSDAS (Space Telescope Science Data Analysis System) is distributed by the Space Telescope Science Institute, which is operated by AURA under contract to the National Aeronautics and Space Administration.

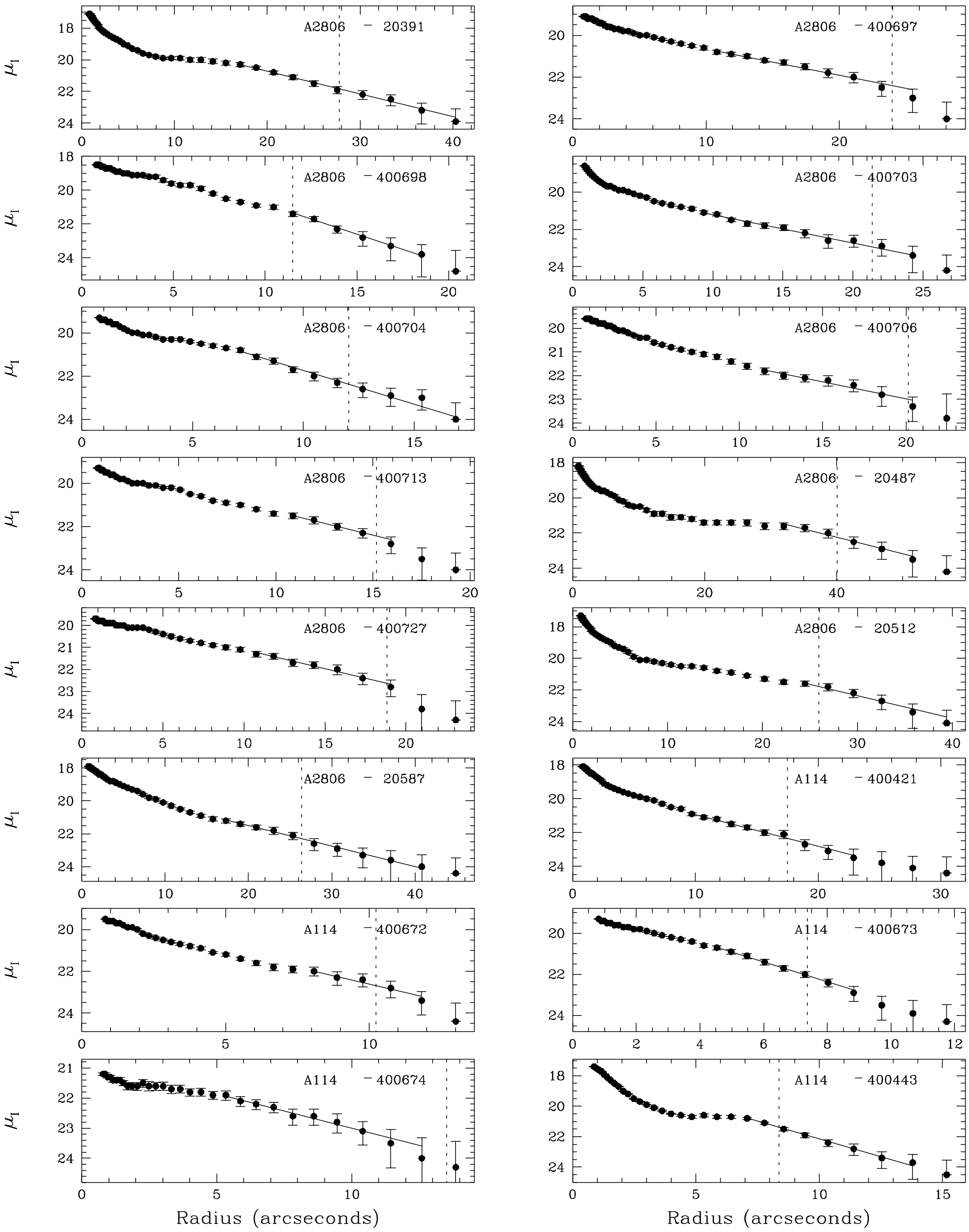

Figure 3.2 A sampling of surface brightness profiles. Names of the galaxy and the corresponding parent cluster are given in each panel. Two lines are drawn: the vertical dashed line is drawn at r_{83} and the solid line is an exponential fit to the disk, over the range of radii over which the disk is assumed to behave exponentially.

An important result of this exponential profile fit is the extraction of the ellipticity of the disk. The disk region is the range of radii where the surface brightness profile drops linearly and the position angles, ellipticities, and centers of the fitted ellipses are approximately unchanging and reliable. A galaxy's ellipticity is usually assigned the mean of its disk region's ellipticities, but in some cases it is estimated by eye. The disk ellipticity found here is central to correcting for internal extinction and deprojecting rotational velocity widths. We discuss in detail the process of determining "true" disk inclinations in Section 3.4.

3.2.3 Flux Calibration

Instrumental magnitudes are converted to apparent magnitudes using Landolt (1992) standard stars. The selection of Landolt fields to monitor each night were governed by two factors: i) observations of a broad range of $R-I$ colors are necessary to adequately quantify color systematics inherent to the instrumental setup, and ii) one or two fields should be observed several times a night at different airmasses to provide information on flux loss as a function of airmass. Exposure times varied; integrations were optimized to provide standard star intensity peaks of at least several thousand counts, without saturating the CCD. The relation fit to the standard star data is

$$M = m + A_0 + A_1(R-I) + A_2(airmass) \tag{3.1}$$

where M is the standard magnitude and m is the observed instrumental magnitude. We find a small dependence on airmass ($A_2 \sim$0.1 mag airmass^{-1}; note that normal observations are done through less than 1.5 airmasses) and a negligible color effect. This is fortunate since we only have I band images; assuming an

Table 3.2 *I* Band Galactic Extinction

Cluster	BH	SFD	Cluster	BH	SFD	Cluster	BH	SFD
A 114	0.020	0.036	A1228	0.022	0.047	A2657	0.106	0.248
A 119	0.033	0.076	A1314	0.000	0.032	A2806	0.000	0.030
A 160	0.045	0.169	A1736	0.118	0.114	A2877	0.000	0.023
A 168	0.041	0.068	A1983	0.000	0.052	A3193	0.000	0.026
A 194	0.073	0.083	A1983b	0.004	0.038	A3266	0.000	0.036
A 260	0.073	0.095	A2022	0.014	0.055	A3381	0.000	0.073
A 397	0.200	0.298	A2040	0.024	0.084	A3407	0.094	0.164
A 496	0.037	0.267	A2063	0.033	0.067	A3528	0.151	0.152
A 569	0.163	0.140	A2147	0.022	0.063	A3558	0.086	0.099
A 634	0.043	0.108	A2151	0.028	0.094	A3566	0.063	0.115
A 671	0.055	0.092	A2256	0.084	0.103	A3581	0.084	0.120
A 754	0.079	0.130	A2295	0.082	0.098	A3656	0.173	0.142
A 779	0.000	0.033	A2295b	0.082	0.088	A3667	0.088	0.096
A 957	0.016	0.083	A2457	0.090	0.165	A3716	0.033	0.068
A1139	0.031	0.061	A2572	0.063	0.100	A3744	0.114	0.126
A1177	0.000	0.035	A2589	0.022	0.059	A4038	0.018	0.037
A1213	0.000	0.036	A2593	0.051	0.085			

$R-I$ galactic color of 0.5 mag yields negligible color corrections. Finally, we reemphasize that we use only data taken on nights where the photometric zero point, A_0, is determined to 0.02 mag or better.

3.3 Corrections to I Band Magnitudes

We have limited our survey to $|b| \gtrsim 20°$due to the heavy extinction encountered at low Galactic latitudes. One approach to correcting for extinction due to our own galaxy is to use Burstein & Heiles' (1978) method for tabulating Galactic extinction values by averaging entries in the *Third Reference Catalogue of Bright Galaxies* (de Vaucouleurs *et al.* 1991) found near the cluster centers. Burstein & Heiles used Galactic HI column densities to infer reddening values assuming either a constant gas to dust ratio (southern declinations) or a ratio that can vary (northern declinations), as indicated by counts of background galaxies. Recent work by Schlegel, Finkbeiner, and Davis (1998) has improved upon the accuracy of Galactic reddening estimates through the use of relatively high resolution COBE/DIRBE and IRAS/ISSA dust maps. Table 3.2 shows the I band foreground extinction values obtained from both methods. We adopt the estimates obtained from the work of SFD, who claim an accuracy of 15% in their values: $\sigma_A \equiv 0.15 A_I$. Values of A_I for sample of clusters range from 0.02 to 0.30 magnitudes.

The correction for internal extinction, the absorption of light within other galaxies, is applied using the procedure outlined in G97a, whereby the decrease in apparent luminosity of late-type galaxies due to their dusty disks can be quantified as

$$\Delta m_{\rm int} = -f(T)\gamma(W_{\rm cor})\log(1-e). \tag{3.2}$$

The parameter $\gamma(\lesssim 1.0)$ depends on the corrected velocity width $W_{\rm cor}$ (see Chapter 4) and e is the ellipticity of the spiral disk (the correction $\Delta m_{\rm int}$ is slightly smaller for early, less dusty galaxies: $f(T)$=0.85 for types T earlier than Sbc; $f(T)$=1 otherwise). In other words, the internal extinction depends on the size of the system and on how inclined the disk is to our line of sight. An error for γ of $\sigma_\gamma = 0.15\gamma$ is assumed. We apply a cosmological k-correction: k_I=(0.5876-0.1658T)z (Han 1992). Finally, we are careful to apply a small correction, Δm_T, for the TF dependence on morphological type discussed in Chapter 6. Thus, the apparent magnitudes given are

$$m_{\rm cor} = m_\infty - A_I - k_I - \Delta m_{\rm int} - \Delta m_T. \tag{3.3}$$

While the true, unextincted, face–on apparent magnitude of the galaxy is $m_{\rm cor} +$

$\Delta m_T, m_{\rm cor}$ represents the value to be used in TF work with the template TF relation obtained in G97b, characterized for Sbc and Sc galaxies. Thus $\Delta m_T = 0$ for types Sbc and later; the correction is 0.1 mag for Sb types and 0.32 mag for types earlier than Sb.

Given that the inferred absolute magnitude is thus

$$M_{\rm cor} - 5\log h = m_{\rm cor} - 5\log\left(\frac{{\rm c}z[{\rm km\ s^{-1}}]}{100}\right) - 25, \tag{3.4}$$

standard error analysis yields the following relation for the I band magnitude errors:

$$\sigma_M^2 = \sigma_\infty^2 + \sigma_A^2 + \sigma_k^2 + (f(T)\log(1-e)\sigma_\gamma)^2 + \left(f(T)\log e\frac{\sigma_e}{1-e}\right)^2 + \sigma_T^2 + \left(5\log e\frac{\sigma_{{\rm c}z}}{{\rm c}z}\right)^2 \tag{3.5}$$

The ellipticity error σ_e comes from a fit to the range of ellipticities along the disk, whereas the uncertainties in the k and morphological type correction, σ_k and σ_T, are set to one-fourth their respective correction's amplitude.

3.4 Inclination Corrections

Knowledge of the true rotational velocity widths of galaxies is crucial to TF studies, yet many circumstances combine to yield incorrect measurements. Among these circumstances in optical spectroscopy work are misalignment of the slit with the major axis of the galaxies and insufficient integration times that prevent unambiguous measurements in the outer parts of the ORC. The largest error contribution to estimates of the velocity width in general derives from uncertainty in the angle of inclination, i, of the disk to the line of sight. As described in detail in Chapter 4, this geometric effect can be easily accounted for by dividing the observed velocity width by sin$i$. In addition, a knowledge of the correct ellipticity of a disk is important in the derivation of the internal extinction correction to the total magnitude, as discussed in Section 3.3. It is the ability to correctly measure the ellipticity that we are concerned with here.

It is well-known that ground-based observations are affected by the atmospheric seeing conditions. Saglia *et al.* (1993; S93) have recently provided a thorough analysis concerning the effects of seeing on spheroidal systems. The turbulent atmosphere increasingly affects the observed ellipticities, $\epsilon_{\rm obs}$, as the angular size of galaxies decreases. Here we consider that effect on spiral disks.

3.4.1 Measuring True Ellipticities

In order to gauge the relationship between $\epsilon_{\rm obs}$ and the undistorted ellipticity $\epsilon_{\rm true}$, we have taken a sample of eleven large angular–sized galaxies (major axis $> 5'$) with a broad range of inclinations and bulge–to–disk ratios and blurred their (I band) images by convolving them with a point spread function (psf) of varying width. The galaxies used in this exercise are a mix of Sa and Sc type galaxies and have $\epsilon_{\rm true}$ ranging between 0.311 and 0.865 and bulge–to–disk ratios between 0 and 2. We assume that the unconvolved images yield $\epsilon_{\rm true}$.

It is necessary in this exercise to mimic the actual seeing profile as closely as possible. Though the seeing quality for an observation is typically conveyed by measuring the FWHM of a Gaussian fit to a stellar profile, it is known that stellar profiles do not drop as steeply outside of their cores as Gaussians do (Woolf 1982). To simulate this effect we have followed the method of S93 which employs atmospheric turbulence theory and empirical results to predict the stellar psf and its parameters. Letting the stellar psf be $p_\gamma(r)$, it can be shown that

$$p_\gamma(r) = \frac{1}{2\pi}\int_0^\infty dk\, k\, e^{-(kb)^\gamma} J_0(kr), \qquad \gamma = 5/3 \tag{3.6}$$

where r is the radial distance, J_0 is the standard Bessel function, b is FWHM/2.921, and γ is a parameter predicted to be 5/3 by theory.

For a fixed $\epsilon_{\rm true}$, we expect $\epsilon_{\rm true}/\epsilon_{\rm obs}$ to increase when either the size of the seeing disk increases or the angular size of the galaxy decreases. We have thus parameterized the change in ellipticity as a function of the ratio between the measured seeing FWHM and the face–on disk scalelength, $r_{\rm d}^\circ$ (see G94 for details on measuring $r_{\rm d}^\circ$). We thus define

$$\eta \equiv \frac{\rm FWHM}{r_{\rm d}^\circ}. \tag{3.7}$$

We have convolved each galaxy image with a range of values for η and measured the resulting ellipticities. Figure 3.3 gives our results for the eleven galaxies used in this study, plotting $\epsilon_{\rm true}/\epsilon_{\rm obs}$ as a function of η. We find that, within the uncertainties of our simulations, the change in the ratio $\epsilon_{\rm true}/\epsilon_{\rm obs}$ is independent of disk inclination and bulge–to–disk ratio. Fitting a linear relation to the data gives us a general method for estimating $\epsilon_{\rm true}$ as a function of the observable quantities $\epsilon_{\rm obs}$, FWHM, and $r_{\rm d}^\circ$. We see that the change in ellipticity is not severe; there is only a $\sim$10% difference even for $\eta \sim 1$, the extreme case when the seeing is comparable to the disk scalelength. More exactly,

$$\epsilon_{\rm true} = \epsilon_{\rm obs} + 0.118\, \eta\, \epsilon_{\rm obs} \tag{3.8}$$

where the 1-σ errors in the offset and slope are 0.004 and 0.011, respectively.

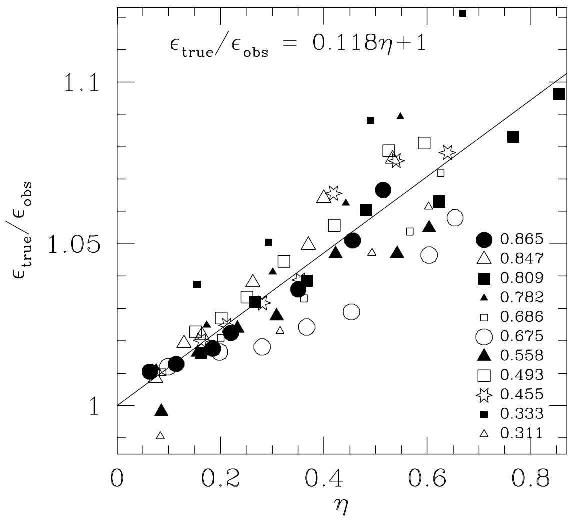

Figure 3.3 Results of simulations on the effects of seeing on disk ellipticities. η is the ratio of the seeing FWHM to $r_{\rm d}^{\circ}$. Plotted are the data points for simulations carried out on 11 galaxies of differing bulge–to–disk ratios and ellipticities. The "true" ellipticities (as measured from the raw, unconvolved images) of these 11 galaxies are given in the lower right. We use the linear relation drawn to recover "true" ellipticities.

3.4.2 Examples of the Impact of Inclination Corrections

As mentioned previously, both the velocity width and the total magnitude depend on the disk inclination. Quantitative examples of the corrections applied are useful to get a feeling as to how TF parameters are changed. Suppose two Sc galaxies with total, edge-on velocity widths of 300 km s^{-1} are observed, with one inclined to the line of sight at 85.0° (galaxy 'A') and the other at an inclination of 48.0° (galaxy 'B'). This means the projected velocity widths would be 299 km s^{-1} and 223 km s^{-1}, respectively, for galaxies A and B (ignoring cosmological effects). Furthermore, suppose the sizes of the galaxies and the seeing conditions yield $\eta = 1.00$ in each case (an extreme value of η is chosen to understand what the magnitudes of the largest probable corrections would be). Thus, according to Equations (4.24) and (3.8), though galaxy A has a true disk ellipticity of 0.844 it will be observed to have an ellipticity of 0.755 ($i = 77.9°$). Similarly, galaxy B has $\epsilon_{\rm true} = 0.324$ but $\epsilon_{\rm obs} = 0.290$ ($i = 45.2°$). We see that without accounting for the circularizing effect atmospheric seeing has on these disks, one would incorrectly infer the velocity widths for galaxies A and B to be 306 km s^{-1} and 314 km s^{-1} instead of the actual 300 km s^{-1}.

Seeing also affects the correction for internal extinction. According to equation (3.2), galaxy A "should" have a correction of 0.742 mag and galaxy B 0.156 mag, but the observed axial ratios would imply corrections of only 0.562 and 0.137 mag.

This simple example highlights how seeing affects differently oriented disks. Without making the proper corrections for seeing, galaxies that are highly inclined would yield reasonable velocity widths but the internal extinction corrections for the galaxies would be uncomfortably awry. Conversely, galaxies considered to be borderline TF candidates due to their low inclinations are not affected greatly by miscalculating the internal extinction, but errors in determining the inclinations would produce velocity width errors of $\sim$5%.

3.5 Comparison of KPNO and CTIO Photometry

We review the internal consistency of the photometric data as a final check of its accuracy. All-sky surveys such as ours require observations from more than one telescope as well as observations from more than one semester. As such, it is necessary to determine in a quantitative manner the signature of any latent systematic biases that may exist.

Table 3.3 Internal Comparison of Photometry

Parameter	N	mean difference	rms scatter	mean uncertainty
m_∞ (mags)	30	0.008	0.062	0.050
$\epsilon_{\rm true}$	30	0.002	0.020	0.032
PA (°)	30	0.2	2.1	2.8
$r_{83}/r_{\rm d}$	30	0.04	0.3	—

Repeat observations (in photometric conditions) of galaxies were carried out i) occasionally in the same observing run, ii) frequently in a different observing run at the same telescope, and iii) sometimes in a different observing run at a different telescope in a different terrestrial hemisphere. Consistency of the data for case i) confirms (a) the reliability of photometric zero-points as well as (b) the reliability of the overall method of data reduction (i.e. sky background subtraction, isophotal ellipse fits, exponential disk fits, etc.). Uniformity in the data for case ii) implies conditions (a), (b), and (c) the lack of any season-to-season variations in the data. Finally, if the sequence of observing runs in both hemispheres is spread throughout the calendar year, then agreement between photometry taken from both hemispheres, case iii), assures conditions (a–c) are met and (d) that the data are free from systematics that are telescope-dependent. In short, checking for consistency within case iii) data can be sufficient to ensure overall internal consistency in the photometric data.

Haynes *et al.* (1998) study the systematics for cases i)-iii) in their SFI and SCI samples, the data for which have been processed in the same manner as outlined in this chapter. They find conditions (a–d) hold for their data to within the expected flux uncertainty, ~0.06 mags. We refrain here from delving into investigations of data uniformity for cases i) and ii) and instead proceed directly to testing the data for case iii). A sample of 30 galaxies (from six clusters) for which reliable KPNO and CTIO photometry exists was selected. Observations cover seven different months and four years. The data were processed in the same manner described above. Results are given in Table 3.3. The first column lists important photometric parameters for which KPNO/CTIO comparisons are made. The second column indicates the number of galaxies in the overlap sample. The third, fourth, and fifth columns display the mean difference between the observed parameters, the rms scatter in the difference (assuming equal weighting), and the mean uncertainty in the parameters (times $\sqrt{2}$ for a fair statistical comparison). The data exhibit no systematic dependencies on telescope site. Moreover, from this fact we can infer the data have been processed in a uniform manner from observing run to observing run and from season to season.

Chapter 4

Spectroscopy

4.1 Introduction

Though the 21 cm spectral line is a frequently adopted tool in TF work — the HI distribution in galaxies typically extends farther out than that of HII regions and thus samples spiral disk velocity fields at larger radii — the characteristics of our sample favor the use of optical spectroscopy. Too few radio telescopes exist with the sufficient sensitivity, spatial and velocity resolution, and bandwidth necessary for an all–sky survey of intermediate distance clusters. The dishes at Nançay and Arecibo would be useful, but they cannot cover the whole sky. In cluster fields at $cz \gtrsim 10^4$ km s^{-1}, confusion becomes a problem and, especially at Arecibo, the interference environment makes observations more difficult. Array instruments still have limited correlator power to cover the large bandwidth required for cluster observations with sufficient resolution. Furthermore, many cluster spirals are HI deficient (Giovanelli & Haynes 1985). For these reasons we have adopted emission line spectroscopy near the Hα line to measure velocity widths. The following section summarizes the observing setup and the techniques used to reduce the spectra. Later in the chapter we describe our approach to modeling rotation curves (Section 4.3) before we detail how we recover velocity widths from optical rotation curves, taking into account several systematic and observational biases (Section 4.4). Section 4.5 discusses the results of internal and external checks for consistency in the data and Section 4.5 explains the error determinations for the optical velocity widths.

4.2 Optical Spectroscopy

Rotational velocity widths for this sample of cluster galaxies were extracted from long–slit spectra obtained at the Palomar Observatory 5 m telescope and the CTIO 4 m telescope. Table 4.1 lists the observing runs and summarizes their technical setups. For the Palomar 5 m portion of this project we used the red camera of the Double Spectrograph (Oke and Gunn 1982) at the Cassegrain focus ($f/15.7$). The combination of the 1200 lines mm^{-1} grating and a $2''$ wide (and $2'$ long) slit yields a dispersion of 0.65 Å pixel^{-1} and a spectral resolution of 1.7 Å (equivalent to 75 km s^{-1} at 6800 Å). Along the cross–dispersion axis, the spatial scale is $0.468''$ pixel^{-1}. Since we have been interested in observing cluster members with redshift velocities of up to $\sim$30,000 km s^{-1}, the angle of the grating was set in order to observe the Hα line at wavelengths anywhere between 6550 Å ($\sim$ rest wavelength) and 7220 Å (cz $\sim$30,000 km s^{-1}). The observing setup at the CTIO 4 m uses the R–C Spectrograph and the Loral 3k CCD with a $203''$ long slit. The combination of the 1200 lines mm^{-1} grating and a $2''$ wide slit yields a dispersion of 0.55 Å pixel^{-1} and a spectral resolution equal to that of the data for the Palomar observations: 1.7 Å (equivalent to 75 km s^{-1} at 6800 Å). Along

Table 4.1 Spectroscopy Observing Runs

	Runs 1-3,5-7,9,12,13,16	Runs 4,8,10,11,14
Telescope	Palomar 5 m	CTIO 4 m
Instrument	DS-red camera	RC Spectrograph
CCD	Tek1024	Loral 3k
Pixels	1024 x 250	3060 x 390
Read-out noise	7.5 e^-	7.5 e^-
Gain	2.0 e^-/DU	1.9 e^-/DU
Spatial scale	0.468″/pixel	0.50″/pixel
Slit aperture	2″	2″
Grating	1200 l/mm	1200 l/mm
Dispersion	0.65 Å/pixel	0.55 Å/pixel
Spect. resolution	1.7 Å (75 km/s)	1.7 Å (75 km/s)
Wavelengths[a]	6550-7220 Å	6020-7680 Å

	Run 1	Run 2	Run 3	Run 4
Dates	10/22-10/23/95	12/13-12/18/95	1/24-1/25/96	4/4-4/7/96
Nights used	2	5	2	3
RCs	23	53	27	16
Hα rate	24/27	65/94	36/41	16/36

	Run 5	Run 6	Run 7	Run 8
Dates	5/14-5/15/96	7/9-7/12/96	9/13-9/19/96	9/30-10/3/96
Nights used	2	4	6	3
RCs	21	35	67	29
Hα rate	24/30	40/63	75/126	41/62

	Run 9	Run 10	Run 11	Run 12
Dates	3/6-3/7/97	3/26-3/28/97	4/25-4/27/97	5/3-5/4/97
Nights used	2	3	3	2
RCs	29	35	35	15
Hα rate	36/52	40/67	44/64	16/22

	Run 13	Run 14	Run 15	Run 16[b]
Dates	7/7-7/9/97	8/22-8/26/97	12/21-12/22/97	4/27-4/29/98
Nights used	3	5	1	3
RCs	32	51	17	10
Hα rate	39/49	61/110	20/33	18/34

[a] Run 4: 5640-7320 Å; 8: 5730-7410 Å; 14: 6410-8080 Å; 16: 6730-7400 Å

[b] Observing run mainly dedicated to a different project; only a small portion of telescope time dedicated to this project.

the cross–dispersion axis, the spatial scale is $0.50''$ pixel^{-1}. The wavelength range for the spectroscopy carried out at CTIO ($\sim$ 6020 Å to 7680 Å) is large enough to observe redshifted Hα emission in galaxies with recessional velocities up to $\sim$34,000 km s^{-1}, in our chosen setup.

As an observing strategy, we performed a five minute test integration on each spectroscopic target. In this way were are able to determine "on the fly" the requisite exposure time to adequately sample the outer disk regions. Furthermore, this test exposure determined if the galaxy was even useful to our work; the galaxy may lie in the foreground or background of the cluster or it may contain little or no Hα emission. If the observation was deemed useful, a second integration typically ranged between 15 and 45 minutes. We detected line emission in 582 out of 897 (65%) targeted galaxies observed in these fifty-two clusters.

4.2.1 Data Reduction

Standard and customized IRAF tasks were used in reducing the spectroscopic data. Initial reduction routines include bias correcting and flat-fielding; subsequent tasks concern rectifying frames and calibration. The spectra were wavelength calibrated using both night sky lines and HeNeAr comparison lamps. The residual uncertainties in the spectral calibration translate to a typical velocity uncertainty of $\sim$7 km s^{-1}, a figure which is added in quadrature to the errors from the rotation curve fitting (below) in determining the total error for each velocity data point. Flux calibration was not performed for these data. The night sky-lines and the galactic continuum were fit with polynomials and then subtracted from the spectra. Finally, the Hα rotation curve (RC) was computed. In $\sim$2% of the cases the emission of a [NII] line (6584 Å) was stronger and extends to larger radii than that of the Hα emission; in these cases the [NII] curve was used. Using software developed by K. Jore, at each position along the cross–dispersion axis we have fit a Gaussian profile to the light distribution (averaged over three pixels in the spatial direction). The position of the Gaussian peak was taken to be the line centroid for that spatial location. Since the seeing was typically $1''$ to $2''$, the rotation curves are oversampled by a factor of two to three. The galactic center-of-light was defined to be at the peak of the galaxy continuum light profile formed by summing the data along the dispersion direction.

4.2.2 Systemic Velocities

It is necessary to extract two parameters from each rotation curve: the systemic velocity (i.e. redshift) and the Doppler velocity width. In an idealized galaxy, where both arms of the rotation curve are smoothly traced out beyond the turnover radius, only the two velocity extrema are needed – the average of the extrema is the systemic velocity and the difference is the velocity width. Unfortunately, rotation curves can exhibit erratic behavior. The determination of velocity widths as derived from long-slit optical rotation curves has received much attention in the recent literature (Raychaudury *et al.* 1997; Courteau 1997; Giovanelli *et al.* 1998b, hereafter G98b), and we will consider it fully in the following section. We concentrate here on calculating the systemic velocity from an observed RC.

The systemic and rotational velocity extracted from an observed rotation curve depends on whether a photometric or kinematic center of symmetry is assumed. In the first case, the systemic velocity is assigned the value at the location where the galaxy light peaks. In the upper panel of Figure 4.1, the

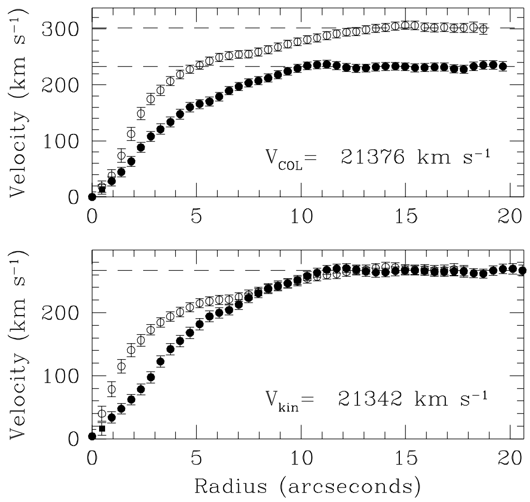

Figure 4.1 A comparison of folding techniques. The upper panel gives an RC folded about the galactic *center–of–light* whereas the lower panel displays the RC folded about the *kinematic* center of the galaxy. The redshift of the galaxy changes by only 34 km s^{-1} and the radii are shifted by only $0.94''$, but the effect is striking. We adopt the lower panel convention.

rotation curve is folded about such a photometric center, exhibiting asymmetry in the outer parts. Alternatively, by forcing a match between the asymptotic rotational velocity in the outer parts of the galaxy, a "kinematical centering" can be obtained. To facilitate this approach, we sort the velocity data points and calculate the average of the 10% and 90% velocities (an N% velocity is greater than N% of all the velocity data points). This technique is effectively a "pixel histogram," similar in flavor to the portrayal of raw 21 cm data. The kinematic center is merely the average of the 10% and 90% velocities: $cz \equiv (V_{90\%} + V_{10\%})/2$. In the lower panel of Figure 4.1, the rotation curve of the same galaxy in the upper panel is folded about the kinematic center, which is shifted from the photometric center by $0.94''$. The systemic velocity differs by 34 km s^{-1} between the two cases. In what follows, we will adopt the kinematical centering technique.

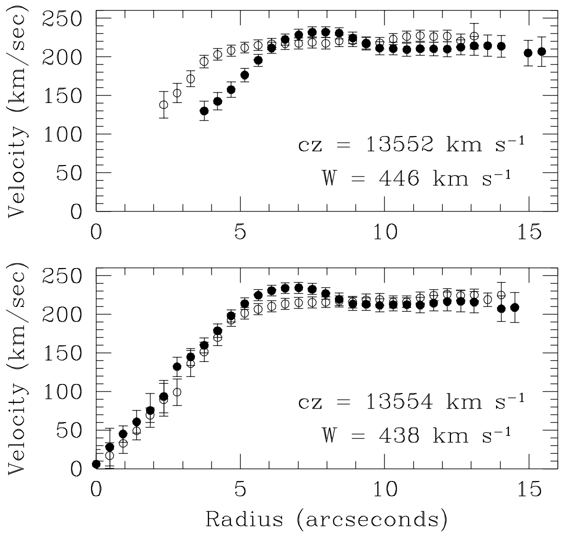

Figure 4.2 The effect of a [NII] data patch on a kinematically folded Hα rotation curve lacking data in the central regions due to absorption. The upper panel displays the Hα rotation curve for galaxy 400641 in Abell 119 without the patch, the lower panel includes the [NII] data patch. Notice the kinematical recentering changes the definition of the RC origin in the spatial direction as well as in the velocity direction.

In regions where heavy Hα absorption and emission are mixed, usually near the galactic center, we fill in the portions of the rotation curve with data from the [NII] rotation curve, if available. We do this to provide information on the shape of the inner portions of all RCs and to ensure that our method of computing velocity widths does not artificially yield incorrect values when data are missing. We apply this [NII] patch to approximately 10% of the Hα RCs; the notes on individual galaxies in Chapter 5 indicates which RCs include [NII] patches. In Figure 4.2 we display the effect a [NII] patch can have on a RC using the RC of galaxy 400641 in Abell 119 as an example. The upper panel gives the Hα RC without the [NII] patch, the lower panel includes the patch. The effect on the inferred redshift and $W_{80\%}$ (described in the ensuing section) is small, but the shape of the RC has changed significantly. This change is in part due to the kinematical recentering of the RC — the origin of the RC has also been shifted radially (by $0.94''$). If information on the central portions of an RC is lacking for all spectral lines available, we consider the peak of the galactic continuum light profile, formed by summing the data along the dispersion direction, to represent the spatial center of the galaxy (see, for example, the upper panel of Figure 4.2).

4.3 Optical Rotation Curves: Empirical Models and Simulations

Besides avoiding the spatial confusion problem encountered by single dish radio telescopes, important in observing galaxies clustered together at intermediate redshifts, optical emission line spectroscopy provides detailed mapping of the rotation curve along the chosen position angle. This mapping facilitates estimating the impact of the optical rotation curve shape (e.g. still rising at the optical radius) on the determination of the velocity width. On the other hand, advantages of using the 21 cm line include that i), velocity widths are "position angle–independent" and ii), HI typically extends farther than the optical radius; an HI velocity width is more likely to have included light near or beyond the turnover radius, the point at which the rotation curve begins to fall. Hence, in many instances, 21 cm work gives more accurate velocity widths than could be measured optically. Haynes *et al.* (1997) reports 21 cm measurements for ∼840 galaxies at redshifts of up to z ∼0.04, a data set which has a small overlap with our sample; we forego Hα and use 21 cm widths when they are available. The origin of our velocity width sample is thus of an inhomogeneous nature.

Though the sample of rotational velocity widths presented here primarily originate from optical spectroscopy – optical velocity widths outnumber widths from 21 cm work by 10 to 1 in the SCII sample – it is of utmost importance to properly cross calibrate the optical and radio measures. Besides providing internal consistency, such a calibration also allows fair comparisons between peculiar velocities derived from this sample and others that may not have relied primarily on optical velocity widths. This is an immediate concern of ours since we will use the SCI cluster peculiar velocities in concert with those found here to better characterize the local peculiar velocity field (Chapter 7). This calibration is thoroughly studied in G98b, facilitated by both computer simulations of optical RCs and 21 cm profiles, and by direct comparisons of optical and radio data. What follows both highlights and borrows heavily from that work, with the emphasis placed on understanding the nature of velocity widths via optical RCs.

4.3.1 Simulation Ingredients: Gas Distribution, Rotation Curve Shape and Disk Model

Two principal agents, besides disk inclination, determine the observed spectra of normal spirals: the rotation curve $V(r)$ and the distribution of the kinematical tracers in the galaxy. For a set of galaxies of given luminosity, variance in the rotation curve shape and in the radial distribution of emission regions results in variedly shaped spectra; since radio and optical spectral measurements sample disks differently, differences in the measured widths result. Numerical simulations can aid in the investigation of the statistical characteristics of those differences. In this section we obtain a family of functional representations to be used in simulations.

Another important reason motivates the need for reliable RC functional forms.

As will be discussed in 4.4.2, the range of disk radii sampled by observed optical RCs varies greatly from galaxy to galaxy, due to variations in the surface brightness of Hα and the sensitivity of the spectroscopic observations, which may end up playing an important role in the amplitude of the derived rotational velocities. In order to achieve an objective measure of width, we will argue that rotational velocity is best measured at a standard radius, preferably in the outer parts of the disk. This may require an extrapolation beyond the last radial distance for which a measure of the RC is available. Thus an expectation value of the RC slope in the unsampled region of the disk, obtainable from a functional representation of the RC, can be very useful.

4.3.2 Model Rotation Curves

Several algorithms have been proposed for the characterization of the RCs of spiral galaxies. With a physical basis, some invoke the combination of recognized physical components such as disk, bulge, and halo and attempt a parameterization regulated by galaxy type or luminosity. While more complex and ultimately more revealing of the global properties of galaxies, these models often do not have the analytical elasticity necessary to fit many individual RCs, unless a full–fledged combination of disk, bulge, halo, bar, and occasionally large–scale asymmetries, is adopted. Other empirical models exhibit analytical simplicity and/or fitting malleability, but generally fail to reflect the physical diversity of galactic components. Ultimately, the adoption of a particular model depends on the goals of the study.

PSS Universal Rotation Curve

Persic & Salucci (1991) have promoted the idea of a "universal rotation curve" (URC), a parameterization of the rotational characteristics of spiral galaxies. Initially, they obtained luminosity dependences for the velocity $V(r_{83})$ at the optical radius and for the slope of the RC in the outer parts of the disk. The optical radius, r_{83}, is defined as that from within which 83% of the light of a galaxy is emitted; for a pure exponential disk of scalelength $r_{\rm d}$, $r_{83} = 3.2 r_{\rm d}$. More recently, Persic, Salucci & Stel (1996; hereafter PSS) produced parametric expressions that describe the "average RC" of a galaxy of any arbitrary luminosity. They first averaged the observed RCs of many galaxies by luminosity bin, then fitted them with a parametric form and expressed the fit coefficients as functions of luminosity. The parametric form is the combination in quadrature of two components, an exponential disk and a dark matter halo:

$$V_{\rm urc}(r, L) = [V_{\rm d}^2 + V_{\rm h}^2]^{1/2} \tag{4.1}$$

where

$$V_{\rm d}^2(r, L) = V^2(r_{83})\beta \frac{1.97x^{1.22}}{(x^2 + 0.608)^{1.43}} \tag{4.2}$$

and

$$V_{\rm h}^2(r, L) = V^2(r_{83})(1 - \beta)(1 + a^2)\frac{1}{1 + (a/x)^2} \tag{4.3}$$

The variable $x = r/r_{83}$ yields the radial scaling and the parameters β and a depend on the galaxy luminosity, namely:

$$\beta = 0.72 + 0.44 \log(L/L^*) \qquad a = 1.5(L/L^*)^{0.2} \tag{4.4}$$

The disk rotation curve suggested by PSS approximates well that of an infinitely thin exponential disk within $x \sim 2$. Beyond $x = 2$, $V_{\rm d}$ is assumed to have a

Keplerian fall–off: $V_{\rm d} \propto r^{-1/2}$. In order to prevent the halo contribution to the RC to become negative at high L, a minimum value of $\beta \simeq 0.83$ needs to be forced. A scale commensurate with I band magnitudes requires $L/L* = 10^{-0.4(M-M^*)}$ with $M^* = -22$, for $H_\circ = 100$ km s^{-1} Mpc^{-1}. This scaling will yield velocity widths which at r_{83} will match those inferred from the TF template relation of G97b, $W(r_{83}) = 2V(r_{83}) = 10^{-(M+21.01)/7.68+2.5}$. Note that for a perfect exponential disk, the maximum of the disk RC occurs at approximately 2.2 scalelengths from the center, or at $r \simeq 0.69 r_{83}$.

The URCs parameterized by Equations (4.1)–(4.4) fit well most of the characteristics of *averaged* observed RCs. Such averages were obtained by PSS from the data of Mathewson *et al.* (1992): they separated approximately 900 rotation curves in eleven luminosity bins and obtained mean RCs for each bin, with the radial distance scaled by each galaxy's r_{83}. However, among galaxies of given luminosity, there is substantial variance in the RC shape, so that the URC models fail badly in reproducing the characteristics of many individual galaxies' RCs. This prompted us to explore alternative models for the RC shape, which would give us more leeway in fits to individual objects and provide a more "plastic" fit to the actual data.

Other Models

The rotational velocity of a particle in a halo density distribution of the type $\rho(r) \propto [1 + (r/r_\circ)^2]^{-2}$ is

$$V(r) = V_{\rm c}[1 - (r_\circ/r)\arctan(r/r_\circ)]^{-1/2} \qquad (4.5)$$

(van der Kruit 1990), which is similar to the model used by Courteau (1997) to fit 304 optical RCs:

$$V(r) = \frac{2V_c}{\pi}\arctan(r/r_\circ) \tag{4.6}$$

This model fits moderately well many RCs. Its main advantage is that of simplicity, depending only on the two parameters V_c and $r_\circ$; its shortcomings are encountered when observed RCs contain structure at short radii (a common flaw of most models) and, more importantly, when they are observed to fall at large radii, which the model cannot accommodate.

Rix *et al.* (1997) propose the form

$$V(r) = V_c(1+x)^\beta(1+x^{-\gamma})^{-1/\gamma} \tag{4.7}$$

where $x = r/R_\circ$. As in the previous formulations, V_c provides the velocity scale and $R_\circ$ a radial scale akin to the core radius, near which the RC turns over. The slope of the RC at small radii is approximately $V_c/R_\circ$. Increasing values of γ produce increasingly sharp turnovers and β gives a power law behavior to the RC at large radii.

Courteau (1997) uses a closely related form:

$$V(r) = V_c(1+1/x)^\beta(1+x^{-\gamma})^{-1/\gamma} \tag{4.8}$$

which has the desirable characteristic of being able to fit peaks in the RC at small radii (such as produced by bar distortions), when $\beta > 0$. The asymptotic slope of both Equations (4.6) and (4.7) for large values of the radius is however never negative, and these expressions encounter difficulties fitting RCs which fall at large radii, as they are often found among the most luminous systems.

Finally, we consider the simple combination

$$V_{\rm PE}(r) = a_1(1 - e^{-r/a_2})(1 + a_3 r) \tag{4.9}$$

where the coefficient a_1, as V_c above, regulates the overall amplitude of the RC, a_2 determines the exponential scale of the inner region and a_3 sets the slope of the slowly changing outer part. This model, which we refer to as *PolyEx*, fits well the average RCs built by PSS from the Mathewson *et al.* data (see G98b for a graphic representation of the model). The coefficients of each fit are illustrated in Figure 2 and Table 1 of G98b.

The *PolyEx* model fits equally well the average RC data as the URC model discussed in the preceding section. It also allows excellent latitude in fitting individual RCs. It fails more conspicuously in cases where the RC has a sharp peak at small radii and in "solid body" cases. It is however an economical expression, requiring only three parameters a_1, a_2 and a_3 — one fewer than expressions (4.7) and (4.8). In cases in which the observed RC is radially undersampled, one can force a fit with a fixed value of a_3, the asymptotic slope and use the resulting model to extrapolate the RC to the desired outer radius, e.g. r_{83}.

In the simulations described in the following sections, we have used to equal advantage both the URC and the *PolyEx* models. However, in deriving the widths at r_{83} from the actual data, as we discuss in Section 4.4, we used the *PolyEx* model, which proved more malleable than the URC approach.

4.3.3 Radial Distribution of Tracers

In the extraction of long–slit spectra from our simulations, we assume that the emission line intensity scales like the surface density of the gas to the 1.3 power

(Kennicutt 1989). We mostly follow the findings of Broeils & Rhee (1997) in determining the distribution of the disk HI gas; our departures from this model are discussed in G98b. In order to simulate a contribution to the gas surface density by molecular hydrogen, we add a term $Ae^{-\frac{1}{2}(\frac{r}{\sigma_2})^2}$ to the HI surface density, with $\sigma_2 = r_d$ and a varying amplitude A which changes between 0 at $M_I = -19.5$ and 4 times the HI surface density peak for $M_I = -21.5$, remaining constant at those two levels outside the $(-19.5, -21.5)$ absolute magnitude interval. The shape of the assumed distribution of the optical emission line material is not very important in our simulations, because the widths inferred from optical RCs are generally not weighted by the emission intensity. More important is the assumed extent to which the optical RC can be traced, which we allow to vary in our simulations. As we will discuss later, in observed RCs the outermost sampled radius varies generally between about $0.5r_{83}$ and $1.7r_{83}$.

4.3.4 Simulation Geometry

Given the distribution of kinematical tracers — $\sigma_{\mathrm{HI}}(r)$ for the HI gas and $\sigma_\alpha(r)$ for the optical emission regions — and the rotation curve of the disk, $V(r)$, spectral profiles can be extracted from the disk simulations, which would mimic the actual observations. Assuming an inclination i, any point on the disk is assigned a line–of–sight velocity

$$V_{||}(x,y) = V(r)\frac{x}{\sqrt{x^2+y^2}}\sin i + V_{\mathrm{turb}}, \tag{4.10}$$

where (x, y) are Cartesian coordinates on the plane of the disk and V_{turb} is a turbulent term, a random deviate of a Gaussian of 11 km s^{-1} dispersion. An "observed" HI profile is the velocity histogram of the weighted contributions of all surface elements of the disk, where the weight is given by $\sigma_{\rm HI}(r)$. An "observed" RC is obtained as follows. A slit window, of thickness $w_{\rm slit}$, is overlayed on the inclined disk; the contributions to the observed RC will be provided by the parts of the disk that fall within the window. Grid point spacing on the disk is always forced to be $w_{\rm slit}/20$. If (x', y') are Cartesian coordinates on the slit itself, with x' the coordinate along the slit major axis, the RC is extracted from the spectral profile

$$I(x', V) = \Sigma_{x'}\Sigma_{y'}\ \sigma_\alpha(r)\ \delta[V - V_{||}(x, y)] \qquad (4.11)$$

where δ is a Dirac–delta function, the sum in x' is typically over an interval centered on x' that reflects the seeing conditions [default value is $w_{\rm slit}/2$], and the sum in y' is taken across the whole width of the slit. This spectral profile is convolved with a Gaussian (in our case of dispersion 30 km s^{-1}) to simulate the spectrograph resolution. The RC value at x' is the mode of the resulting smoothed profile. We approximate that value by fitting a Gaussian to the peak of the spectrum, and selecting the value of the velocity at which the Gaussian fit peaks. When the slit is exactly aligned with the disk major axis, $x \equiv x'$.

4.4 Long–Slit Optical Spectra

The determination of velocity widths based on optical long–slit spectra, for applications with the TF relation, has received substantial impulse in recent years. Large bodies of work have been contributed by Mathewson *et al.* (1992) and Mathewson & Ford (1996), hereafter jointly referred to as MF; Vogt, Haynes & Herter (see Vogt 1995), D97, D98a, and D98b, jointly referred to as PAL; and Courteau (1997). These observational studies concentrate on the red part of the optical spectrum, made attractive by the presence of several nebular lines, most prominently Hα at 6563Å, [NII]$\lambda\lambda$6548,6584Å and [SII]$\lambda\lambda$6716,6731Å. In this section we present methods to measure rotational velocity widths from long–slit optical spectra and the corrections that need to be applied to them. These corrections account for disk inclination, cosmological broadening, disk opacity and smearing of the shape of the RC, produced by the physical width and the misalignment of the spectrograph slit with respect to the major axis of the galaxy's disk.

4.4.1 The Measurement of Rotation Curves and Their Velocity Widths

We start our discussion from the measurement of a fully calibrated spectrum, i.e. a set of spectral profiles sampled at different radial distances along the major axis of the galaxy. The spectrum at any given radial position (a slice across the spectrograph slit) is the integral emission of the gas at that radius, broadened spatially and spectrally by atmospheric seeing and pixel size, instrumental response, turbulent motions of the gas and by the fact that any transversal segment of the slit blends the emission of several different regions of the disk, that may be characterized by different lines of sight components of the rotational velocity. The latter effect increases rapidly in importance as the inclination of the disk approaches the edge–on perspective. In highly inclined systems, the expected line profile at any given radius along the slit is asymmetric, peaking near the line of sight velocity that corresponds to the on–major axis point. Operationally, it is customary to use the mode of the line profile as an indication of velocity at the given radial distance along the slit. In practice, fitting a Gaussian to the central peak of the line profile yields the desired result. Thus an observed RC is extracted from the set of spectra along the slit. Because the pixel size does, in the radial direction, generally oversample the median seeing disk size, radial averaging of the observed RC is generally carried out, most commonly via a three–point boxcar averaging, which produces minimal smoothing of the RC but increases the signal–to–noise.

Once an optical RC is available, a width can be extracted either

(i) by collapsing the RC into a velocity histogram, to which each point of the RC contributes equally, forming an integrated line profile; then an algorithm similar to the one described for the measurement of radio line profiles yields a width $W_{\rm his}$; or

(ii) by folding the RC about a photometric or kinematic center of the galaxy, and referring to the amplitude of the rotational velocity at some chosen radius, $V_{\rm rot}(r_{\rm RC})$, or twice that value.

MF report a width as "the difference between the maximum and the minimum values of the rotation curve", i.e. the difference between the extreme velocities of the histogram, which we shall refer to as $W_{\rm max}$, while their systemic velocity is the midpoint between the two; PAL measure a width, $W_{80\%}$, which is the difference between the 10% and 90% velocities of the histogram: $W_{80\%} \equiv V_{90\%} - V_{10\%}$. This method is useful since it effectively ignores small–scale velocity irregularities within an RC that may arise from streaming motions within the galactic disk, the non–uniform distribution of HII regions, or distortions associated with the spiral pattern.

As mentioned in Section 4.3.1 and discussed in 4.4.2, widths as $W_{\rm his}$ depend on the spatial coverage of the observed RC, and therefore on the sensitivity of the observations. This vulnerability can be avoided by measuring widths at some fixed radial distance $r_{\rm RC}$ from the center of the galaxy, as in method (ii) above. What is the best choice for $r_{\rm RC}$? Two values are most frequently used. Since the maximum of the rotational velocity of a pure exponential disk is expected to occur at r=2.2$r_{\rm d}$, where $r_{\rm d}$ is the scalelength of the disk light, several authors have advocated the use of scaling relations involving 2.2$r_{\rm d}$ and $V_{\rm rot}(2.2r_{\rm d})$ (e.g. Chiba & Yoshii 1995; Karachentsev 1989; Courteau 1997). An alternative choice (Persic & Salucci 1995; G97a) is that of the so–called "optical radius", r_{83}.

The measurement at $V_{\rm rot}(2.2r_{\rm d})$ has an important advantage over that at $V_{\rm rot}(r_{83})$: most observed RCs are mapped as far out as 2.2$r_{\rm d}$, while generally only about 60% are mapped as far out as r_{83}. The measurement of $V_{\rm rot}(r_{83})$ thus requires more often an extrapolation of the observed RC. The advantages of $V_{\rm rot}(r_{83})$ over $V_{\rm rot}(2.2r_{\rm d})$ are however also important. Internal extinction depends on the inclination of disks and affects the estimate of not only the total flux but also of the scalelength, isophotal and other characteristic radii, as well as the observed shape of the RC itself. Because extinction and the derivative of the RC increase with decreasing radius, measures of $V_{\rm rot}(r)$ are more resilient in the outer disk. Moreover, scalelengths are parameters of notoriously unreliable measure and significantly more dependent on inclination than a cumulative parameter such as r_{83}. Since in the vast majority of observed RCs, which require an extrapolation to obtain $V_{\rm rot}(r_{83})$, such extrapolation is usually small; in our experience the total uncertainty associated with the derivation of $V_{\rm rot}(r_{83})$ is smaller than that of using $V_{\rm rot}(2.2r_{\rm d})$.

4.4.2 Corrections

Measures of optical velocity widths require corrections for several effects, which are listed here and discussed in more detail in subsections below:

- Width measurements obtained from a velocity histogram require a correction for radial undersampling of the RC, which depends on the outermost extent and the shape of the observed RC, sometimes referred to as the *shape correction*, $\Delta_{\rm sh}$. If the observed raw width is ${}^{\circ}W_{\rm opt}$, we define ${}^{1}W_{\rm opt} = {}^{\circ}W_{\rm opt} + \Delta_{\rm sh}$. If ${}^{\circ}W_{\rm opt}$ is of the type (ii) described in the preceding section, then $\Delta_{\rm sh} = 0$. So $\Delta_{\rm sh}$ is an additive term that converts type (i) into type (ii) widths.

- The radial scale at which $V_{\rm rot}$ is measured should be corrected to face–on viewing. This is not *per se* a correction to the width, but rather a reminder that the proper radius should be used and a potential source of uncertainty associated with the radial scale correction.

- A cosmological broadening correction: ${}^{2}W_{\rm opt} = {}^{1}W_{\rm opt}/(1+z)$.

- A correction for the observed inclination of the galactic disk. ${}^{3}W_{\rm opt} = {}^{2}W_{\rm opt}/\sin i$.

- A disk opacity correction. Extinction of Hα light traveling through edge–on disks attenuates the RC amplitude and may have a significant effect on the observed width: ${}^{4}W_{\rm opt} = {}^{3}W_{\rm opt} f_{\rm op}$.

- A slit smearing and misalignment correction. The width of the spectrograph slit may not be negligible, in comparison with the galaxy image;

furthermore, it may not be perfectly aligned along the major axis of the inclined disk. These effects distort the observed RC, requiring a correction $f_{\rm slit}$, so that ${}^5W_{\rm opt} = {}^4W_{\rm opt} f_{\rm slit}$.

The corrected optical velocity width can finally be expressed as

$$W_{\rm cor} = \frac{{}^{\circ}W_{\rm opt} + \Delta_{\rm sh}}{(1+z)\sin i} f_{\rm op} f_{\rm slit}. \tag{4.12}$$

Usually, no turbulent motion correction is applied to widths derived from optical RCs. The reason is that, at any spatial location along the slit, the RC is obtained from the velocity of the peak of the line emission, and the broadening of the line due to turbulent motions and instrumental profiles only affects its width. At any rate, the turbulent broadening of optical emission lines is in general significantly smaller than the instrumental broadening. Recently, Wang *et al.* (1997) have analyzed the kinematics of giant HII regions and that of the diffuse ionized gas (DIG), which contribute to the overall Hα emission. They find the DIG to be more disturbed than HII regions, the former exhibiting dispersions of 18 to 60 km s^{-1} while that of HII regions is typically 20 km s^{-1} or less. Since the contribution of the DIG to the total Hα flux is small compared to that of HII regions, a turbulent broadening term for the Hα emission lines of 20 km s^{-1} or less seems appropriate. By comparison, the instrumental broadening is typically on the order of 30 km s^{-1} or larger.

The uncertainties introduced by the inclination correction ${}^2W_{\rm opt} \rightarrow {}^3W_{\rm opt}$ are discussed in G97a and D97 and Chapter 3. In the following subsections we discuss and quantify anew the other corrections listed above. Note that those arising from disk opacity and slit positioning and smearing preferentially act to *attenuate* $W_{\rm opt}$, due to the sampling of regions off the major axis of the galactic disk, resulting in a systematic bias in measured widths.

RC Shape Correction and Extrapolation of the RC

If the outer parts of the RC exhibit a nonzero gradient, the results of width measurements of the type (i) described above, such as in the case of $W_{\rm max}$ or $W_{80\%}$, will depend on the maximum radial distance $r_{\rm cut}$ at which the RC is measured and on the RC shape. If, for example, a RC rises monotonically with radius, the histogram–derived $W_{\rm opt}$ will increase as the RC is sampled progressively farther out. Measurements of $W_{\rm opt}$ of type (i) as described above, where RCs are always measured to the same radius $r_{\rm RC}$, yield more objective estimates of widths, so that the shape correction $\Delta_{\rm sh}$ is a term that converts widths from a type (i) to a type (ii).

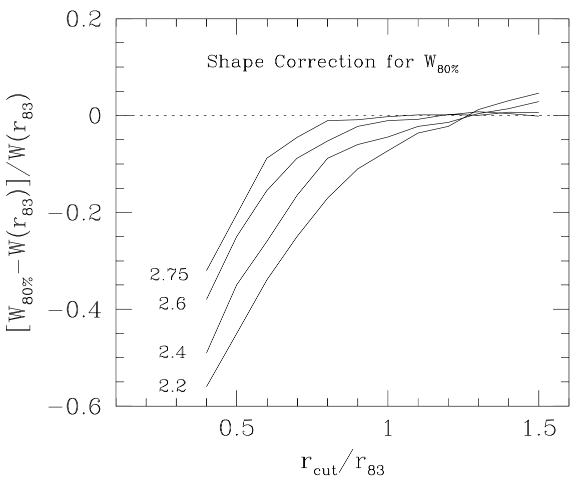

Figure 4.3 Graphic display of the fractional difference between the measured value of $W_{80\%}$ and that of the velocity width measured at $W(r_{83})$, plotted against the ratio between the outer radial cutoff of the observed RC and the optical radius. The results are obtained from simulations as described in the text. This display can be used to estimate the shape correction $\Delta_{\rm sh}$ applicable to the velocity width $W_{80\%}$. The effect is separately plotted for galaxies characterized by different values of $\log W$, as indicated.

In Section 4.4.1, it was argued that a choice of $r_{\rm RC}$ should be favored where that radius falls sufficiently far out in the disk to avoid the effects of extinction and regions where the RC is unstable or where its derivative is large. That is one of the reasons we have adopted $r_{\rm RC} = r_{83}$. In Figure 4.3, a graphic display is shown of the fractional difference between $W_{80\%}$ and $W(r_{83})$, as estimated from simulations, separately for galaxies of different velocity width, as indicated in the graph. That fractional difference is plotted against the ratio between $r_{\rm cut}$ and r_{83}. The display can also be used to estimate $\Delta_{\rm sh}$ for $W_{80\%}$.

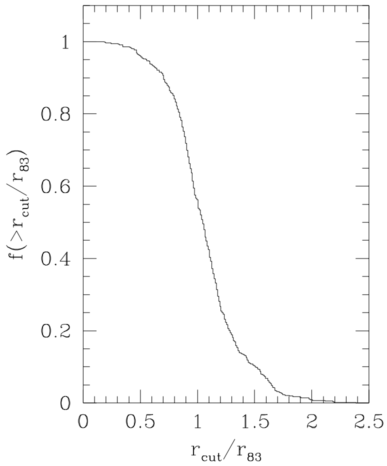

Figure 4.4 Fraction of optical RCs reaching a maximum radial distance equal to or larger than $r_{\rm cut}/r_{83}$, from the PAL and MF data bases. About 60% of RCs extend at least as far out as r_{83}.

If the value of the width at some radius $r_{\rm RC}$ is adopted as standard, and the RC extends to $r_{\rm cut}{>}r_{\rm RC}$, the value $W(r_{\rm RC})$ can be inferred by simple interpolation of the observed RC. If, on the other hand, $r_{\rm cut}{<}r_{\rm RC}$, an extrapolation is necessary. Optical RCs extend to radial distances $r_{\rm cut}$ which vary greatly from object to object. On the average, the RCs of MF and PAL extend to $r_{\rm cut}{=}\ 1.08r_{83}$; however, about 40% of estimates of $W(r_{83})$ require an extrapolation of the observed RC beyond the last sampled radius. This is illustrated in Figure 4.4, which gives the frequency with which an observed RC extends to a radius larger than r/r_{83}, for the joint data set of PAL and MF samples (see Figure 19 of G98b for the difference between the two data sets in this respect). The extrapolation of the RC requires fitting an expected behavior in the unsampled regions, for example by using one of the forms discussed in Section 4.3.2. The URC forms advocated by PSS, and described in Section 4.3.2 fit well the average RC, but individual RCs are often widely variant from the average forms, which cannot be fit to advantage. Other forms have limitations, such as the inability to fit outer RCs that fall with radius, or inner region peaks such as produced by bars. We find that the most malleable model is the *Polyex* described by Equation (4.9). In using it to obtain values of $V_{\rm rot}(r_{83})$, our practice is the following: if $r_{\rm cut}$>0.75 r_{83}, the form (4.9) is fit with no constraints as to any of the three parameters a_1, a_2 and a_3. The value $V_{\rm rot}(r_{83})$ and its uncertainty are obtained from the fit and its errors, where an important role is played by the uncertainty on the outer slope a_3. If $r_{\rm cut}\leq$ 0.75 r_{83}, the value of the outer slope a_3 is constrained to match the expected value for a galaxy of the given luminosity, as shown in Figure 2 and Table 1 of G98b, and only a_1 and a_2 are solved for in the fit. The error on $V_{\rm rot}(r_{83})$ is derived from the estimated uncertainties on a_1 and a_2 and a relative uncertainty on a_3 assumed to be $0.6(1-r_{\rm cut}/r_{83})$. For $r_{\rm cut}\lesssim$ $0.5 r_{83}$, the extrapolation generally becomes too uncertain for most practical purposes. This occurs fortunately for a very small fraction of the data.

Scaling $r_{\rm RC}$ to face–on viewing

When width measurements of type (ii) are made, the definition of the radial distance $r_{\rm RC}$ at which they are to be made can be ambiguous. For example, if $r_{\rm RC}$ is a photometric quantity, such as an isophotal radius or a multiple of the scalelength, its location on the disk will vary with the inclination of the galaxy to the line of sight. As a result, $W(r_{\rm RC})$ will in general depend on inclination in a more complex form than purely sinusoidal. The deviation from a sinusoidal dependence will be regulated by (a) the manner in which the metric radius associated with $r_{\rm RC}$ changes with inclination and (b) the derivative of the RC near $r_{\rm RC}$. When $r_{\rm RC}$ changes with inclination, it would thus be necessary to standardize the approach by using the radius at a fixed inclination, such as the face–on case $r^\circ_{\rm RC}$. For example, the measured scalelength $r_{\rm d}$ of a given galaxy varies by about 50% purely as the disk inclination varies from intermediate to high values (see e.g. G94, Figure 12), and the conversion $r_{\rm d} \rightarrow r^\circ_{\rm d}$ is quite uncertain. This makes the adoption of $W(r_{\rm RC})$ as a standard width with $r_{\rm RC}$ as a multiple of the scalelength, e.g. $2.2 r_{\rm d}{}^\circ$, ill–advised, and the adoption of the corresponding $W(r^\circ_{\rm RC})$ uncertain. If for $r_{\rm RC}$ one adopts an isophotal quantity, it is advisable to use an isophote in the very outer disk, where one may safely assume nearly total transparency and the conversion of $r_{\rm RC}$ to a face–on value is straightforward. If the width is measured at r_{83}, the change of this radius with inclination is very small, as r_{83} is a *cumulative light* radius, thus its adoption as a standard appears safer than other choices.

The Effect of Disk Opacity on W

Goad & Roberts (1981) noted that the observed RC for an opaque, edge–on spiral galaxy would suggest solid body rotation, independently of the shape of the true ("major axis") RC. Only the outermost parts of the disk (i.e. $r \approx r_{83}$) would be visible and sampled in this case and the factor $x/\sqrt{x^2+y^2}$ in Equation (4.10) reduces to x/r_{83}, hence the linear tapering of the RC. Since the outer parts of galactic disks appear to be transparent (Bosma *et al.* 1992; Prada *et al.* 1994; G94), velocities at large radii, such as r_{83}, will in general be recoverable from observed RCs, given that the Hα emission extends that far. The distortion of the RC due to opacity effects will be most dramatic in the inner parts of nearly edge–on systems.

We characterize the dust extinction coefficient in a galaxy disk via $\kappa(x,y,z) \equiv \kappa(r,z) = \kappa(0,0)e^{-r/d_r}e^{-|z|/d_z}$, with d_r and d_z being the dust scalelength and scaleheight. Then the central, face–on disk optical depth is

$$\tau^{\circ}(0) = \int_{-\infty}^{\infty} \kappa(0,z)dz = 2\kappa(0,0)d_z. \tag{4.13}$$

If the galaxy is edge–on, a two–dimensional model can provide an indication of the highest potential severity of the effect in the measurement of widths. Within the geometrical frame described in Section 4.3.4, each grid point of coordinates $(x, y, z = 0)$ in the plane of the disk is seen through a dust layer of optical depth

$$\tau(x,y,z=0) = \int_{-\infty}^{y} \kappa(x,y',0)dy' = \kappa(0,0,0)\int_{-\infty}^{y} e^{-\sqrt{x^2+y'^2}/d_r}dy'. \tag{4.14}$$

Thus, the contribution to the RC of a volume element centered on that point will be attenuated in the measure $e^{-\tau}$. In our calculations we assume $d_z = 0.06r_{\rm d}$

and d_r=(4/3)r_d, following recent determinations of Xilouris *et al.* (1997a,b) for UGC24048 and NGC891.

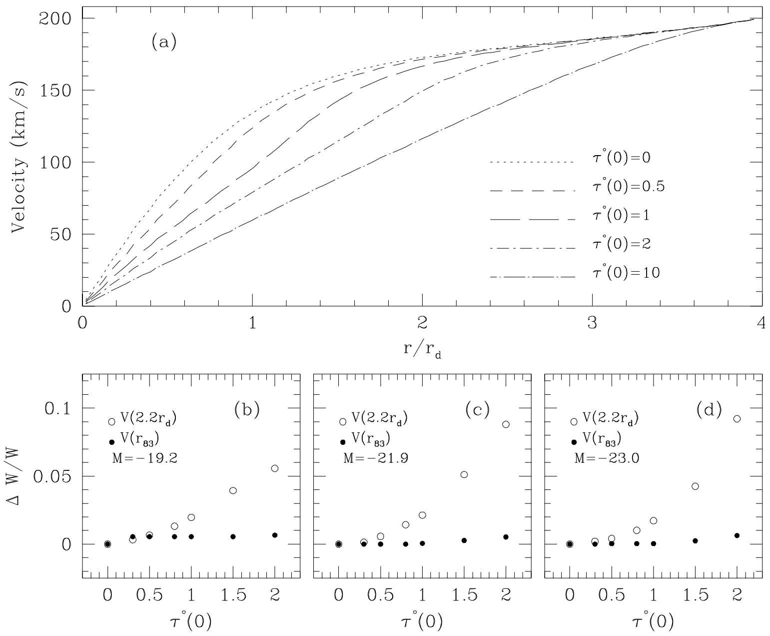

Figure 4.5 The RCs of an edge–on galaxy, with a disk characterized by different opacity levels, are shown in panel (a). Curves correspond to different values of the disk central optical depth near the wavelength of the RC tracer line. In panels (b) through (d), the fractional change in the measured width at two different radii is shown, as a function of $\tau°(0)$, for edge–on galaxies of three different absolute magnitude; the radii correspond to $r_{2.2} = 2.2r_d$, and r_{83}, the optical radius.

Figure 4.5a shows a simulation of the effect of disk opacity on the RC. The upper line represents the RC unaffected by opacity, for a galaxy of intermediate luminosity. The lower tracings correspond to different choices of the disk optical depth, parameterized by values of $\tau°(0)$ of 0.5, 1, 2 and 10 respectively. The results of Xilouris *et al.* (1997a,b) for two edge–on galaxies suggest values of $\tau°(0)$ of between 0.5 and 1.0, which would make the disks of those systems very nearly transparent if seen face–on. We note that even for relatively low opacities, the perturbation of the RC shape can be quite substantial, especially in the inner parts. At radii of the order of $3r_{\rm d}$, however, the effect of opacity is quite reduced, even for the extreme geometry of our example. We reiterate the fact that Figure 4.5a represents the worst case scenario of an edge–on system, conforming with the opacity model of Equation (4.14). Bosma *et al.* (1992) have performed a more thorough study of the effects of opacity on optical rotation curves and they similarly find negligibly changed asymptotic velocities for a larger range of scenarios, except for $i = 90°$, $\tau°(0) \gtrsim 2$. However, if the velocity width is measured at a relatively small radius $r_{\rm RC}$, it may substantially underestimate the true width for edge–on systems. In Figure 4.5, panels (b) through (d) for three different absolute magnitudes, we display the alteration in the measured rotational velocities at $2.2r_{\rm d}$ and at r_{83}, produced by extinction as parameterized by the central opacity of the face–on disk. Even moderate opacities on the order of $\tau°(0) \sim 1.5$ may lead to significant underestimates of $W(2.2r_{\rm d})$, while $W(r_{83})$ is nearly unaffected. At lower inclinations, the amplitude of the effect depends strongly on the relative angular sizes of the galaxy disk and the projected width of the spectrograph slit, as discussed in the next section, and rapidly ceases to be a serious concern a few degrees off the edge–on perspective.

Thus, for reasonable expectations of disk opacity, we conclude that the effects on velocity widths are in general quite mild, *provided that the RC is measured in the outer parts of the disk.* Widths of highly inclined systems, measured as far in as $2.2r_{\rm d}$, should be taken with caution. We believe that even $W(r_{83})$ may be affected, albeit at a smaller level, perhaps on the order of a couple of percent, especially for large, very inclined ($i > 88°$) disks. However, given the currently large degree of uncertainty in the characterization of the amount of extinction in the inner parts of disks, we choose not to apply an extinction correction for $W(r_{83})$, and in processing our data we use $f_{\rm op} = 1$. We also caution that if the RC of an edge–on galaxy is sampled to an outer radius $r_{\rm cut}$ significantly smaller than r_{83}, the depression produced by opacity on the observed part of the RC will likely affect heavily the measure of any width.

The Effect of Slit Smearing

It has been shown that the effects of beam smearing act to systematically decrement rotational velocities obtained from HI synthesis maps, especially near the knee of the rotation curve (Rubin *et al.* 1989). The angular resolution of HI synthesis maps of spiral disks generally varies between $10''$ and $1'$. Each resolution element along the major axis contains emission not only from gas along the major axis proper, along which the maximum rotational speed should be observed (bar a variety of possible asymmetries), but also from regions off the major axis. In a position–velocity map along the major axis, this results in a RC which appears increasingly smeared as the disks are more inclined and as they are more poorly resolved across the major axis, by the telescope beam. The smearing is biased low in velocity, because the line–of–sight components of rotational velocities of off–axis regions are generally smaller than those of points along the major axis adjacent to them. It is then generally assumed that the high velocity envelope of such a position–velocity map yields a fair estimate of the true RC (see Figure 2, Bosma *et al.* 1992).

In long–slit spectroscopy a similar effect can be seen — the non–zero width of the slit allows sampling of regions slightly off the major axis, smearing and biasing low the extracted RC. Because of the relatively higher angular resolution of those observations, the effect is usually ignored. However, when the width of the slit cannot be neglected in comparison with the typical minor axis size of the observed disks, the effects of smearing need to be taken into account.

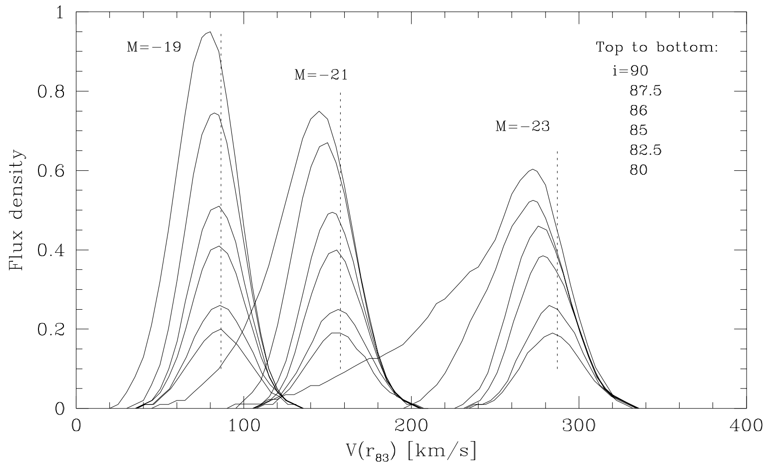

Figure 4.6 Simulated spectral profiles at r_{83}, obtained for a variety of disk inclinations and RC shapes (as parameterized by the absolute magnitude M), as indicated. Simulations were obtained for a slit width of $w_{\rm slit}$=0.2$r_{\rm d}$, and an instrumental response of 30 km s^{-1} was assumed. The Hα distribution was assumed to extend well beyond r_{83}.

Figure 4.6 illustrates the effect we refer to as "slit smearing." Using the model described in Section 4.3.1, we have computed spectral profiles as would be measured at the radial distance r_{83}, for a variety of disk inclinations and RC shapes (identified by absolute magnitude, cf. Figure 1, G98b). The simulated slit width in Figure 4.6 is $w_{\rm slit}$=0.2$r_{\rm d}$ and the instrumental response is assumed to be Gaussian with a sigma of 30 km s^{-1}. The Hα disk emissivity is allowed to extend well beyond r_{83}. The "measured" line profile at each inclination is scaled in velocity by the factor $1/\sin i$, so that the vertical dotted lines identify the values of the velocity corresponding to $V_{\rm rot}(r_{83})$ in the input model. We note two important effects: (1) at high inclinations, especially for brighter galaxies, spectral line profiles become asymmetric; (2) the peak of the profile shifts to progressively lower velocities as the inclination increases. The extension of the line profile wings to velocities larger than the input value $V_{\rm rot}(r_{83})$ is explained mainly as due to the spectral response of the instrument; the extension to lower velocities and the accompanying asymmetry of the profile is produced by the fact that regions other than those along the major axis of the disk are sampled by the slit. In the extreme case of $i = 90°$, even a very thin slit samples the whole disk, and the spectral smearing becomes independent on slit size.

In real observations, much of the spectral asymmetry exhibited by Figure 4.6 is hidden by the limited signal–to–noise ratio of the data; the broad wings are confused by noise and, to the first order, spectral shapes usually appear Gaussian. Fitting the spectral profiles with Gaussians thus generally recovers their mode.

Moreover, in practice the Hα disk emissivity appears generally truncated at some radius $r_{\rm cut}$. If the RC is measured at some radius $r_{\rm RC}{\simeq}r_{\rm cut}$, the value $V_{\rm rot}(r_{\rm RC})$ is obviously little affected by slit–smearing, as there is no off–major axis emission in the slit at that radial location. As $r_{\rm cut}$ increases well beyond $r_{\rm RC}$, the spectral profile shifts to progressively lower velocities. Slit smearing is thus also a function of $r_{\rm RC}/r_{\rm cut}$.

In general, the velocity offset, i.e. the shift in the mode of the spectral profile, depends on several parameters: the disk inclination and the RC shape (parameterized by M), as appears obvious in Figure 4.6, on the slit width, on the manner in (or the radial distance at) which the width is measured and on the radial extent of the emission regions in the disk. Finding a reliable correction recipe for observed widths appears at first to be a complicated task. Fortunately, some of

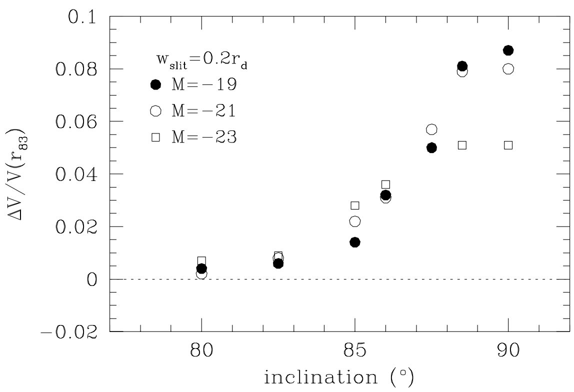

Figure 4.7 Relative change in the velocity width W(r_{83}) versus disk inclination, plotted for galaxies of different absolute magnitude M, for a fixed value of the slit size of $w_{\rm slit}$=0.2$r_{\rm d}$ and Hα distribution extending well beyond r_{83}.

the dependences appear to be easily separable. For example, simulations show that the *fractional* change in the width, i.e. $\Delta W/W$ is, to the first order, independent on RC shape. In Figure 4.7 we show the change $\Delta W/W$ for galaxies of different M, plotted versus disk inclination, for a fixed value of the ratio $w_{\rm slit}/r_{\rm d}$ and for $r_{\rm RC}$=r_{83}: a single relationship applies to the effect, except for the very brightest M and the highest inclinations, for which the effect saturates near $\Delta W/W \simeq 0.05$. Simulations show that the same disk inclination dependence is applicable to measures of $W(r_{83})$ as well as to $W_{80\%}$ and $W_{\rm max}$. The effect is ampler if the width is measured farther into the disk, e.g. for $W(2.2r_{\rm d})$: in this case the same trend as shown in Figure 4.7 applies, but with an amplitude which is larger by one–half.

Next we explore the dependence of slit smearing on slit size, parameterized by the ratio $w_{\rm slit}/r_{\rm d}$. For a given RC shape ($M = -21$), the effect of slit smearing is illustrated in Figure 4.8 for four different slit sizes and, again, for $r_{\rm RC}$=r_{83}. Superimposed on the simulated measurements are smooth lines, which represent a parameterization of the effect, which we discuss below. First, we note saturation

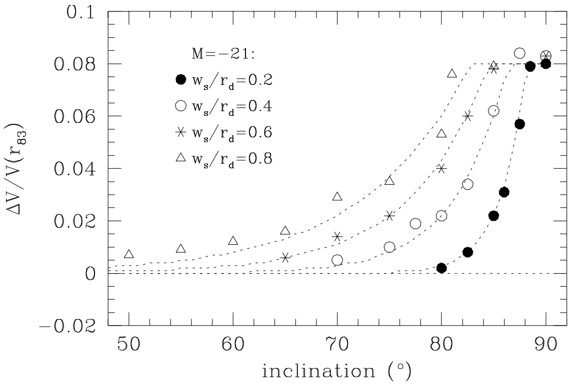

Figure 4.8 Dependence of slit smearing on slit size, parameterized by the ratio $w_{\rm slit}/r_{\rm d}$. The relative change in the velocity width $W(r_{83})$ is plotted versus disk inclination for 3 different slit sizes, as indicated, for a given RC shape (corresponding to a galaxy of $M = -21$). The smooth lines represent the empirical parameterization of the effect given by Equation (4.17).

of the effect for high inclination: that is due to the fact that, once the majority of the disk falls within the slit, further approach to the edge–on perspective produces no additional smearing. The inclination angle at which saturation occurs, $i_{\rm max}$, is expected at roughly $i_{\rm max} = \cos^{-1}(w_{\rm slit}/2r_{\rm RC})$, where $r_{\rm RC}$ is the radius at which the RC is being measured. For $r_{\rm RC}$=r_{83}, $i_{\rm max} \simeq \cos^{-1}$ $(w_{\rm slit}/6.4r_{\rm d})$, which yields $i_{\rm max} \simeq 88°,\ 86.4°, 84.6°,\ 82.8°$ for values of $w_{\rm slit}/r_{\rm d}$ of 0.2, 0.4, 0.6 and 0.8 respectively. These are in general agreement with the angles at which saturation appears in simulations in Figure 4.8.

The dotted lines in Figure 4.8 correspond to

$$\begin{aligned} \Delta W/W &= c_1\ e^{-(i_{\rm max}-i)/i_\circ} && \text{for}\ \ i < i_{\rm max} \\ &= c_1 && \text{for}\ \ i \geq i_{\rm max} \end{aligned} \tag{4.15}$$

where $i_\circ = 12.5 w_{\rm slit}/r_{\rm d}$. This empirical relation appears to fit moderately well all simulated data. For W=$W(r_{83})$ and W=$W_{80\%}$, c_1=0.08, while for W=$W(2.2r_{\rm d})$, c_1=0.10. For galaxies brighter than $M = -21.5$, $\Delta W/W$ saturates near 0.05, as already noted in Figure 4.7.

The dependence of the slit smearing effect on the extent of the Hα emission is relatively straightforward. Most of the smearing of $W(r_{\rm RC})$ is produced by the capture within the slit of radiation produced at radii immediately beyond $r_{\rm RC}$. If the cutoff radius of the Hα emission $r_{\rm cut}$ extends a few percent beyond $r_{\rm RC}$, the full slit smearing effect described by Equation (4.17) is seen. If $r_{\rm cut}$ falls short of $r_{\rm RC}$, the value $W(r_{\rm RC})$ is extrapolated from inner points, the velocities of most of which are affected by slit smearing; the extrapolated value should then also be corrected. In the case that the RC sampling just reaches $r_{\rm RC}$, the observed $W(r_{\rm RC})$ is minimally affected by slit smearing, but the observed velocities inner to $r_{\rm RC}$ are slit smeared. If the value of the rotational velocity at $r_{\rm RC}$ is inferred from a model fit to the RC or by interpolation, the result will thus be affected by slit smearing. It is thus simpler and more appropriate to correct for the full effect in all cases, independently on $r_{\rm cut}/r_{\rm RC}$.

The effect of slit smearing is compounded by errors in the alignment between the spectrograph slit and the major axis of the galaxy, which we consider next. As we will see, it is convenient to parameterize jointly the two effects.

The Effect of Slit Misalignment

The extraction of the rotational velocity width from an observed RC assumes that the velocity sampling has been performed along the major axis of the disk, and that motions are planar and circular. The actual spectrograph slit positioning may differ, though, from that of the disk major axis due to errors in the estimate of the center of light position and of the position angle PA. Errors in the centering of the slit on the light centroid are rare, as the latter is easily gauged by visual inspection at the telescope, usually within a fraction of the seeing radius and of the slit width. Errors in the estimate of the position angle are far more common, and they can be large for objects of low inclination or with wealth of structural features, such as bars or bright, open spiral arms. It is thus important to estimate the impact of the potential errors in the positioning of the slit. In the simulations described in this section, we assume that the slit is well centered but the position angle may be off from the true major axis of the galaxy by an amount $\epsilon_{\rm pa}$.

Consider the following simple geometric argument. If the slit is very narrow and the RC changes slowly in the outer portions of the disk, an error $\epsilon_{\rm pa}$ in the alignment of the slit will produce an error in the measured velocity at large radii of ΔV. It can be readily shown that the relative error on the rotational velocity is

$$\frac{\Delta V_{\rm rot}}{V_{\rm rot}} \simeq 1 - \frac{1}{\sqrt{1+\eta^2}}, \qquad \text{where} \qquad \eta = \frac{\tan \epsilon_{\rm pa}}{\cos i} \tag{4.16}$$

for a disk at inclination i. For a fixed $\epsilon_{\rm pa}$, as the inclination of the disk increases or the width of the slit $w_{\rm slit}$ becomes commensurable with the projected disk scales, parts of the major axis of the galaxy are increasingly contained within the slit, so that the observed departure from the true rotational velocity becomes smaller than predicted by Equation (4.16). In other words, *slit smearing partly compensates for the effect of slit misalignment, and it will do so increasingly in small angular size and highly inclined galaxies.* It is thus practical to analyze the effect of slit misalignment jointly with that of slit smearing.

We simulate the effect of slit misalignment and smearing by using the same geometric construct described in the previous two sections. We explore the rather vast parameter space of RC shapes (parameterized by M), slit sizes, disk inclina-

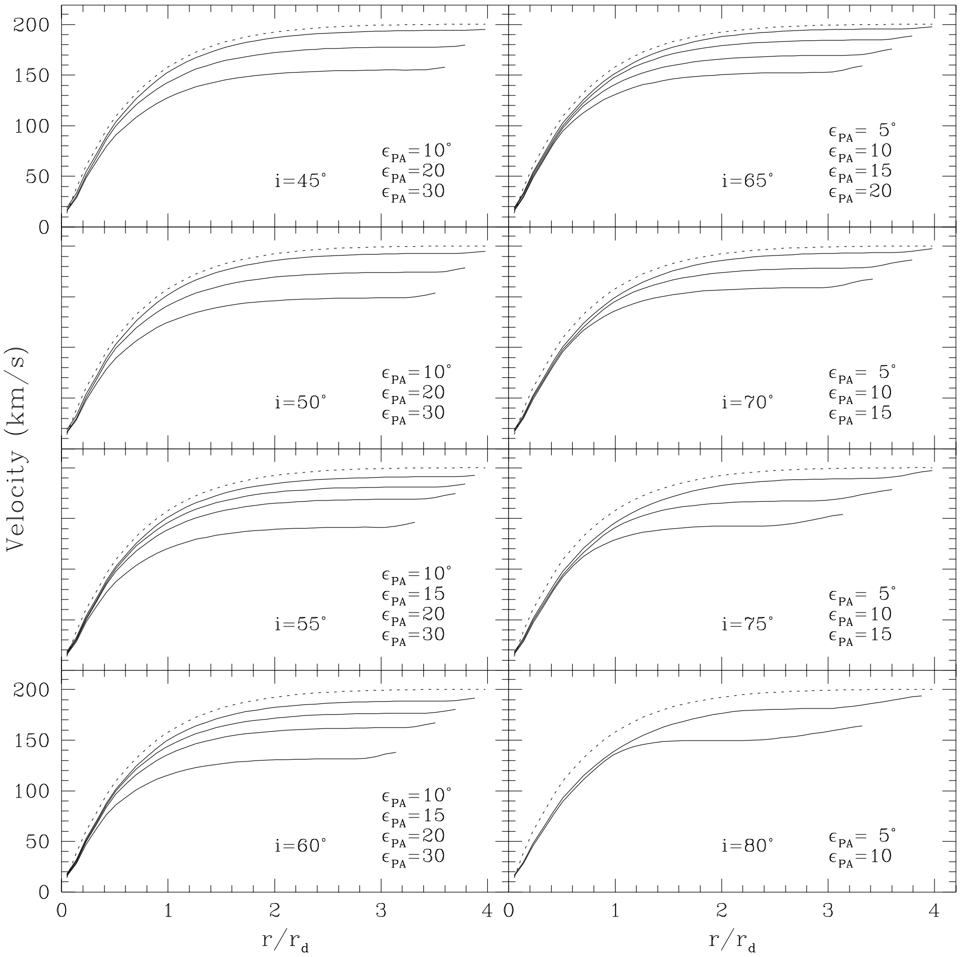

Figure 4.9 A collection of observed rotation curves for a variety of slit misalignments and disk inclinations. The curves are deprojected for inclination. The model rotation curve is also displayed as a dashed line.

tions, position angle errors, width measuring convention, extent of the RC tracer material. Examples of the simulations are shown in Figure 4.9 and Figure 4.10 for a galaxy of $M = -21.8$ (for which the RC is close to asymptotically flat). Figure 4.9 gives "observed" (but deprojected for inclination) RCs for a variety of inclinations and slit misalignments for a galaxy with $w_{\rm slit}/r_{\rm d}$ of 0.4. The shape and amplitude of the "true" rotation curve is that of Equation 4.9 and is indicated by a dashed line. Figure 4.10 displays the fractional error in the velocity

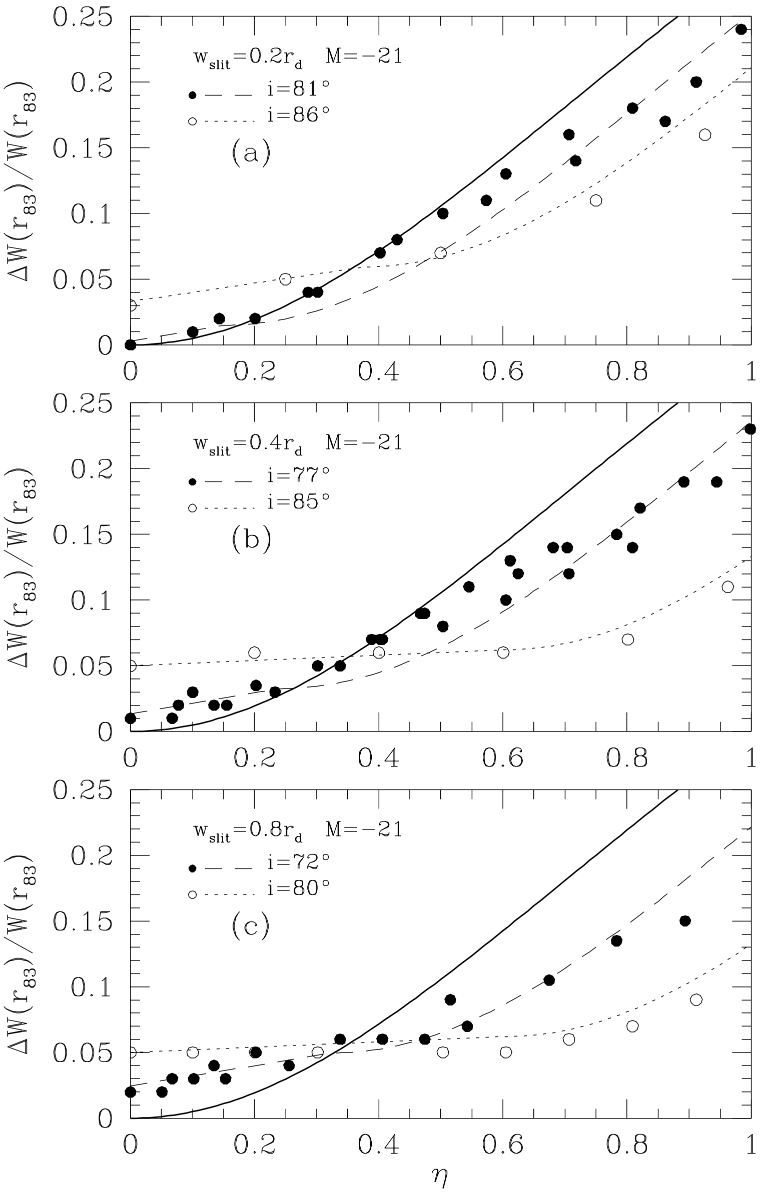

Figure 4.10 Fractional error in the measurement of the width at r_{83}, due to the combination of slit smearing and misalignment. The three panels show examples of the effect for galaxies of $M = -21.8$ and three different slit widths, expressed in units of the scalelength $r_{\rm d}$, respectively in panels (a), (b) and (c). In each panel, the case for two different disk inclinations is shown. The dashed and dotted lines superimposed on the simulation data points identify the error modeling relations (4.17–4.21), while the solid line identifies Equation (4.16).

measurement at $r_{\rm RC}$=r_{83} resulting for a galaxy observed with a slit such that $w_{\rm slit}/r_{\rm d} = 0.2$, 0.4 and 0.8, respectively for panels (a), (b) and (c). The RC tracer material is allowed to extend well beyond r_{83}. The velocity errors expected for several disk inclinations are shown; the smooth solid curve represents Equation (4.16). We can note the following:

- The combined effect of slit smearing and misalignment is always directed in the sense of underestimating the true velocity width.

- As expected, for most values of the PA error, Equation (4.16) represents an upper limit to the velocity measurement error, which is matched in the case of galaxies at low inclination; as the inclination increases, slit smearing attenuates the effect of slit misalignment.

- For small values of η, i.e. small PA errors, slit smearing dominates and leads to velocity errors in excess of that predicted by Equation (4.16).

- At high inclinations, the width error remains constant at a minimum value until η reaches a threshold $\eta_{\rm th}$. This reflects the fact that, for a given disk inclination, the major axis of the galaxy is fully contained within the slit up to the radius $r_{\rm RC}$ at which the RC is being measured, as long as $\eta \lesssim 0.5$ $(w_{\rm slit}/r_{\rm RC})/\cos i$.

- For low values of $\eta < \eta_{\rm th}$ and not extreme values of the disk inclination, the width error increases with η slowly and in a roughly linear way, reflecting the fact that, although $r_{\rm RC}$ on the major axis is still inside the slit, the velocity distribution about $V(r_{\rm RC})$ within the slit grows progressively more asymmetric.

We also note that differences in behavior depending on M (i.e. the RC shape) constitute a second order effect, so that the parameterization of the combined slit smearing/misalignment can be expressed in a M–independent form.

Combined Slit Smearing and Misalignment Correction

Our correction for the combined slit smearing/misalignment effects, as it applies to $W(r_{83})$, is:

$$\Delta W/W = S_{\rm smearing} + S_{\rm pa} \tag{4.17}$$

where the slit correction factor $f_{\rm slit} = 1 + \Delta W/W$. The slit smearing term, according to findings in Section 4.4.2, is

$$\begin{aligned} S_{\rm smearing} &= 0.08\ e^{-(i_{\rm max}-i)/i_\circ} && \text{for} \quad i < i_{\rm max} \\ &= 0.08\ (0.05 \ \text{ for } \ M < -21.5) && \text{for} \quad i \geq i_{\rm max} \end{aligned} \tag{4.18}$$

$$\text{with} \qquad i_{\rm max} = \cos^{-1}(w_{\rm slit}/6.4 r_{\rm d}) \qquad \text{and} \qquad i_\circ = 12.5 w_{\rm slit}/r_{\rm d}$$

where $i_\circ$ is in degrees, while the slit misalignment term is

$$\begin{aligned} S_{\rm pa} &= c_2(i)\ \eta && \text{for} \quad \eta < \eta_{\rm th} \\ &= 1 - \frac{1}{\sqrt{1+(\eta-\eta_{\rm th})^2}} + c_2(i)\eta_{\rm th} && \text{for} \quad \eta \geq \eta_{\rm th} \end{aligned} \tag{4.19}$$

with $\eta = \tan\epsilon_{\rm pa}/\cos i$. The threshold value of η is

$$\eta_{\rm th} = 0.42\ \frac{(w_{\rm slit}/r_{\rm RC})}{\cos i} \tag{4.20}$$

and the slope $c_2(i)$ of the linear part of the correction for low values of η changes between a maximum value at low inclination and zero for high inclinations. We find it is best expressed by a soft step function, of the kind:

$$c_2(i) = \frac{0.08}{e^{2.5-5(i_{\rm max}-i)/i_\circ} + 1} \tag{4.21}$$

Note that the expressions for η and $\eta_{\rm th}$ diverge for $i \to 90°$. Because at high inclinations the correction depends on the difference $(\eta - \eta_{\rm th})$, divergence does not become a problem except for values of i very close to 90°. In the computation of the correction, for $i > 89°$, we use $i = 89°$.

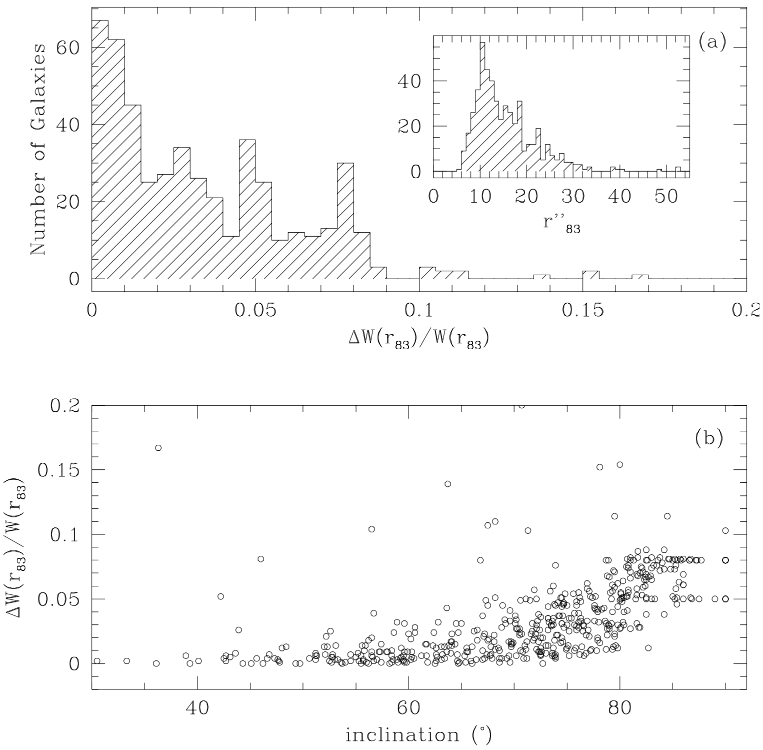

Figure 4.11 Distribution of errors $\Delta W(r_{83})/W(r_{83})$, on the basis of the galaxies' angular sizes, disk inclinations, scalelengths, width of the slit used during spectroscopy, and the misalignment of the slit with respect to the PA of disk major axes. The median optical diameter of these galaxies is 27″ in the I band, as shown in the small histogram inset in panel (a), and the spectrograph slit was 2″. In panel (a), the distribution of errors is plotted in the form of a histogram, while in panel (b) the errors are plotted versus the disk inclination.

In Figure 4.10 the effects of slit smearing and misalignment are shown for two different disk inclinations, one close to $i_{\rm max}$ (unfilled symbols) and one intermediate (filled symbols) between that value and an inclination for which the slit width becomes immaterial. The dashed and dotted lines represent the empirical relation of Equation (21). The solid curve represents the pure case of slit misalignment, Equation (4.16), for a very thin slit and a flat RC. The data points have been obtained from simulations as described in Section 4.3.1. The parameterization of Equations (4.17–4.21) fits reasonably well the data, with some systematic departures at intermediate values of η: we have chosen a parameterization that preferentially *underestimates* the necessary correction, albeit the discrepancy generally is less than 2%.

We conclude this section with a plot that illustrates the amplitude of the slit smearing/misalignment effect (i.e. $f_{\rm slit}$-1). In Figure 4.11, we show the effect for the SCII sample. The median major angular diameter of these objects is $27''$ in the I band, as shown in the small histogram inset in panel 4.11a. Errors on $\Delta W(r_{83})/W(r_{83})$ are computed from the photometric parameters and the actual misalignment of the slit with respect to the PA of the major axis, (the spectroscopy utilized a $2''$ slit width). In practice, since photometric and spectroscopic data are usually taken in parallel, good quality photometry may not be available at the time of spectroscopic observations, which may then be carried out using cataloged PA values of inferior quality. For low inclination objects, PA errors are expected to be large and thus large slit misalignment corrections are necessary. For high inclination objects, when PA errors are smaller but the minor axis size becomes comparable with the slit width, slit smearing takes place. Note that a significant fraction of the sample will need corrections of amplitude $\sim$5%. We advocate a conservative application of the slit correction by suggesting a maximum of $f_{\rm slit} = 1.08$.

The Impact of Slit Effects on Astrophysical Inferences

First consider the case of galaxies of relatively large angular size, i.e. with diameters of $1'$ or larger. PA errors are typically small if the inclination is high — e.g. if $\epsilon_{\rm pa} \simeq 2°$ and $i \sim 85°$, then $\eta \lesssim 0.4$ — but they can be large if the inclination approaches the face–on perspective: e.g. if $i \simeq 45°$, then the PA error can exceed 10°; for $\epsilon_{\rm pa} \simeq 15°$ one obtains $\eta \simeq 0.4$. Thus width corrections on the order of 5% for slit misalignment should not be considered extraordinary. In these cases, however, the determination of the inclination angle is also uncertain and likely to introduce an even larger error on the corrected width than that associated with slit misalignment. Unlike the former, however, slit misalignment is a one–way error, always forcing a systematic underestimate of width. For very high inclinations, the angular size of the minor axis can become comparable with the slit width, thus slit smearing becomes important and corrections of several percent may apply even for galaxies of large angular size. In the study of the large–scale peculiar velocity fields, if galaxies with optical and radio widths are well mixed in their sky distribution, slit effects should be relatively inconsequential. If however optical and radio data are segregated, preferentially covering different parts of the sky, a small bias may be introduced in the peculiar velocity field.

For smaller galaxies, errors due to slit effects can be significantly more conspicuous. This is a particularly important concern in the case of high redshift objects. The location of high z objects in the TF diagram with respect to a template relation — usually obtained from the study of low z objects — is often used as an indication of evolution of the galaxy population. Because slit effects systematically decrease the measured values with respect to the true ones, they will mimic evolutionary effects on the mass–to–light ratio. For example, for a galaxy of angular size of 15″ or less and intermediate inclination, PA errors leading to values of $\eta = \tan(\epsilon_{\rm pa})/\cos i > 0.6$ and $\delta W/W \gtrsim 0.15$ would be likely. For a TF relation slope of $\simeq 8$, these would result in an apparent, but spurious, "brightening" of about half a magnitude, with respect to low redshift galaxies of comparable, measured width.

4.5 Data Comparison

Direct spectroscopic data comparison between multiple data sets was carried out in G98b. The data sets are (a) the MF sample of optical and HI spectroscopic data, obtained at the Siding Spring 2.3 m and Parkes telescopes; (b) an HI sample of late spiral galaxies (Sc; see Haynes *et al.* 1997), obtained at the Arecibo, NRAO-Green Bank and Nançay observatories, and (c) PAL, our sample of optical rotation curve data obtained at the Palomar Observatory 5m Hale and Cerro Tololo 4m Blanco telescopes. Approximately 1/3 of PAL is the set of rotation curves from Vogt's (1995) thesis. We summarize here the relevant results of the comparisons.

4.5.1 Systemic Velocities

Accurate calibration of the systemic recessional velocity scale is an important factor in determining the peculiar motions of extragalactic objects. For example, upon comparing their Sc redshifts with optical redshifts from MF and other sources, G98b noticed a velocity calibration error in the MF optical sample. The error monotonically increases with redshift, with an error of ~50 km s^{-1} at cz ~8,000 km s^{-1}. Such an error for an all-sky survey would result in artificially changing the Hubble constant with radial distance, a geocentric signature.

Panel (a) of Figure 4.12 displays the difference between the HI and optical systemic velocities of galaxies in the Pal/Sc HI overlap sample, plotted versus cz. There is no systematic bias apparent. An offset of 17 km s^{-1} has been added to the heliocentric velocities obtained at Palomar as listed in Vogt's (1995) thesis, where most of the optical velocities first appeared; this offset resulted from a wavelength calibration error. The scatter of the velocity difference in Figure 4.12, computed for 168 of 170 galaxies with velocity differences of less than 50 km s^{-1}, is 11 km s^{-1}.

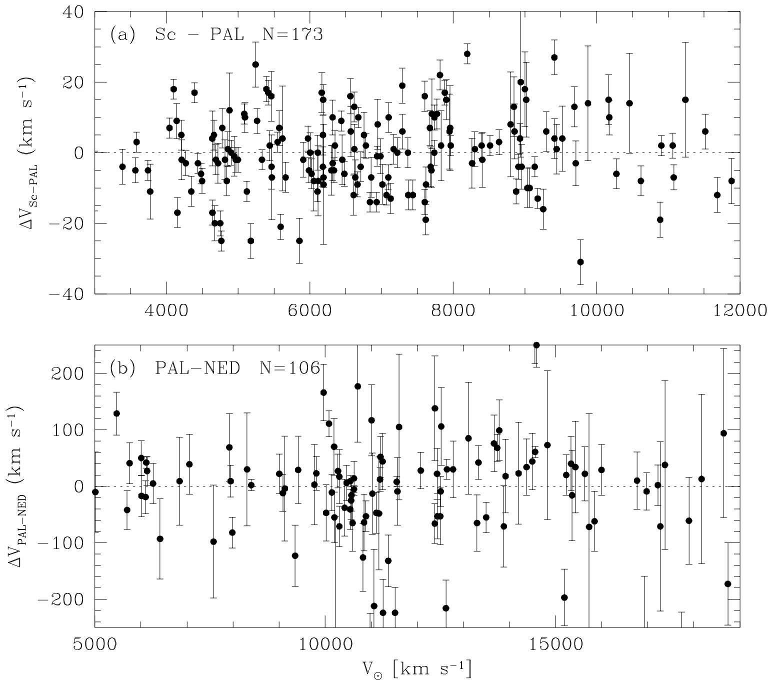

Figure 4.12 Panel (a): Difference between the 21 cm and optical radial velocities for 170 galaxies in the PAL/Sc HI overlap sample. Panel (b): Difference between the optical radial velocities for 106 galaxies in the Pal/NED overlap sample.

A second check can be made that concerns only the PAL data used in the SCII sample, the subset that lies at higher redshifts. To accomplish this we refer to the rather inhomogeneous optical spectroscopy data available from the literature (i.e. NED) – most 21 cm surveys do not yet extend beyond 12,000 km s^{-1}. Panel (b) of Figure 4.12 gives such a comparison. The velocity offset is only 4 km s^{-1}, with an rms scatter of 50 km s^{-1}.

4.5.2 Optical Velocity Widths

There are currently few large databases of optical rotation curves available. Hence, any direct comparisons of our velocity widths obtained from optical RCs with those from an external RC database will be limited. In fact, there are only 22 galaxies for which RCs exist in both the PAL and MF database. The mean difference in velocity widths for these 22 galaxies is 13 km s^{-1} (rms scatter of 20 km s^{-1}), with the PAL widths being larger on average. In computing this figure we fitted the RCs with the *PolyEx* model to remeasure the MF widths at r_{83}, for consistency with the PAL widths. We emphasize that this comparison is quite weak on statistical grounds and because of the poor quality of many of the MF RCs in the overlap sample.

An internal consistency check can also be made on the database, whereby velocity widths are remeasured from repeat observations. This is unfortunately a rather costly approach to verify data reliability, as telescope time on 5 m class telescopes is literally precious. Results from a small but statistically dubious "repeat sample" show negligibly different velocity widths. An alternative to this approach is to compare velocity widths as measured from different emission lines within the same spectrum. Vogt (1995) performed this consistency check for a portion of the PAL database and found no systematic differences between the two emission line widths.

4.5.3 Equilibration of Optical and Radio Width Scales

A set of conversion relations between different width estimates, for both optical and 21 cm data, was computed in Section 6.3.2 of G98b. It was found that the simplest set of relations referred to the extent of the optical RC, $r_{\rm cut}$. The relation of interest for this work is the conversion between optical widths measured at r_{83}, $W(r_{83})$, and radio widths measured from HI profiles. These are the two types of widths measured for this work, and they necessarily need to put on the same scale. G98b gives the following recursion relation:

$$W_{21,\rm Sc} - W(r_{83}) = -19.4 + 27.38\left(\frac{r_{\rm cut}}{r_{83}}\right) - 5.77\left(\frac{r_{\rm cut}}{r_{83}}\right)^2 \tag{4.22}$$

Since the vast majority of the widths used in this study derive from optical spectroscopy, we will convert 21 cm widths to the r_{83} scale. The above relation yields $W_{21,\rm Sc} - W(r_{83}) = 2.21$ km s^{-1} if we assume a constant ratio of $r_{\rm cut}/r_{83} \sim 1$, a fair approximation overall for our sample (see Figure 4.4). We prefer not to make such an approximation, however, and instead use the global offset found in G98b that is independent of $r_{\rm cut}$:

$$W_{21,\rm Sc} - W(r_{83}) = 3.3\mathrm{kms}^{-1}. \tag{4.23}$$

We use the above relation to convert radio widths to optical widths when computing TF relations for each cluster. This correction is only appropriate for velocity widths uncorrected for disk inclination.

4.6 Errors in Optical Velocity Widths

There are of course other factors that contribute to the uncertainty in a velocity width measurement besides those that involve the spectrograph slit. Another important factor that contributes to the uncertainty in W is the error in the measured inclination i (see Section 3.5). In practice we measure a disk's ellipticity, ϵ, so to describe inclinations in terms of ellipticities, we follow Hubble (1926) in assuming spiral disks are oblate spheroids with intrinsic axial ratio q:

$$\cos^2 i = \frac{(1-\epsilon)^2 - q^2}{1-q^2}. \tag{4.24}$$

We also follow the convention outlined G94 in adopting a value of q=0.13 for type Sbc and later and a value of q=0.2 for morphological types earlier than Sbc. Formally, the error in the inclination i can be expressed as

$$\sigma_i^2 = \left(\frac{di}{d\epsilon}\right)^2 \sigma_\epsilon^2 + \left(\frac{di}{dq}\right)^2 \sigma_q^2 = \left(\frac{(1-e)}{\sin i \cos i (1-q^2)}\right)^2 \sigma_\epsilon^2 + \left(\frac{q \tan i}{1-q^2}\right)^2 \sigma_q^2 \tag{4.25}$$

where σ_ϵ is the uncertainty in the disk ellipticity measurement and σ_q is the error in q, assumed to be $0.15q$.

We can now quantify the formal error in the velocity width (cf 4.12):

$$\sigma_W^2 = \frac{(\sigma_{W,\mathrm{obs}}^2 + \sigma_{\mathrm{sh}}^2) f_{\mathrm{slit}}^2}{(1+z)^2 \sin^2 i} + \sigma_i^2 W_{\mathrm{cor}}^2 \cot^2 i + \sigma_{\mathrm{slit}}^2 W_{\mathrm{cor}}^2 \tag{4.26}$$

where $\sigma_{W,\mathrm{obs}}$ is the error in the observed velocity width and σ_{sh} is the error in the shape correction applied, typically $0.25\Delta_{\mathrm{sh}}$. We find the error due to slit smearing and misalignment effects, σ_{slit}, to be roughly $0.25(f_{\mathrm{slit}} - 1)$. In other words, its error is also approximately one fourth the correction's amplitude. In the few cases where a 21 cm width is used, we follow G97a in computing errors in the widths.

Chapter 5

Data Presentation

In this chapter we present the data in its various forms. We start with the information that served as a first step in determining membership within a given cluster. Figure 5.1 shows the distribution of the galaxies in each cluster, in order of increasing right ascension. The top panel in each of these figures displays the spatial location of: the outline of the fields imaged (large squares), cluster members (circles — those with poor/unusable velocity widths are left unfilled), background or foreground objects (asterisks), and galaxies with known redshift but without reliable widths (dots). Circles of one and two Abell radii are drawn as dashed lines, if the area displayed is large enough. If no dashed circle is drawn, the Abell radius is larger than the figure limits. We also plot radial (CMB) velocity as a function of angular distance from the cluster center in the lower panel of each figure. A dashed vertical line is drawn at one Abell radius. The combination of the sky and velocity plots is used to gauge cluster membership for each galaxy.

The data used to generate Figure 5.1 derives from both the photometry and

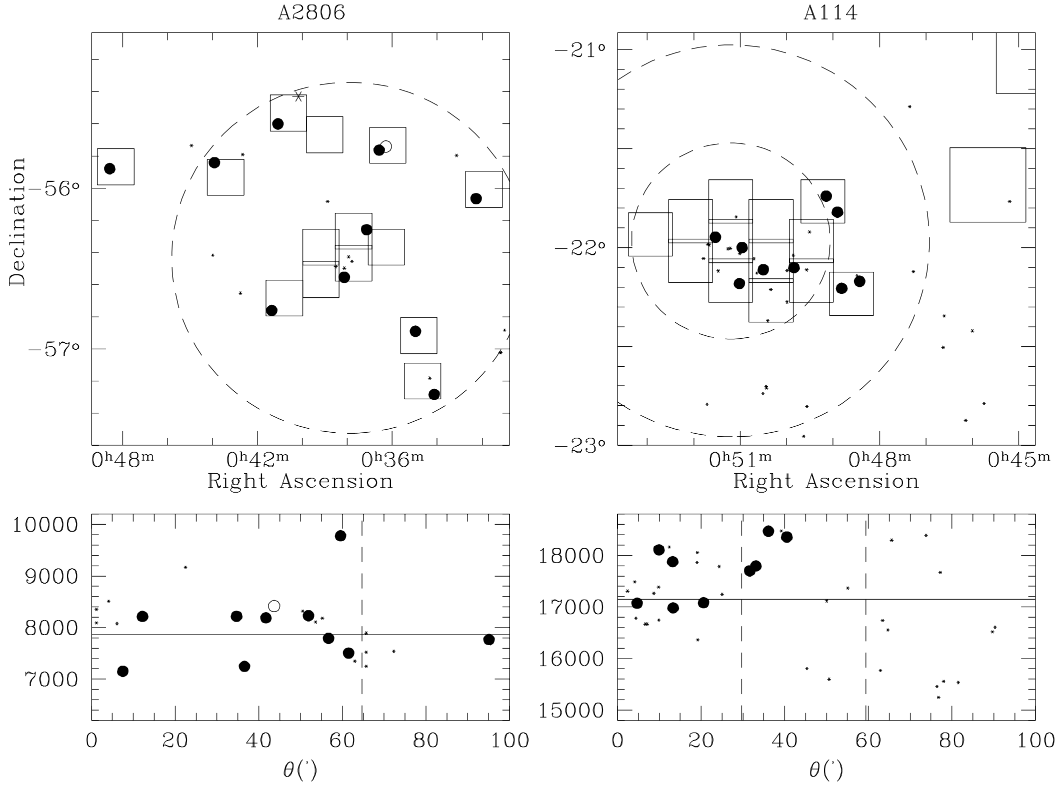

Figure 5.1 Sky and velocity distribution of galaxies in the cluster fields, in order of increasing cluster Rig!ht Ascension. Circles represent cluster members with measured photometry and widths; if unfilled, widths are poorly determined. Asterisks identify foreground and background galaxies and dots give the location of galaxies with known redshift, but lacking accurate width and/or photometry. Large square boxes indicate outlines of imaged fields with the 0.9 m telescope. Vertical dashed lines in the lower panels indicate 1 R_{A} (and occasionally 2 R_{A}). The upper panels contain circles of radius 1 R_{A} (and occasionally 2 R_{A}). For A2877b, A1736b, A1983b, and A2295b, filled triangles identify cluster members and 1 R_{A} is indicated by the dotted line in the lower panel and by the dotted circle of radius 1 R_{A} in the upper panel.

spectroscopy. Photometry was obtained for a large number of objects in the cluster fields, but whether or not a given galaxy's flux was extracted was dictated by the availability and quality of the spectroscopy. There are 489 RCs available from the 52 clusters studied, with 36 RCs coming from the thesis work of N. Vogt (1995). We separate photometric data and spectroscopic data into two tables.

Figure 5.1 (Continued)

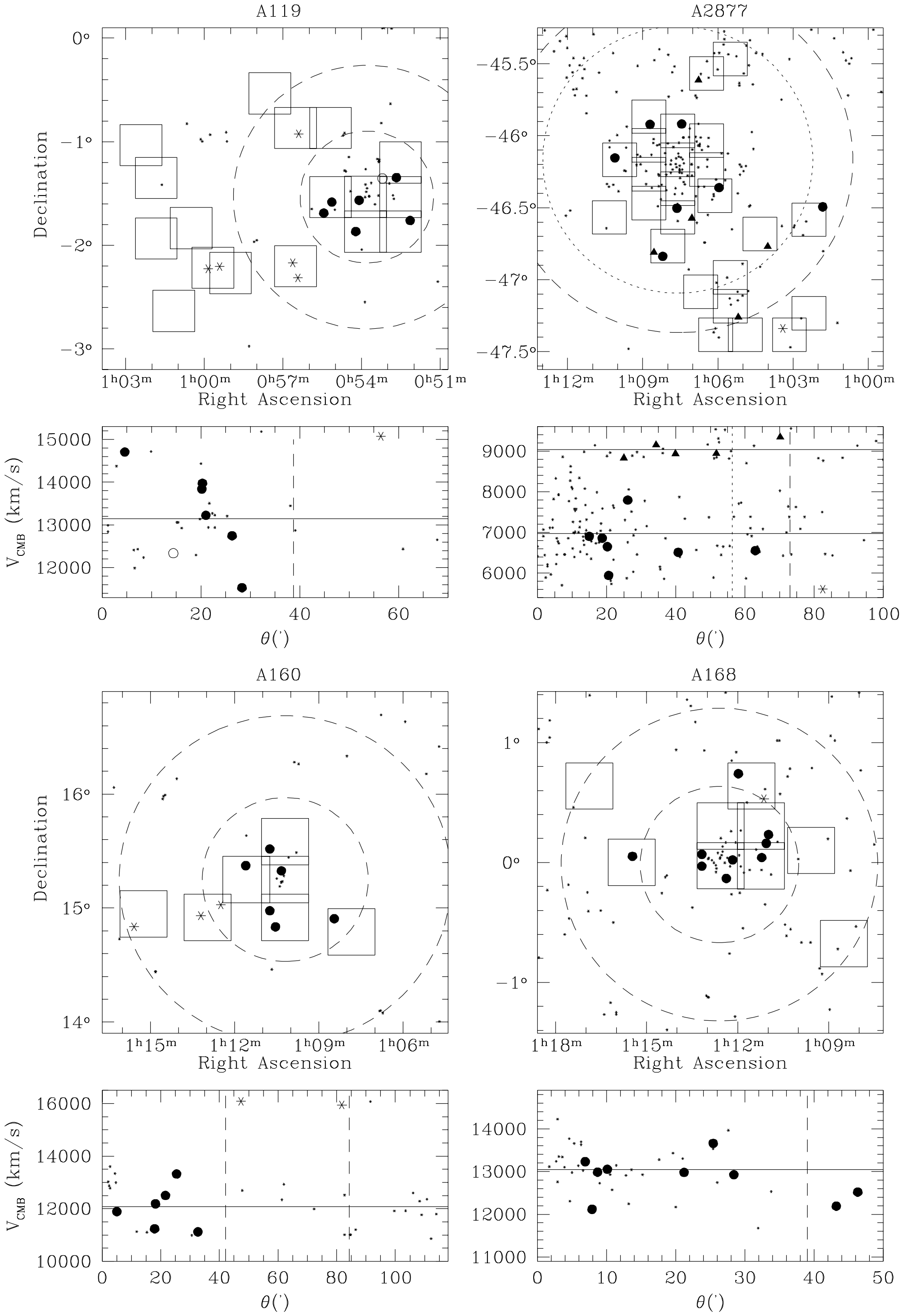

Figure 5.1 (Continued)

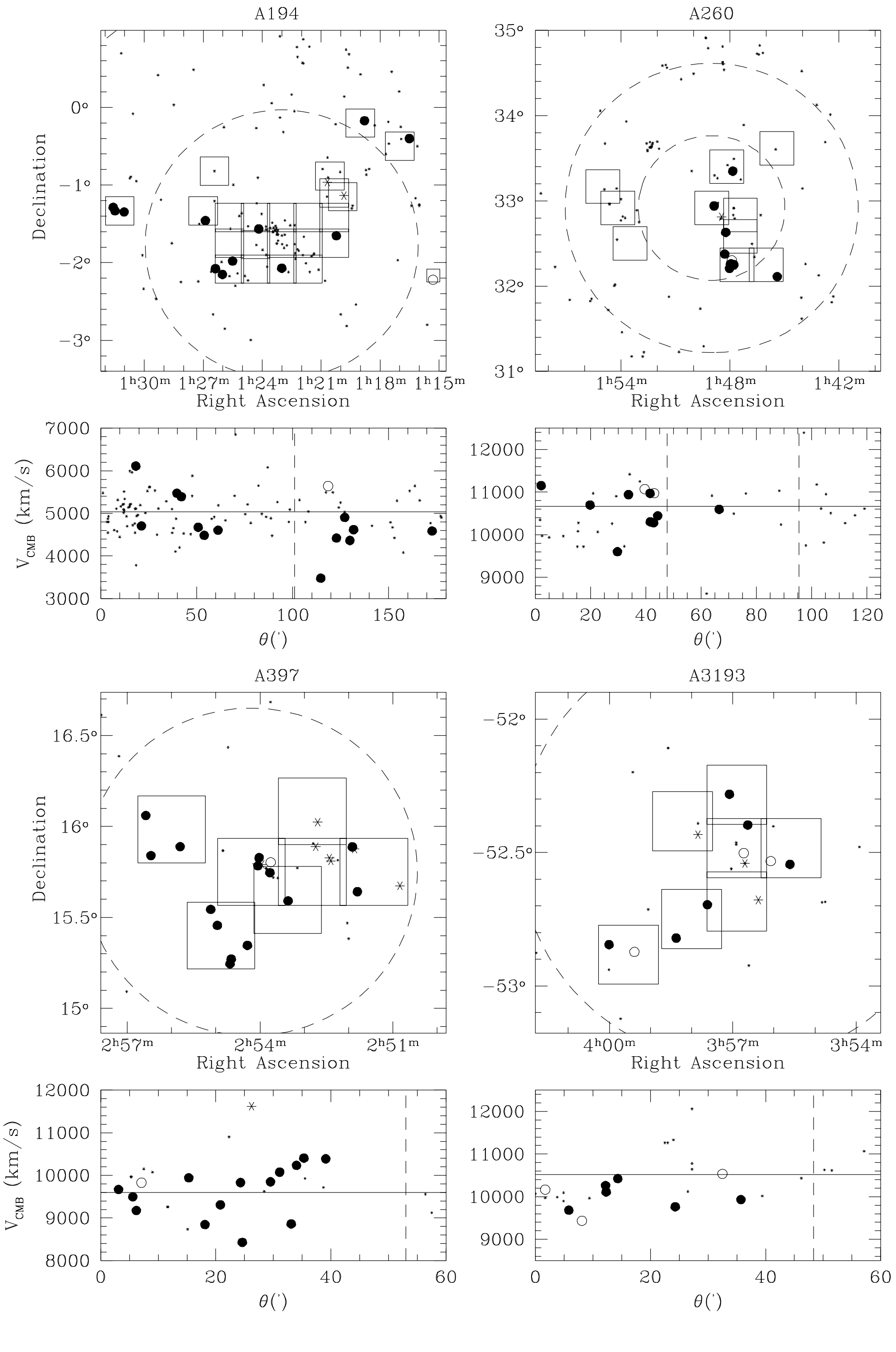

Figure 5.1 (Continued)

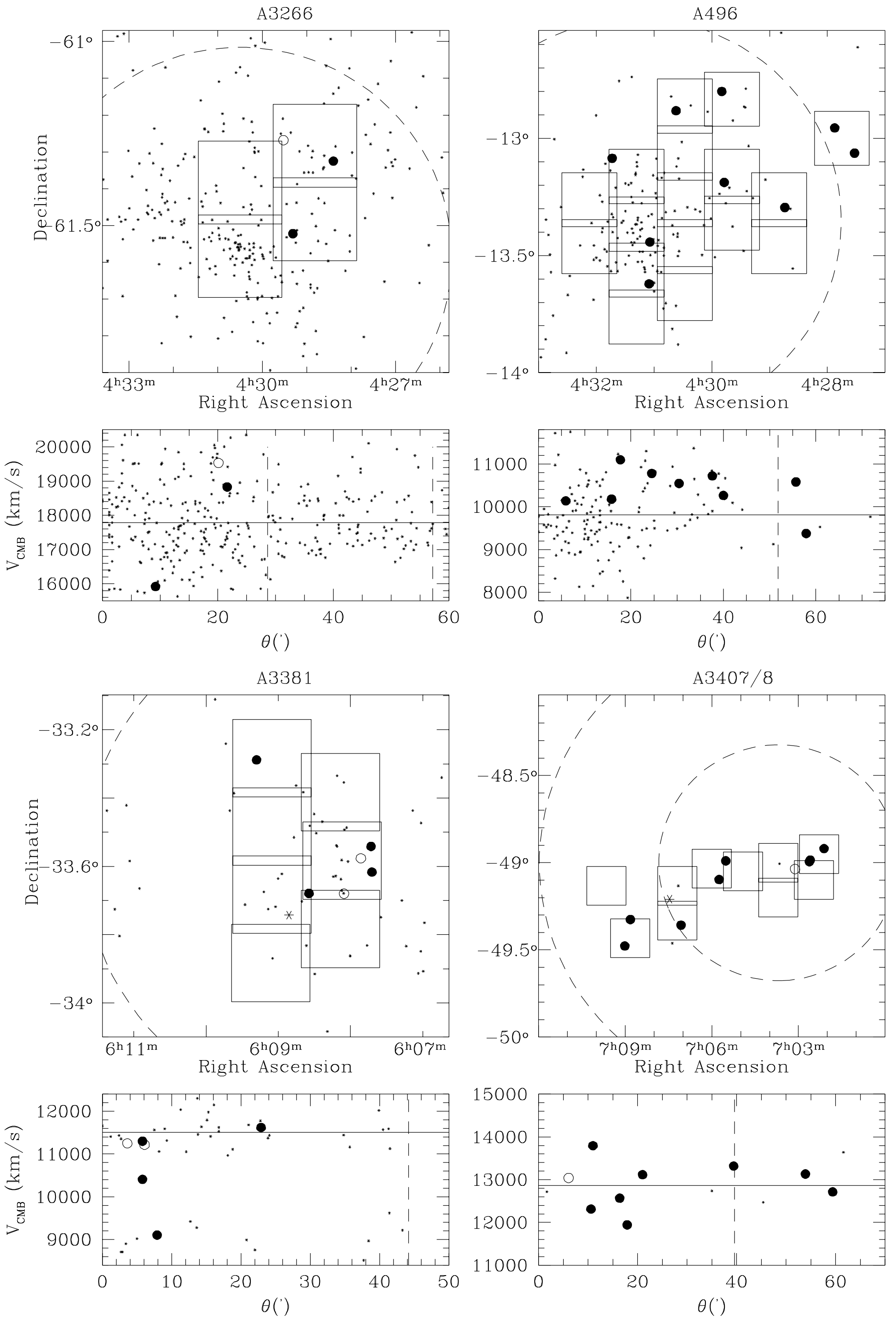

Figure 5.1 (Continued)

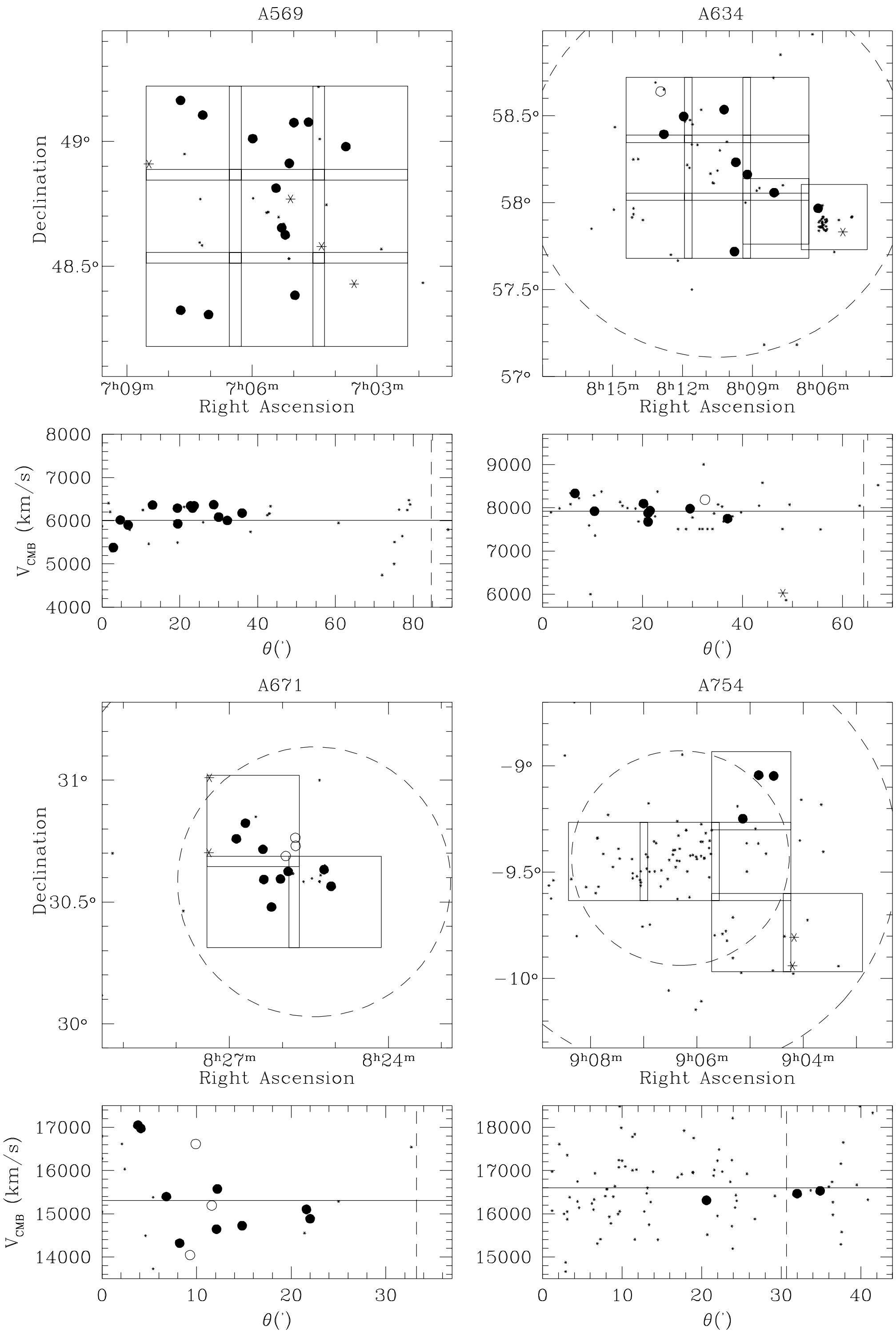

Figure 5.1 (Continued)

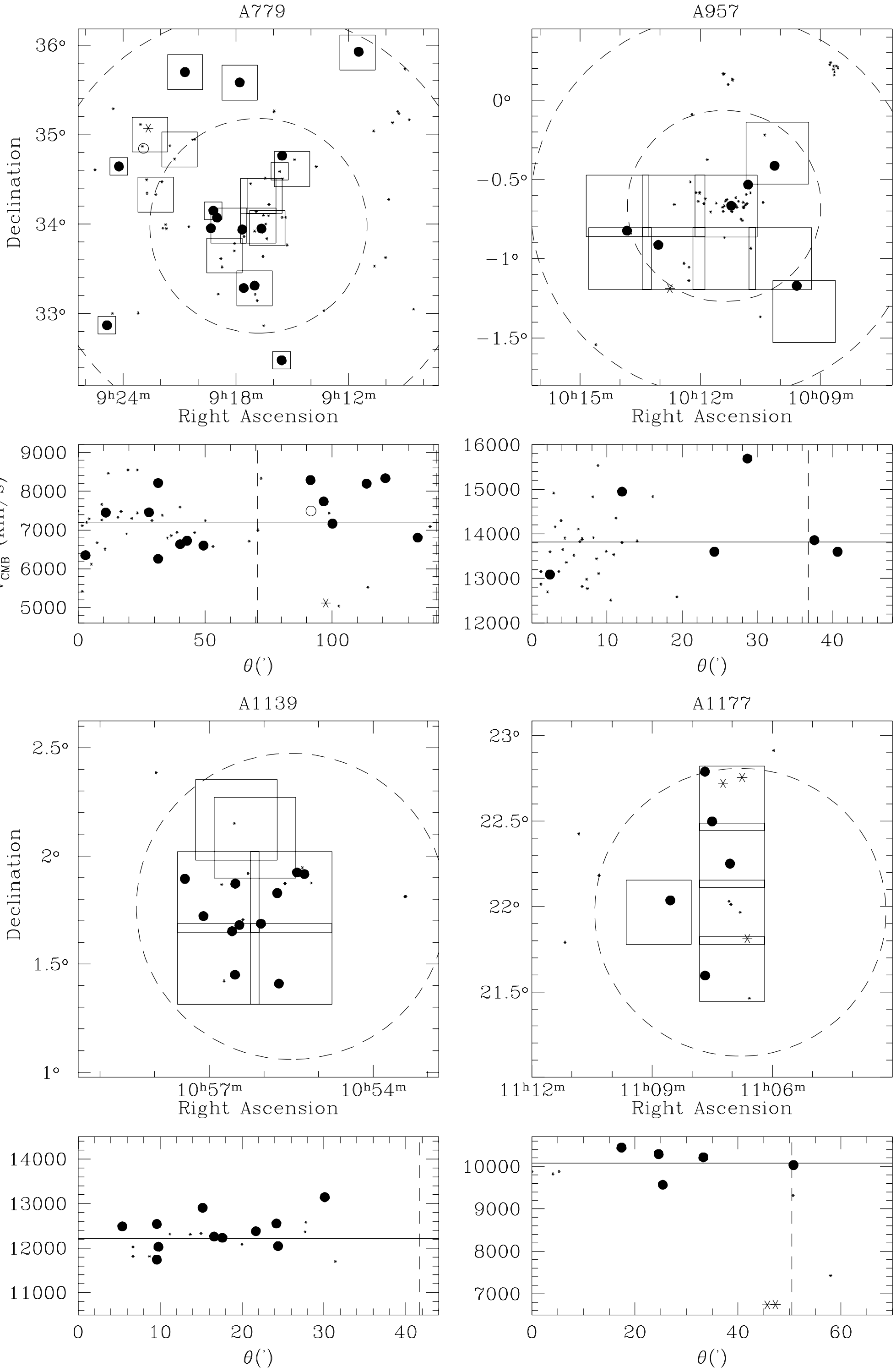

Figure 5.1 (Continued)

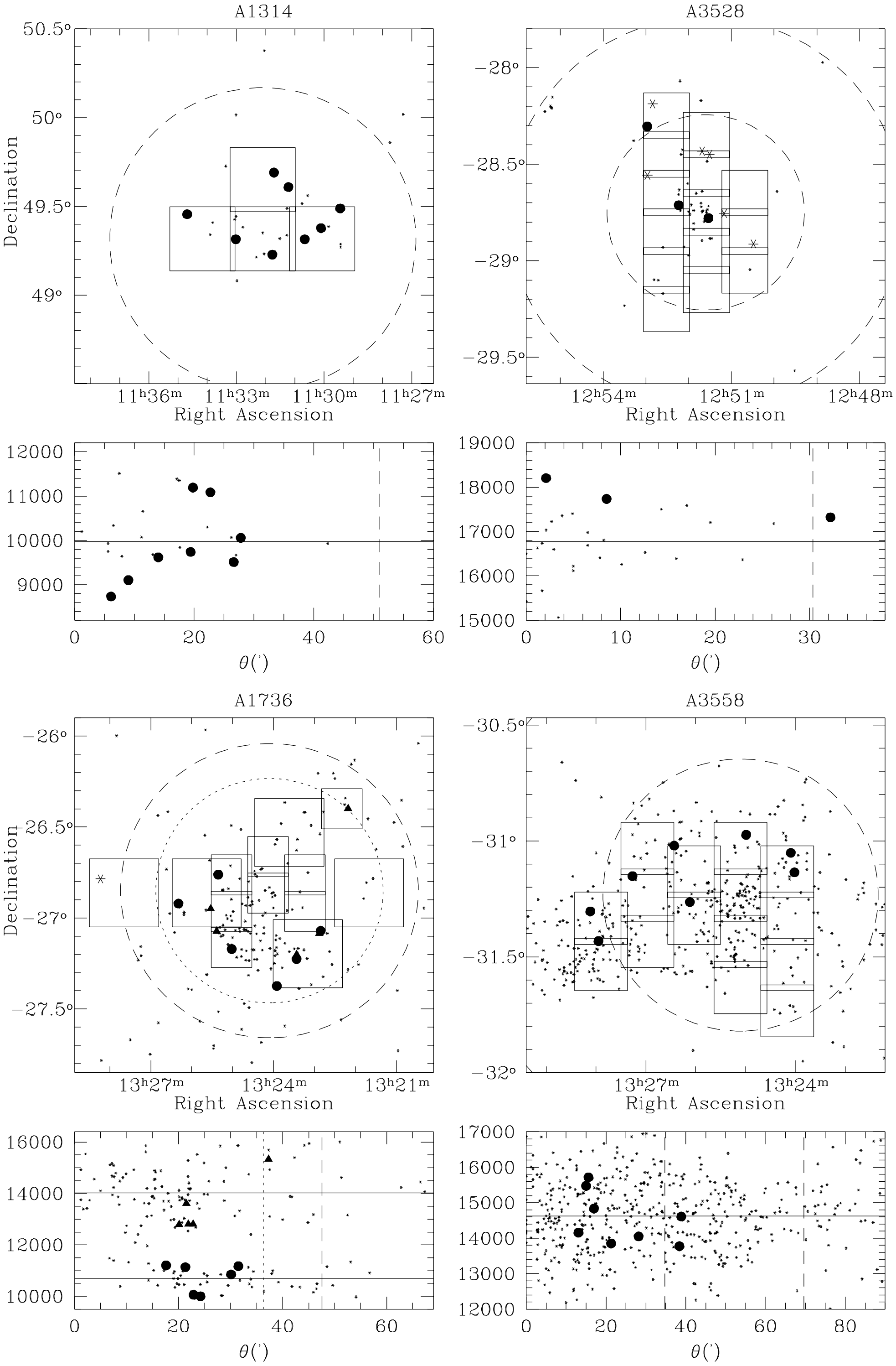

Figure 5.1 (Continued)

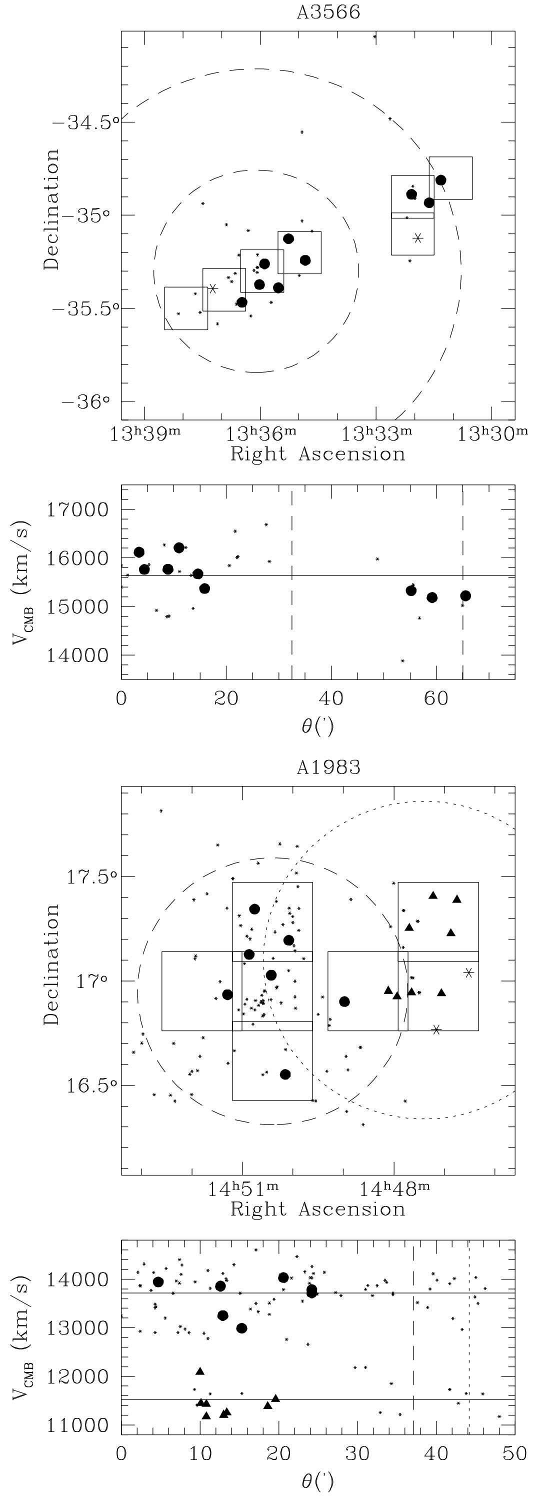

Figure 5.1 (Continued)

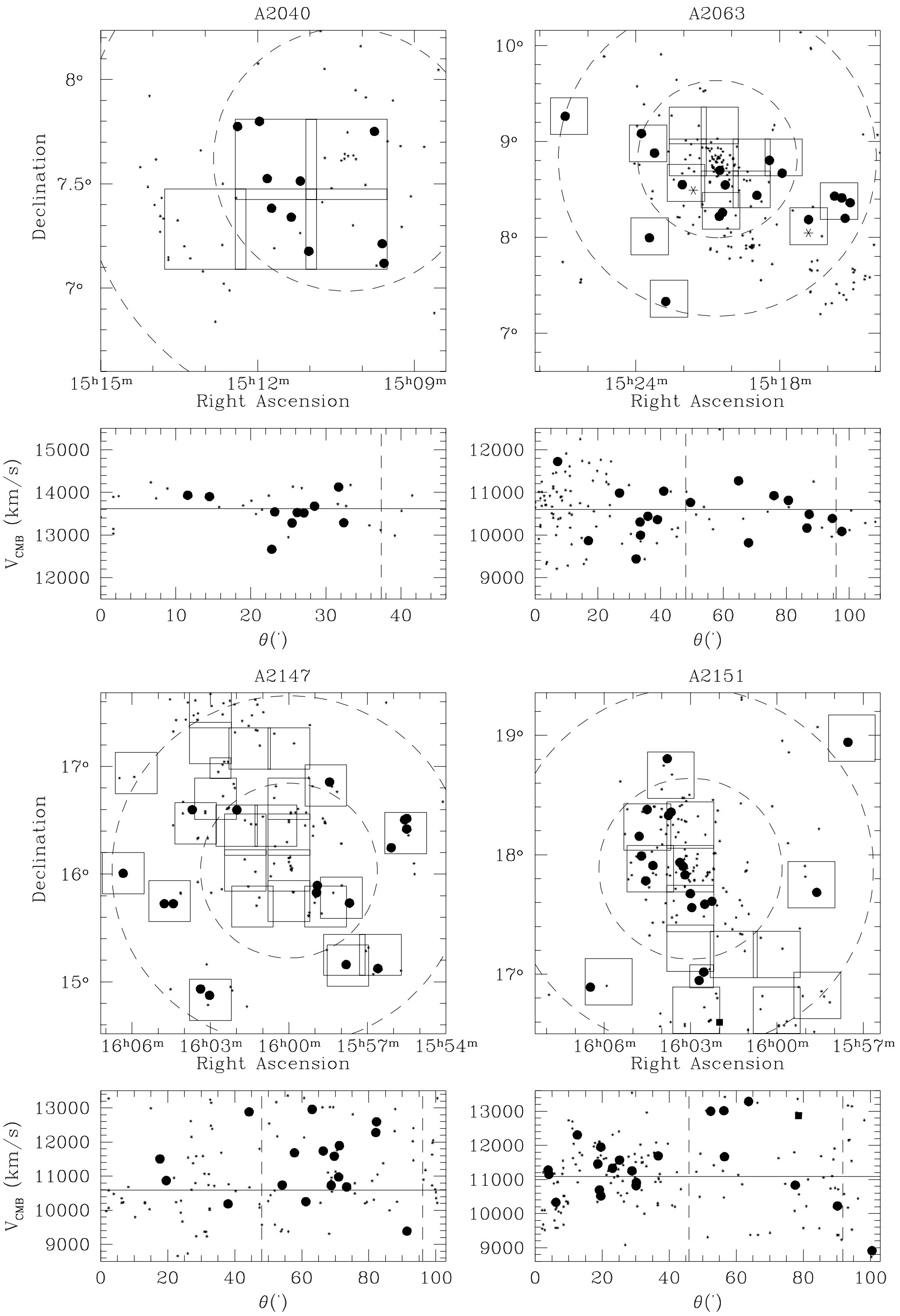

Figure 5.1 (Continued)

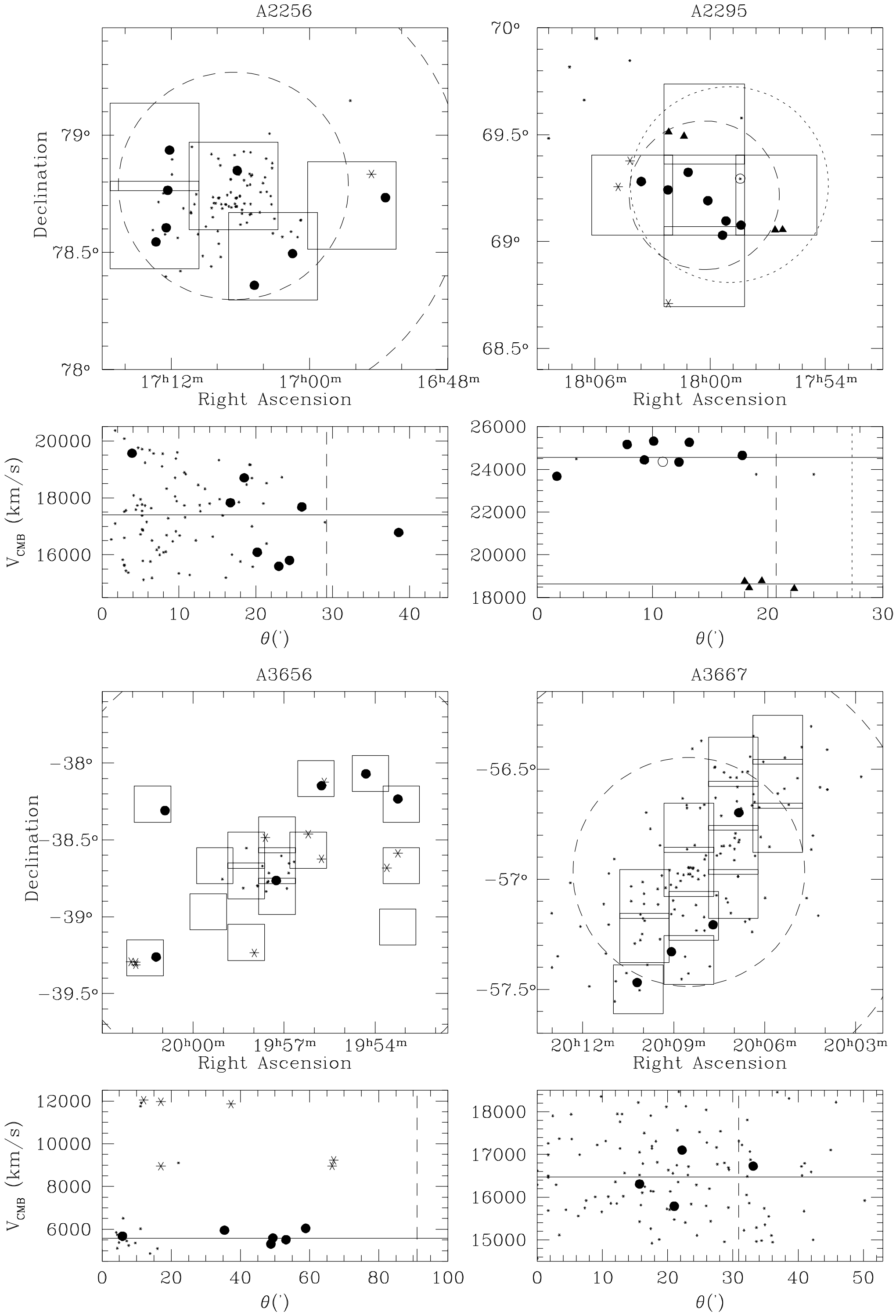

Figure 5.1 (Continued)

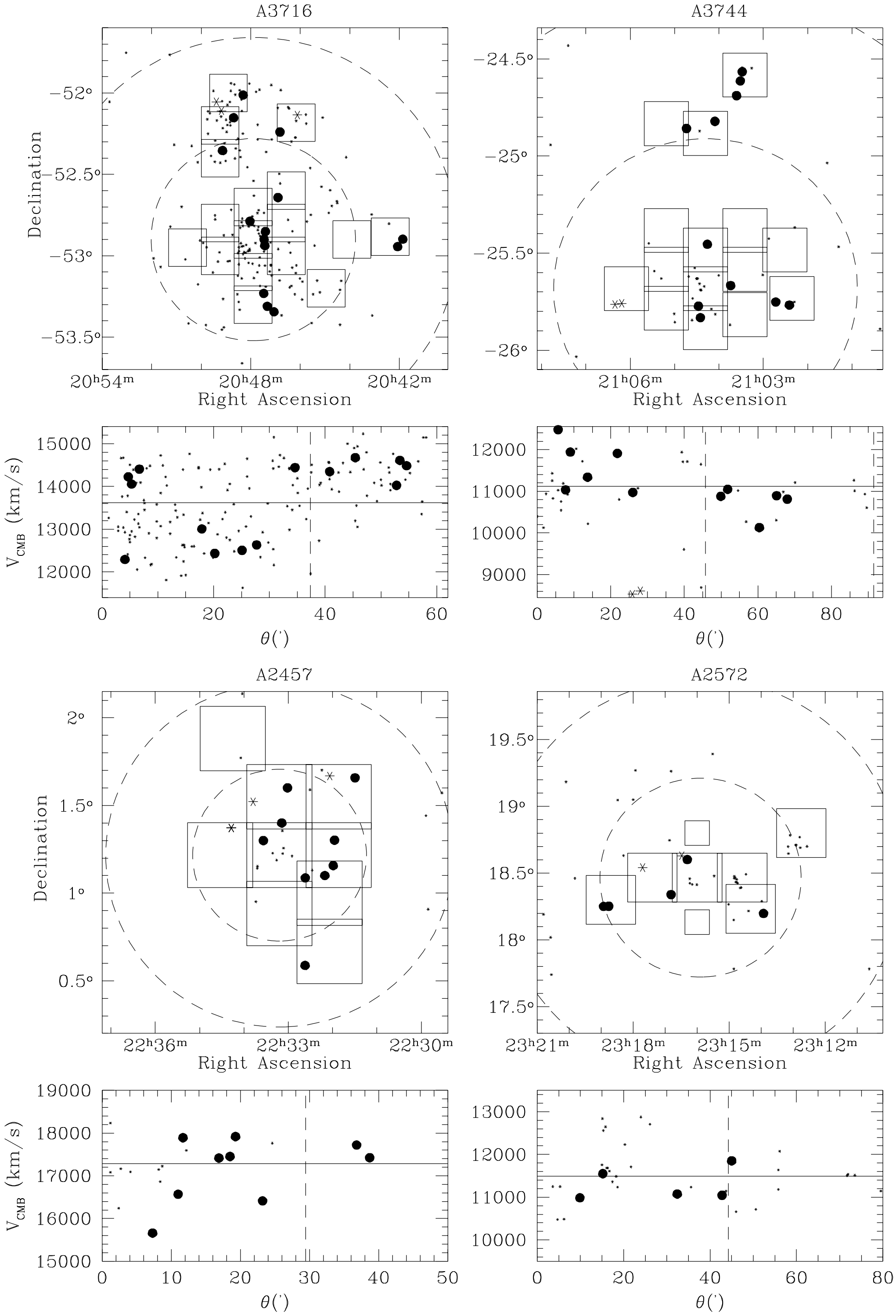

Figure 5.1 (Continued)

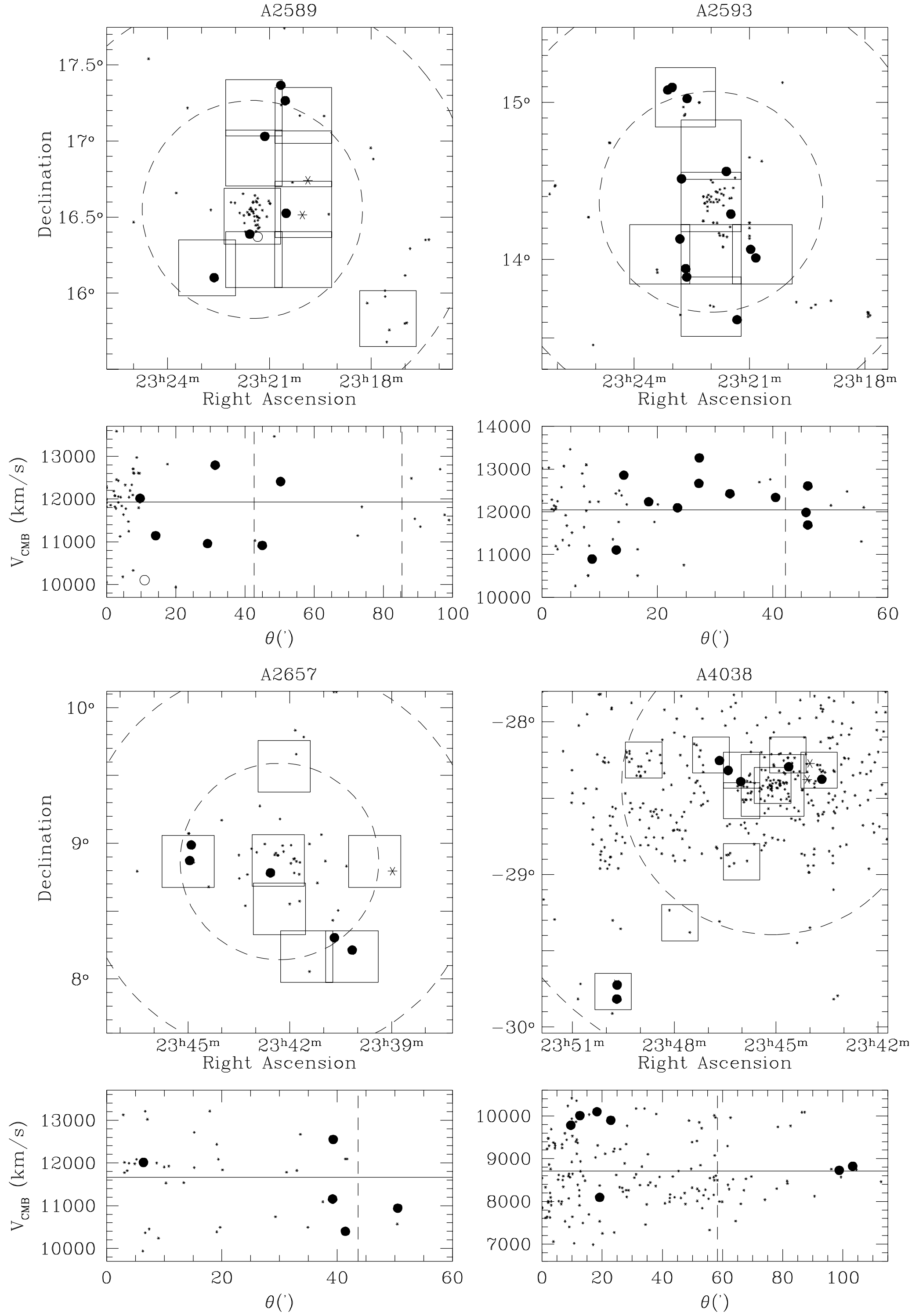

Table A.1 lists the spectroscopic properties and Table A.2 gives the pertinent photometric results (the tables are given in the appendix).

Entries in the tables are sorted first by the Right Ascension of each cluster, and within each cluster sample by increasing galaxy Right Ascension. The listed parameters for Table A.1 are:

Column 1: identification names corresponding to a coding number in our database, referred to as the Arecibo General Catalog.

Columns 2 and 3: Right Ascension and Declination in the 1950.0 epoch. Coordinates have been obtained from the Digitized Sky Survey catalog and are accurate to $< 2''$.

Columns 4: integration time for spectroscopy measurement. A dash indicates only a 21 cm spectrum is available.

Columns 5 and 6: the galaxy radial velocity as measured in the heliocentric and CMB reference frame (Kogut *et al.* 1993). Errors are parenthesized: e.g. 13241(08) implies 13241$\pm$08.

Column 7: the raw velocity width in km s^{-1}. Measurement of optical widths are described in Chapter 4; 21 cm line widths are denoted with a dagger and refer to values measured at a level of 50% of the profile horns.

Column 8: the velocity width in km s^{-1} at r_{83} after correcting for RC shape, the cosmological stretch of the data, slit effects and, for 21 cm data, signal to noise effects, interstellar medium turbulence, and instrumental and data processing broadening; details on the adopted corrections for optical and 21 cm data are given in Section 4.4.2 and G97a, respectively.

Column 9: the corrected velocity width in km s^{-1} converted to an edge–on perspective.

Column 10: the adopted inclination i of the plane of the disk to the line of sight, in degrees, (90° corresponding to edge–on perspective); the derivation of i and its associated uncertainty are discussed in Section 4.6.

Column 11: the logarithm in base 10 of the corrected velocity width (value in column 7), together with its estimated uncertainty between brackets. The uncertainty takes into account both measurement errors and uncertainties arising from the corrections. The format 2.576(22), for example, is equivalent to 2.576±0.022.

The position angle adopted for the slit of each spectroscopic observation is that given in column 4 of Table A.2. The first column in Table A.2 matches that of Table A.1. The remaining listed parameters for Table A.2 are:

Column 2: morphological type code in the RC3 scheme, where code 1 corresponds to Sa, code 3 to Sb, code 5 to Sc and so on. When the type code is followed by a "B", the galaxy disk has an identifiable bar. We assign these codes after visually inspecting the CCD I band images and after noting the value of R_{75}/R_{25}, where R_N is the radius containing $N\%$ of the I band flux. This ratio is a measure of the central concentration of the flux can be computed analytically for a variety of bulge–to–disk ratios. Given the limited resolution of the images, some of the inferred types are rather uncertain; uncertain types are followed by a colon.

Column 3: the angular distance θ in arcminutes from the center of each cluster.

Column 4: position angle of the major axis of the image, also used for spectrograph slit positioning (North: 0°, East: 90°).

Column 5: observed ellipticity of the disk.

Column 6: ellipticity corrected for seeing effects as described in Section 3.4, along with its corresponding uncertainty. The format 0.780(16), for example, is equivalent to 0.780±0.016.

Column 7: surface brightness of the disk at zero radius, as extrapolated from the fit to the disk surface brightness profile.

Column 8: the (exponential) disk scalelength.

Column 9: the distance along the major axis to the isophote containing 83% of the I band flux.

Column 10: the measured I band magnitude, extrapolated to $8r_{\rm d}^{\circ}$ assuming that the surface brightness profile of the disk is well described by an exponential function.

Column 11: the apparent magnitude, to which k–term, Galactic and internal extinction corrections were applied; details on the adopted corrections are given in Section 3.3.

Column 12: the absolute magnitude, computed assuming that the galaxy is at the distance indicated either by the cluster redshift, if the galaxy is a cluster member within one Abell radius of the cluster center, or by the galaxy redshift if not. The calculation assumes $H_{\circ} = 100h$ km s^{-1} Mpc^{-1}, so the value listed is strictly $M_{\rm cor} - 5\log h$. In calculating this parameter, radial velocities are expressed in the CMB frame and uncorrected for any cluster peculiar motion. The uncertainty on the magnitude, indicated between brackets in hundredths of a mag, is the sum in quadrature of the measurement errors and the estimate of the uncertainty in the corrections applied to the measured parameter.

When an asterisk appears at the end of the record, a detailed comment is given for that particular object. Because of the length and number of these comments, they are not appended to the table but included in the text as follows. Note that a record is flagged in both tables A.1 and A.2, independently on whether the comments refer only to the photometry, only to the spectroscopy, or both.

A2806:

20391: Possible disk warp; [NII] patch for radii $< 8''$

400698: Mostly bulge RC; uncertain extrapolation.

400703: Mostly bulge RC; uncertain extrapolation; unfit for TF use.

400713: mostly bulge RC; large extrapolation; exponential disk over narrow range of radii.

A114:

400672: Exponential disk over narrow range of radii.

400443: Uncertain ellipticity; Hα absorption in bulge – [NII] patch for radii $< 3''$; two nuclei?

400453: Uncertain PA.

A119:

400619: Exponential disk over narrow range of radii; Hα absorption in bulge – [NII] patch for radii $< 2.5''$.

400600: Uncertain RC extrapolation; [NII] line used.

400641: Uncertain ellipticity; [NII] patch for radii $\lesssim 2''$.

400658: Background galaxy.

A2877:

20791: Foreground galaxy.

410675: Note low i.

20893: Asymmetric I band profile.

A2877b:

20797: Note low i.

20845: Note low i; ellipticity uncertain.

A160:

110104: Only 21 cm width available.

110968: Unusual spiral arm pattern.

110975: Background galaxy; 5 minute integration.

110976: Background galaxy.

110977: Background galaxy.

A168:

110868: HII distribution patchy and does not extend far radially; exponential disk over narrow range of radii.

110877: Asymmetric RC.

110879: Asymmetric central region, both in image and RC; difficult to determine ellipticity.

410553: Mostly bulge RC; tiny galaxy.

A194:

784: Only 21 cm width available.

830: Only 21 cm width available; note low i; unfit for TF use.

894: Foreground galaxy; only 21 cm width available.

915: Background galaxy; only 21 cm width available.

931: Foreground galaxy; only 21 cm width available.

410584: Asymmetric nucleus.

1116: Only 21 cm width available.

1120: Only 21 cm width available.

1123: Only 21 cm width available.

A260:

110558: Marginal quality 21 cm width also available.

110805: Mostly bulge RC; [NII] patch on receding side of RC for $r \gtrsim 2''$; companion $45''$ to East; unfit for TF use.

110937: Background galaxy; 5 minute integration.

A397:

121137: Background galaxy.

120587: Probably used incorrect PA; 21 cm width preferred; note low i.

121055: Background galaxy

121143: Tiny galaxy; RC still rising at optical radius; poorly determined 21 cm width.

121145: Background galaxy

121060: Background galaxy

121061: Background galaxy

2406: Patchy HII; good agreement between 21 cm and RC width; used [NII] RC.

120614: Only 21 cm width available; note early type; unfit for TF use.

121154: Mostly bulge RC; uncertain velocity width.

121157: Background galaxy.

120632: Poor HII sampling; 21 cm width available.

2420: Asymmetric HII distribution; compatible RC and 21 cm widths.

120651: Asymmetric RC; PA uncertain; 21 cm width used.

120652: Hα absorption in bulge; note low i; good agreement between 21 cm and RC width.

121080: Note low i; compatible 21 cm and RC widths.

121082: Only 21 cm width available; caution: nearby star may perturb photometry.

121085: Patchy HII; uncertain PA.

2453: Uncertain ellipticity; Hα absorption in bulge; $W_{\rm opt} = 360$ km s^{-1}; 21 cm width available.

A3193:

23113: Note low i.

23130: Extremely low surface brightness at radii $\gtrsim 20''$; heavy Hα absorption throughout disk; unfit for TF use.

23136: Note low i; [NII] patch for radii $\lesssim 0.5''$.

A3266:

440559: Note low i; uncertain ellipticity; unfit for TF use; center-of-light peak used for RC spatial center.

A496:

440516: Atypical emission characteristics on receding side of RC for both Hα and [SII] lines.

440519: Rising RC.

A3381:

460069: Rising RC; uncertain extrapolation.

460071: Hα absorption in bulge.

24895: Companion galaxy $35''$ to SE.

A3407:

470039: Uncertain ellipticity; image partly truncated by frame edge; complex velocity profile; unfit for TF use.

470051: Background galaxy.

470058: Disk warp?

A569:

170433: RC still rising.

170437: Background galaxy.

170438: RC only from bulge.

170439: RC still rising?

140440: Note low i.

170442: RC slightly rising.

170446: Exponential disk over small range of radii.

170057: RC slightly rising.

3724: Only 21 cm width available.

170063: Sd or irregular morphology?

170468: Background galaxy.

A634:

180807: Foreground galaxy; PA off 9° from major axis.

180715: Mostly bulge RC; unfit for TF use.

A671:

180287: Uncertain RC extrapolation.

180802: Background galaxy; 5 minute integration.

180803: Background galaxy.

A754:

490235: Foreground galaxy; 5 minute integration.

490249: 5 minute integration.

A779:

4865: Vogt RC; marginal quality 21 cm width also available.

4926: Vogt RC; compatible optical and 21 cm widths.

190187: Only 21 cm width available.

4941: Vogt RC; mildly discrepant (5%) optical and 21 cm widths; companions.

4949: Vogt RC; discrepant (10%) optical and 21 cm widths.

190224: Vogt RC; 21 cm width preferred.

190225: Only 21 cm width available; nearby star.

4960: Only 21 cm width available; Note low i.

190243: Comparable 21 cm width.

190203: Vogt RC.

190252: Only 21 cm width available.

5014: Only 21 cm width available.

190765: Only 21 cm width available.

190293: Only 21 cm width available.

5041: Only 21 cm width available.

A957:

500048: $1''$ slit used.

500344: Background galaxy.

500345: Background galaxy; 5 minute integration.

A1139:

200723: Mostly bulge RC.

200743: Mostly bulge RC.

201069: Mostly bulge RC; uncertain velocity width.

A1177:

211452: Background galaxy; incorrect PA used.

211453: Foreground galaxy; asymmetric I band profile; possible stripped disk.

211459: Foreground galaxy.

211499: Rising RC.

211500: [NII] RC; unfit for TF use?.

A1213:

211561: Background galaxy; 5 minute integration.

211561: [NII] RC.

6292: Interacting? Distorted spiral structure; unfit for TF use.

A1228:

6357: Only 21 cm width available.

6364: Dust lane along major axis; optical radius significantly larger than RC's extent; used [NII] RC.

211475: Background galaxy.

211476: Bar distorts RC; unfit for TF use.

211406: Asymmetric RC; tiny disk.

A1314:

211621: Rising RC.

211634: Asymmetric I band profile.

211641: Dust lane.

A3528:

520509: Background galaxy.

520227: Background galaxy.

520482: Background galaxy; 5 minute integration; rising RC.

520535: Background galaxy.

28988: Foreground galaxy; 5 minute integration.

520530: Background galaxy.

A1736:

29640: nearby star; low S/N RC data.

A1736b:

530430: Uncertain RC extrapolation; unfit for TF use.

530432: Not kinematically centered; $W_{\rm obs} = 2V_{\rm rot,red}$.

A3558:

530179: Interacting triplet?

530448: Not kinematically centered.

530456: [NII] patch for radii $\lesssim 2''$.

530471: Uncertain ellipticity; warped disk?

530474: PA off 17° from major axis.

530478: Not kinematically centered.

A3566:

530519: PA off 13° from major axis.

530530: COL centering used.

530537: [NII] patch for radii $\lesssim 1''$.

530541: [NII] RC.

A3581:

540202: Background galaxy.

A1983b:

241056: Background galaxy; not used in fits.

9538: Unreliable RC; severe Hα absorption; 21 cm width available.

241059: Only 21 cm width available.

241061: Background galaxy; Hα partially absorbed and λ6548 completely absorbed!

241296: Large extrapolation to RC.

240746: Only 21 cm width available.

240747: 21 cm width available; interacting w/faint companion? Probably unfit for TF use.

9548: Low velocity horn in 21 cm data poorly defined.

9550: Compatible RC and 21 cm widths.

A1983:

241306: Only 21 cm width available.

240823: Only 21 cm width available.

240840: Mostly bulge RC.

241298: Weak, patchy HII distribution, but RC fine.

A2022:

250021: Interacting w/250022?

250022: Interacting w/250021?

251792: [NII] RC; rising RC; spatial center forced to match COL position.

251793: Rising RC; PA off 9° from major axis.

251802: Background galaxy.

A2040:

251754: Not kinematically centered; $W_{\rm obs} = 2V_{\rm rot,blue}$.

250266: [NII] RC.

250374: Uncertain RC extrapolation.

A2063:

250443: Vogt RC; 21 cm width used.

250472: Vogt RC; compatible widths from RC and 21 cm profile.

250473: Background galaxy; only 21 cm width available.

251814: [NII] RC; RC still rising.

251816: Faint dust lane.

250632: fair quality 21 cm width also available.

250641: Bulge off-center; fair quality 21 cm width also available.

250644: Irregular? Bulge off-centered.

250716: Background galaxy; 5 minute integration.

250740: Vogt RC; compatible widths from RC and 21 cm profile.

9838: Vogt RC.

250786: [NII] RC; fair quality 21 cm width also available.

9844: Vogt RC; compatible widths from RC and 21 cm profile.

250803: Vogt RC; compatible widths from RC and 21 cm profile.

250896: Vogt RC; 21 cm width also available.

A2147:

251498: Only 21 cm width available.

251753: Note low i; PA off 15° from major axis.

251400: Vogt RC; confused 21 cm profile also available.

251424: Vogt RC.

251503: Vogt RC.

251436: Vogt RC; incorrect PA used.

251509: Vogt RC.

10131: Only 21 cm width available.

251510: Vogt RC; marginal quality 21 cm width also available; average of optical and 21 cm widths used.

260959: Only 21 cm width available.

260246: Poor Vogt RC; 21 cm width preferred. Asymmetric I band profile.

260963: Only 21 cm width available.

10287: 21 cm width preferred; Note low i; incorrect PA used for RC.

A2151:

10121: Vogt RC; discrepant optical and 21 cm widths; 21 cm width used.

251442: Only 21 cm width available.

260091: Vogt RC; uncertain $W_{\rm obs}$.

260112: Vogt RC; note low i; PA off 11° from major axis.

260116: Vogt RC.

260953: Vogt RC; compatible optical and 21 cm widths.

10177: Vogt RC; warped disk? Compatible optical and 21 cm widths.

10180: Vogt RC; PA off 11° from major axis.

260146: Vogt RC.

10190: Vogt RC; 21 cm width preferred.

260184: Vogt RC; note low i; PA off 18° from major axis.

10195: Vogt RC.

260208: Vogt RC; compatible optical and 21 cm widths; ellipticity uncertain.

260226: Vogt RC; dust lane; i set to 88°.

260245: Vogt RC.

260247: Only 21 cm width available.

260284: Vogt RC; center-of-light peak used for RC spatial center; comparable 21 cm width also available.

260302: Vogt RC; compatible 21 cm and optical widths.

A2256:

261191: Foreground galaxy; 5 minute integration.

270144: Uncertain ellipticity.

270148: [NII] RC; rising RC.

270385: [NII] patch for radii $\lesssim 2''$; PA off 11° from major axis.

270172: Rising RC.

A2295b:

270370: Rising RC; uncertain extrapolation; uncertain PA.

280128: Mostly bulgy RC.

280130: Star $40''$ to WNW.

280134: Foreground galaxy.

A2295:

270375: Rising RC; note low i; small companion galaxy $10''$ to E; unfit for TF use; 5 minute integration.

280131: Background galaxy.

280136: Background galaxy.

A3656:

590070: Background galaxy.

590071: Background galaxy.

32903: Nearby star; PA uncertain.

590083: Background galaxy; nearby star.

590073: Background galaxy; Note low i.

590074: Background galaxy.

32965: Background galaxy.

590088: Background galaxy.

600332: Background galaxy.

600333: Background galaxy; [NII] patch for radii $\lesssim 6''$.

600334: Background galaxy.

A3716:

600243: Rising RC.

600251: Foreground galaxy.

33829: Low S/N on receding side of RC.

600264: Asymmetric I band profile.

33844: Rising RC; prominent dust lane.

600270: Not kinematically centered.

33851: [NII] patch for radii $\lesssim 4''$.

600289: Nearby star.

600309: Background galaxy.

33887: Background galaxy; [NII] patch for radii $\lesssim 3''$; Note low i; PA uncertain.

A3744:

610196: Rising RC; large extrapolation.

610198: Rising RC.

34131: Faint disk; large extrapolation made to RC.

610220: Heavy Hα absorption in one half of disk.

610222: Slightly rising RC.

34189: Foreground galaxy; patchy HII distribution.

610251: Foreground galaxy.

A2457:

320572: Mostly bulge RC; large correction applied to $W_{\rm RC}$; [NII] line used.

320573: Inner/outer isophotes differ in ellipticity and PA.

320574: Background galaxy.

320576: Star 55$''$ to NE; uncertain ellipticity; [NII] patch for radii $\lesssim 1.5''$.

320579: Slightly rising RC; uncertain ellipticity; [NII] patch for $2'' \lesssim$ radii $\lesssim 4''$.

320581: [NII] patch for radii $\lesssim 2''$.

320583: Asymmetric merger?

320591: Foreground galaxy; 5 minute integration.

A2572:

331603: Background galaxy; 5 minute integration.

331606: Background galaxy; 5 minute integration.

A2589:

330292: Background galaxy.

331577: Background galaxy.

330318: Not kinematically centered.

331686: Asymmetric I band profile; uncertain ellipticity.

331163: Fair quality 21 cm width also available.

330362: Note low i; uncertain RC extrapolation; unfit for TF use.

A2593:

331695: Irregular?

331702: Rising RC.

331726: Note low i; $R_{\rm opt}$ unreliable.

331727: Asymmetric I band profile.

331737: [NII] patch for radii $\lesssim 7''$.

A2657:

331608: Foreground galaxy; 5 minute integration; member of triplet?

331611: Companion $40''$ to East.

331612: Rising RC.

330872: [NII] patch for radii $\lesssim 5''$.

A4038:

36309: [NII] patch for radii $\lesssim 5''$.

630396: Background galaxy; 5 minute integration.

630397: Background galaxy; Note low i.

630400: [NII] patch for radii $\lesssim 2''$.

630408: Note low i.

630414: [NII] patch for radii $\lesssim 4''$.

36409: [NII] patch for radii $\lesssim 1''$.

630424: Background galaxy; c$z \sim$ 43,000 km s^{-1}; rising RC.

We present some general characteristics of the data sample in the form of various histograms in Figure 5.2. Panels (a) and (b) are the corrected apparent and absolute magnitude distributions in the I band, with a Schecter LF ($M^* = -21.6, \alpha = -0.5$) overlayed in panel (b). The full rotational velocity widths, corrected for all effects discussed in Chapter 4, are given in panel (c), while panel (d) plots the redshift distribution of the entire data sample, foreground and background objects included. We use the axial ratios in panel (e) to infer disk

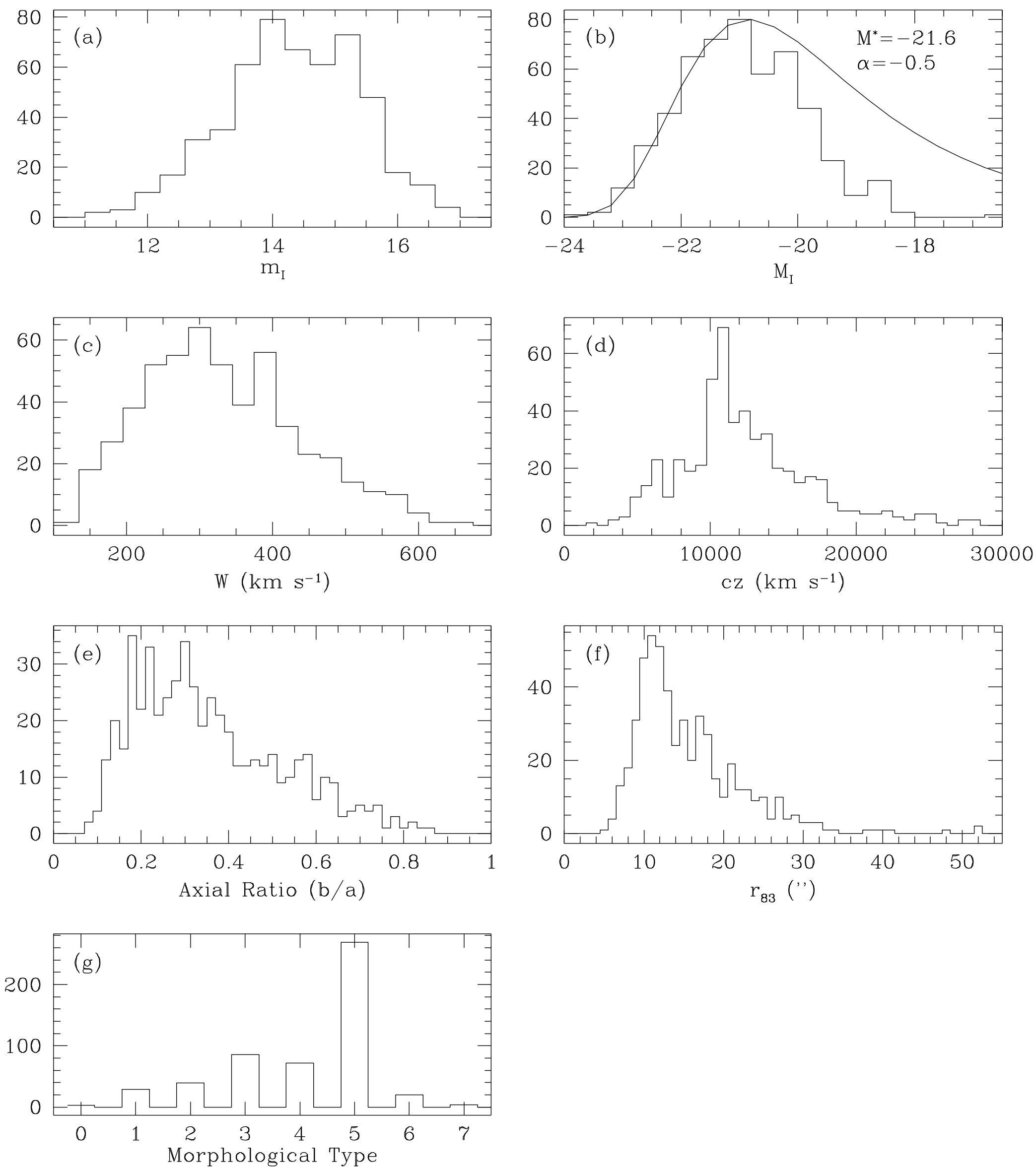

Figure 5.2 Several distributions for the data are displayed. From left to right, top to bottom: *I* band apparent magnitude, *I* band absolute magnitude (with Schecter function superimposed), rotational velocity width, recessional velocity in CMB frame, ratio of semi-minor axis to semi-major axis, optical radius, and morphological type in the RC3 scheme.

inclinations, and the r_{83} values from panel (f) are used for estimating $W(r_{83})$. The last plot, panel (g), shows the morphological distribution of the galaxy sample.

In Figure A.1 (see the appendix), we plot the RCs folded about a kinematic center as described in Section 4.2. Entries in the figure are sorted first by the Right Ascension of each cluster, and within each cluster sample by increasing galaxy Right Ascension. The error bars include both the uncertainty in the wavelength calibration and the ORC fitting routine used. The name of the galaxy and its corresponding parent cluster are given along with the CMB radial velocity. Two dashed lines are drawn: the horizontal line indicates the adopted half velocity width, $W/2$, which in some cases arises from an extrapolation to the ORC or from a 21 cm width (see Table A.1); the vertical line is at r_{83}. Overlayed are the *PolyEx* fits used to infer $W(r_{83})$.

In addition to the 489 RCs presented here, we also have 21 cm measurements for 49 galaxies. All but two of these radio spectra were taken at the Arecibo Observatory using a spectrometer channel separation of 8 km s^{-1} while the remaining two were obtained at the Greenbank 300' telescope (Haynes & Giovanelli 1991) at a spectral resolution of 11 km s^{-1}. A typical signal to noise ratio for these observations was 10; errors in the observed velocity widths are of order 15 km s^{-1}. Details on the HI data reduction and the corrections made to the observed velocity widths can be found in G97a. A full discussion of the comparison between HI and optical widths, is given in G98b.

Figure 5.3 gives the "raw" TF plots of each cluster uncorrected for any cluster incompleteness bias. A computation of such bias is studied in the next chapter. In the A2877, A1736, A1983, and A2295 panels, the error bars containing filled circles represent members of "A2877b," "A1736b," "A1983b," and "A2295b," respectively. Included in the TF plots is the template relation obtained from nearby clusters in G97b:

$$y = -7.68x - 21.01 \tag{5.1}$$

where y is $M_{\rm cor}$ – 5log$h$ and x is log$W_{\rm cor}$ – 2.5.

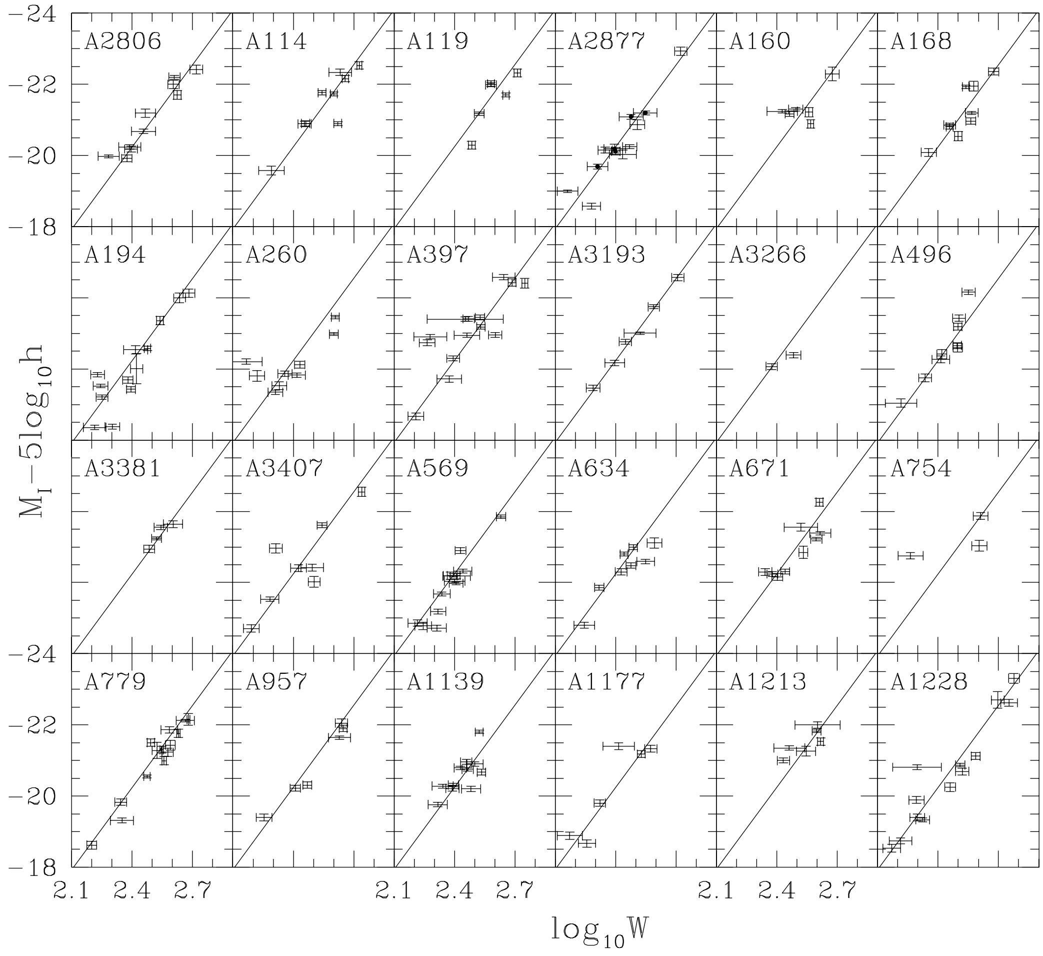

Figure 5.3 "Raw" TF plots for the clusters are given. We emphasize that the data have *not* yet been corrected for incompleteness bias. The dashed line is the template relation valid for low z clusters, Equation 5.1.

A final display of the data can be seen in Figure 5.4, a collection of all the data in a single TF plot. The solid line given is the same as that drawn in Figure 5.3. Evidence for non-linearity is tenuous.

Figure 5.3 (Continued)

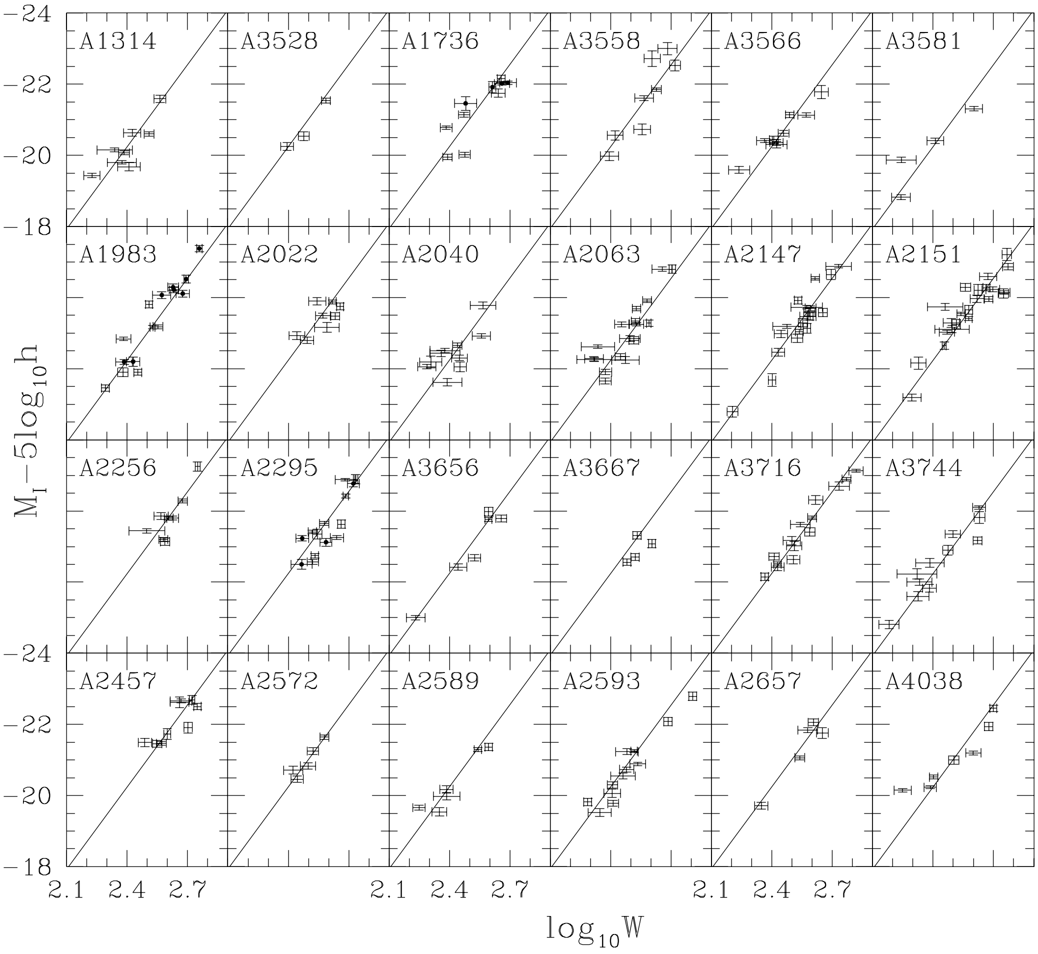

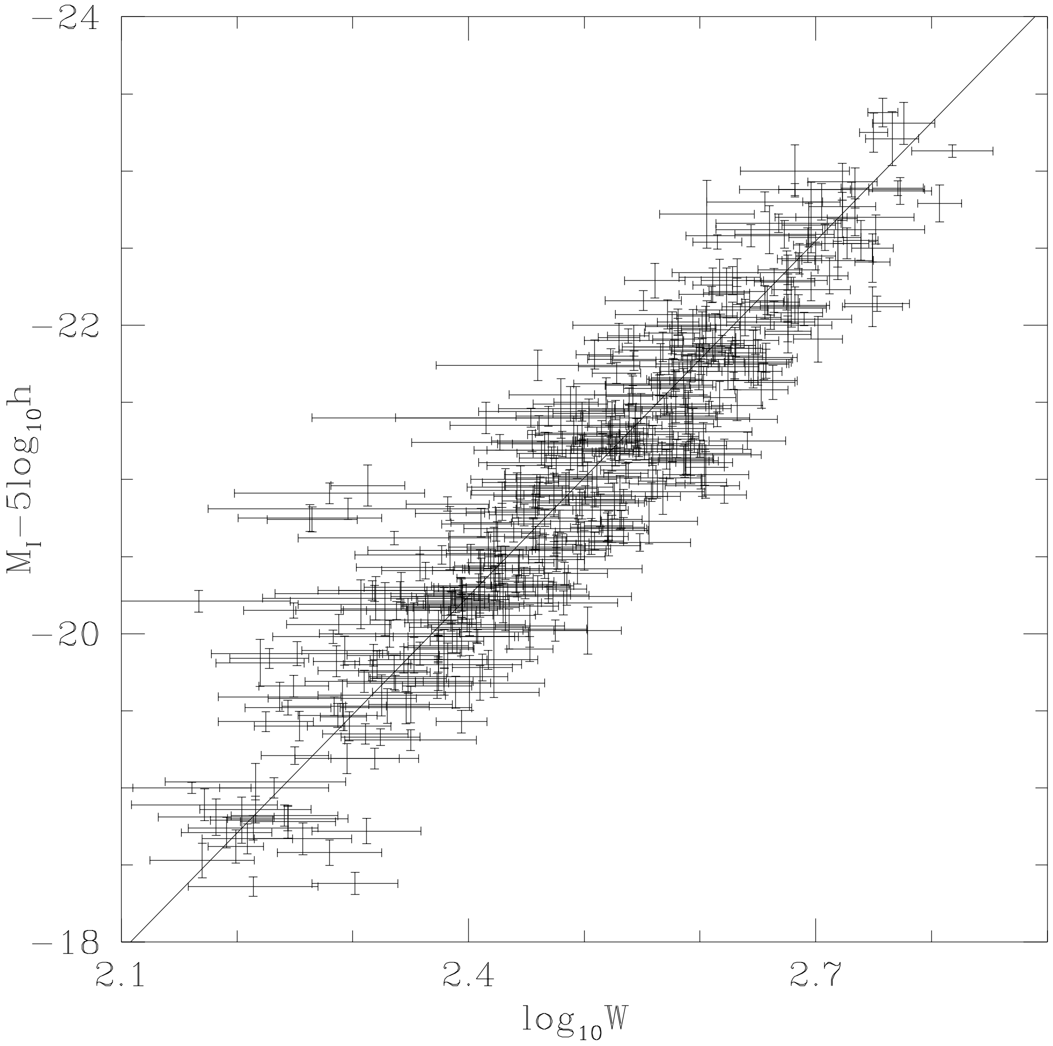

Figure 5.4 The TF data for all cluster members is displayed above. The linear relation plotted is that from G97b for the nearby cluster sample.

Chapter 6

The Tully-Fisher Relation

6.1 Introduction

In order to extract peculiar motions from a set of TF observations, the data must be referenced to a fiducial template. Ideally, the template employed represents the kinematical rest frame for the volume of space under consideration. It follows then that the template necessarily must originate from data within the volume itself, and that the template data likewise must spatially sample a large fraction of the volume. Otherwise, large-scale dynamical fields will be extrapolated from a template that is corrupted by small scale motions. In this chapter we outline our approach to the accurate calibration of the TF relation using our sample of data from 52 rich Abell clusters distributed throughout the sky. As we shall see, the ultimate tabulation of the TF offset is an iterative process: the computation of the cluster incompleteness bias requires prior knowledge of the TF template zero-point, or offset, while the computation of the offset demands a correction for the cluster incompleteness bias. The process does converge, however, in a small number of iterations. We choose to begin this chapter with a discussion in Section

6.2 of the scatter characteristics of our TF data. Section 6.3 covers pertinent biases in our observational work and our corrections for them. Finally, Section 6.4 presents results for the TF template along with the offsets for individual clusters, specifically those due to peculiar motions.

6.2 The Scatter of the Tully-Fisher Relation

We start this chapter with a discussion of the TF error budget. Essentially the accuracy of any observational work is understood through the amplitude of a relation's scatter. Whether or not the true scatter is observed may be open to debate, however, and the TF relation is no different in this regard. Claims of the scatter in the TF relation vary from as low as 0.10 mag (Bernstein *et al.* 1994) to as high as 0.7 mag (Sandage *et al.* 1994a,b; 1995; Marinoni *et al.* 1998). The amplitude of the scatter does depend on wavelength, and studies in the I band typically yield the tightest relations. The efforts with the largest samples yield one-sigma dispersion values of $\sim$0.4 mag (Mathewson, Ford, & Buckhorn 1994; Willick *et al.* 1995; G97). Uncertainties in observational measurements are not the only factors that lead to the overall spread in the data. The corrections to the observed fluxes and disk rotational velocities described in Chapters 3 and 4 are not exactly known, nor are the methods we detail later in this chapter to account for inherent sample biases such as cluster incompleteness. Moreover, there must be an *intrinsic* component to the TF dispersion since individual galaxies inevitably have diverse histories. In fact, Eisenstein & Loeb (1996) advocate an intrinsic scatter of 0.3 magnitudes, a number greater than most estimates from observational work. In light of this fact, they make the interesting claim that either spirals formed quite early or that there must be a type of feedback loop that promotes galactic assimilation.

Figure 6.1 reinforces the notion of low intrinsic scatter. The two dotted lines

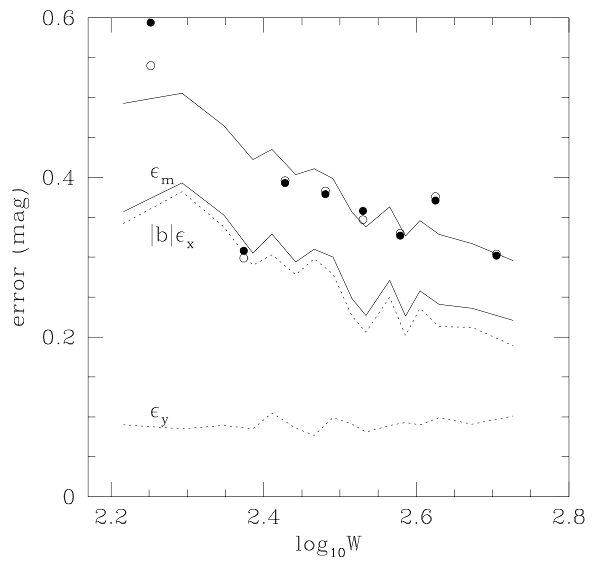

Figure 6.1 The observed scatter in the TF relation. Running averages (in units of magnitudes) of the observed errors are given as dotted lines. The lower solid line is the sum in quadrature of the two dotted lines and represents the total measurement uncertainty. The circles plotted indicate the standard deviations of residuals from the template TF relation, with filled circles taking into account cluster incompleteness; both filled and unfilled circles are corrected for all other effects including cluster peculiar motions. The upper solid line is the total scatter in the TF relation and has been computed by a sum in quadrature of the observed error distribution and an intrinsic component equivalent to that found in G97b (see Equation 6.2 below).

indicate the velocity width and magnitude errors (ϵ_x, Equation 4.26, and ϵ_y, Equation 3.5), with ϵ_x scaled by the TF slope to put it on the same magnitude scale; the solid line labeled ϵ_m represents the average measurement uncertainty: $\epsilon_m^2 = (b\epsilon_x)^2 + \epsilon_y^2$. The data displayed in Figure 6.1 are generated using equal numbers of galaxies per data point. The circles plotted represent the average standard deviations of the residuals from the fiducial TF relation. The filled circles include cluster incompleteness bias corrections (described in Section 6.3.1), while all circles are corrected for all other effects including morphological offsets and cluster peculiar motions. We see that the velocity width errors dominate those from the I band fluxes, which are approximately independent of velocity width. Furthermore, the errors on the logarithmic velocity widths become increasingly uncertain for slower rotators. We can understand this last property of the scatter by recalling the form of logarithmic errors: $\sigma_{\log_W} \propto \sigma_W/W$. Thus, since the errors on the W do not linearly scale with W, but instead remain rather flat, the logarithmic errors decrease with W. We approximate the total observed scatter with a simple linear relation that depends on the velocity width:

$$\sigma_{\mathrm{tot}} = -0.40x + 0.38 \text{ mag.} \tag{6.1}$$

The total scatter found here is in general larger than that found in G97b, an unsurprising fact given our use of optical rotation curves, a relatively less certain source, compared to 21 cm profiles, of velocity widths. The gap between the observed scatter and the measured errors is reconciled by the intrinsic scatter contribution: the top line is a sum in quadrature of our observed measurement errors, ϵ_m, and the intrinsic scatter found in G97b:

$$\sigma_{\mathrm{int}} = -0.28x + 0.26 \text{ mag.} \tag{6.2}$$

Simply put, our findings for an intrinsic component of the TF relation agree with those of G97b.

6.3 Observational Biases

6.3.1 Cluster Incompleteness

Quite possibly the most important selection effect to consider for this observing program is that of cluster incompleteness, the preferential sampling of the bright end of the luminosity function (LF). The condition unmistakably will occur when source imaging does not extend to adequately low surface brightness levels, thus precluding inclusion of faint galaxies in the sample. On the other hand, the effect can arise regardless of the source image quality and may be a result of observer indolence – brighter galaxies are favored since their RCs can typically be adequately mapped with shorter integrations. Several authors have cautioned that cluster incompleteness can significantly alter inferred distances to clusters, though this ultimately depends on the amplitude of the scatter in the TF relation (see the review by Teerikorpi 1997 and references therein). Schechter (1980) first advanced the notion that the repercussions of this selection effect can be circumvented through an inverse fitting procedure, whereby the roles of the ordinate and abscissa in the TF diagram are reversed. The argument goes as follows: if there are no observational effects working against the selection of velocity widths and if the errors on the absolute magnitudes are negligible, then a fit to log$W$ vs. M will not be affected by a cutoff at faint magnitudes. However, as G97 points out, magnitude errors cannot be ignored (see Figure 6.1), negating such a circumvention. In addition, the errors in M and log$W$ are coupled, through inclination corrections.; TF data do not obey a sharp faint magnitude limit. Inevitably, the absence of faint galaxies in a TF sample artificially brightens the offset and lowers the slope. We describe next our methodology to account for the effect.

Our first concern is to quantify the characteristics of the observed LF with respect to the actual LF. As an aside, we note that current work by Andreon (1998) supports the notion of a canonical spiral LF by proposing that the LF for the separate morphological classes E, S0, and S is *independent of environment* – observed differences in the overall LF for different environments are merely due to varying proportions of the morphological classes. Our first step is to sum up the observed luminosities in bins of absolute magnitude. Computing such absolute magnitude histograms for each individual cluster, where the membership counts can be as small as ~5, would not be statistically indicative on the whole. We therefore compute *average* histograms for several distance ranges of width 2000 km s^{-1}. We define the completeness function as the ratio of the observed luminosity distribution to the assumed intrinsic luminosity distribution. The following figures have been constructed assuming a Schechter LF with $M^* = -21.6$ and $\alpha = -0.5$, but final TF templates using other Schechter parameters will also be provided in Section 6.4. Figure 6.2 displays a smoothed representation of the completeness functions, along with our fitted approximation. We borrow a relation from Fermi-Dirac statistics to model our completeness:

$$c(y) = \frac{1}{e^{(y-y_{\rm t})/\beta} + 1} \tag{6.3}$$

where $y_{\rm t}$ represents a transition luminosity in the fit, and β characterizes the steepness of the drop. It should be noted that the final TF template is rather robust in terms of the completeness function construction. The template is largely insensitive to the choice of distance regimes, variations in the FD fit profile, and the luminosity bin widths. Reasonable alterations in these parameters induce

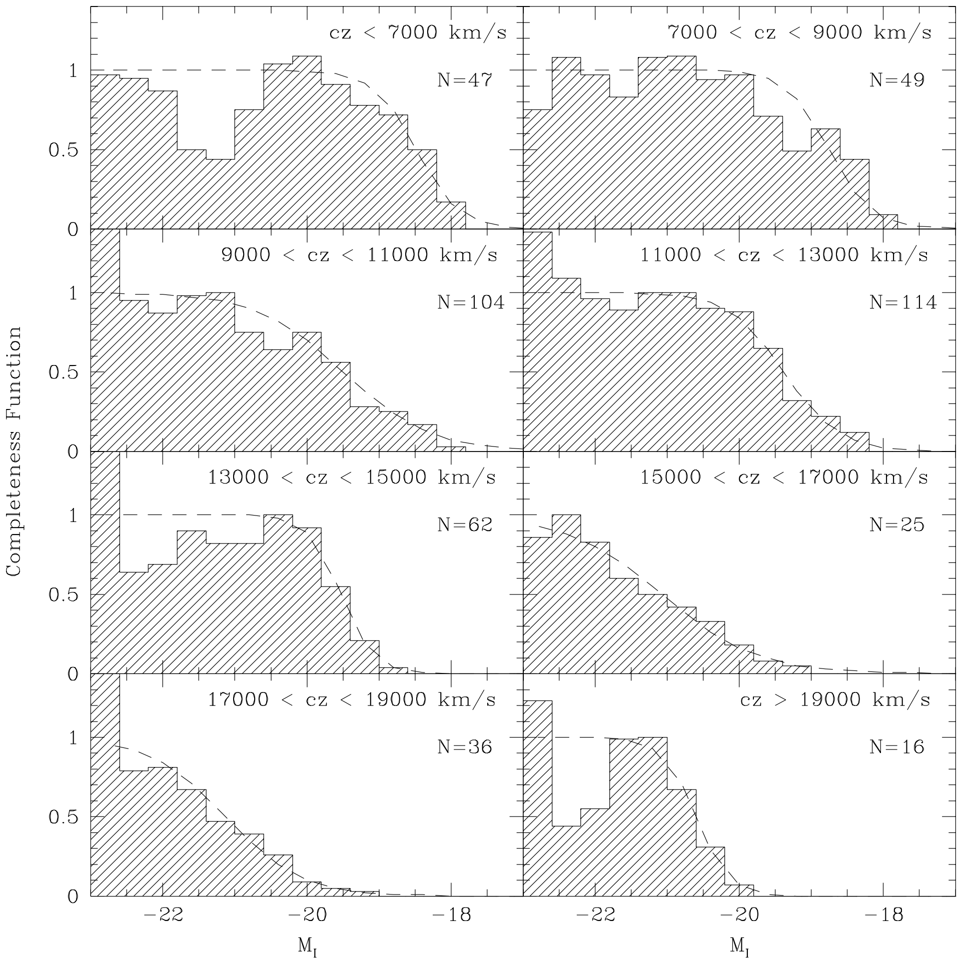

Figure 6.2 The distributions of cluster completeness for separate distance ranges. The dashed line is our smoothed approximation to the completeness function. The number of galaxies within each redshift range are indicated.

negligible changes in the TF template offset. With the estimation of the completeness function in hand, we can now quantify a given cluster's incompleteness bias via Monte Carlo simulations.

Monte Carlo Simulations of Cluster Parent Samples

For each cluster, the fitting of a TF relation to a sample of observed velocity widths and luminosities is biased by the absence of faint galaxies. Our task is simplified by assuming the bias-corrected slope derived in G97b is valid for our sample, a justifiable assumption given the relative propinquity of their data – a broader dynamic range can be more easily sampled in nearby clusters. Furthermore, least-square fits to the data yield slopes that, within the errors, agree with G97b. On a more qualitative level, inspection of Figure 5.4 indicates our data agree with the slope from G97b. It is thus sufficient to only determine the bias in the TF offset for each cluster. The essence of our approach is to use, for each cluster, the observed error distribution as a guide to build a parent cluster sample from which our observed biased sample derives, and to extract from this parent sample the "true," or unbiased, TF offset.

The technique is as follows: for each galaxy a large number ($N = 10^3$) of trial TF data points are generated that mimic the general characteristics of the actual data. Within each trial, a random (Gaussian deviate) magnitude offset $\Delta y_{\rm trial}$ is first chosen according to the scatter relation found in Section 6.2, Equation 6.1, which depends on the galaxy's measured velocity width parameter x. The addition of this offset to the magnitude inferred from the final, template TF relation yields the trial absolute magnitude:

$$y_{\rm trial} = b_{\rm tf}x + a_{\rm tf} + \Delta y_{\rm trial}. \qquad (6.4)$$

The trial magnitude is kept only if it is a likely magnitude, i.e. a second random number from the interval [0,1] must be less than $c(y_{\rm trial})$, the completeness value for the trial luminosity. Otherwise, the process is repeated until a likely magnitude is found. After all N iterations are complete for a given galaxy, the incompleteness bias is taken to be the mean difference between the trial luminosities and that expected from the TF relation, i.e.

$$-\Delta y_{\rm icb} = \frac{\sum_i^N y_{{\rm trial},i}}{N} - (b_{\rm tf}x + a_{\rm tf}). \qquad (6.5)$$

Figure 6.3 gives the biases calculated as a function of velocity width and the polynomials we fit to them. The general property of the computed bias is as

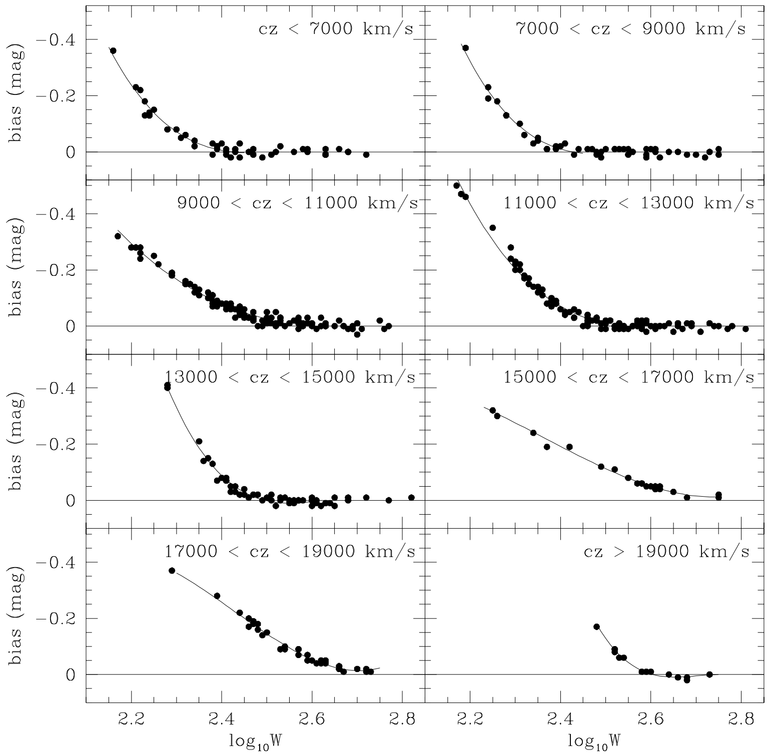

Figure 6.3 The incompleteness bias as a function of rotational velocity width is shown. Individual points are the biases generated for each galaxy from Monte Carlo simulations and the solid lines are polynomial fits to the bias.

expected: incompleteness biases "turn on" at higher velocity widths (i.e. for brighter galaxies) for more distant objects. The bias is larger (i.e. more negative) than −0.2 magnitudes for about 5% of the sample. An incompleteness bias-corrected offset for each cluster is then extracted from the cluster's distribution of observed velocity widths and bias-corrected absolute magnitudes. A tabulation of these offsets is provided in Table 6.1. The cluster names are listed first and are followed by the number of cluster members with reliable photometry and velocity widths. The next two columns are measures of the cluster offsets, the second of which is corrected for the effect of cluster incompleteness and includes an indication of its uncertainty ϵ_a in parentheses, e.g. $-21.01(10)$ implies -21.01 ± 0.10 magnitudes. The last column of data listed is σ_a, the one-sigma dispersion in the difference between the template and the cluster's set of absolute magnitudes. It is used to compute the offset uncertainty: $\epsilon_a = \sigma_{\rm min}/\sqrt{N}$, where $\sigma_{\rm min}$ is taken to be the minimum of [0.35 mag, σ_a] to avoid overly optimistic measures of offset uncertainty in cases of accidental alignment of the data due to small number statistics. Lastly, we remark that the proper incorporation of selection effect corrections is vital to determining the TF template, but the exact evaluation of said biases necessarily requires a TF template. A stable solution to this circular process is found within a few iterations.

6.3.2 Homogeneous Malmquist Bias

An observational bias commonly referred to as the "homogeneous Malmquist bias" is a distance underestimate for a galaxy drawn from a uniform distribution of galaxies. The bias is a direct result of the error on the measured distance – a galaxy taken from a Poissonian spatial distribution and measured to be at a distance $R_{\rm m} \pm \Delta R$ is more likely to actually lie between $R_{\rm m} + \Delta R$ than in the range $R_{\rm m} - \Delta R$, merely due to the larger volume of the more distant shell. Following the reasoning given in Lynden-Bell *et al.* (1988), it can be shown that a measured distance $R_{\rm m}$ is, on average, an overrepresentation of the true distance $R_\circ$ by the factor $\exp(3.5\Delta^2)$, where Δ is the fractional error in the TF distance measurement, roughly 17% for individual galaxies and 5% for clusters:

$$R_\circ = R_{\rm m} e^{3.5\Delta^2}. \tag{6.6}$$

Table 6.1 Cluster Tully-Fisher Offsets

Cluster	N	$a_{\rm bias}$	a	σ_a	Cluster	N	$a_{\rm bias}$	a	σ_a
A2806	10	-21.06	-21.04(11)	0.27	A3528	3	-20.87	-20.73(07)	0.12
A 114	9	-20.91	-20.83(14)	0.41	A1736	6	-20.93	-20.90(18)	0.44
A 119	6	-20.86	-20.86(16)	0.38	A1736b	4	-20.94	-20.93(18)	0.32
A2877	7	-20.92	-20.87(15)	0.40	A3558	8	-21.03	-21.01(15)	0.43
A2877b	5	-21.00	-20.98(16)	0.14	A3566	9	-21.04	-20.94(12)	0.23
A 160	6	-20.97	-20.96(18)	0.45	A3581	4	-20.92	-20.86(20)	0.40
A 168	9	-21.04	-21.02(13)	0.38	A1983b	8	-21.18	-21.16(12)	0.25
A 194	13	-20.86	-20.81(13)	0.45	A1983	7	-21.05	-20.97(19)	0.50
A 260	9	-20.77	-20.68(14)	0.42	A2022	8	-20.84	-20.77(12)	0.32
A 397	14	-21.07	-21.03(15)	0.57	A2040	10	-21.01	-20.94(14)	0.43
A3193	6	-21.05	-21.00(14)	0.09	A2063	18	-21.08	-21.05(09)	0.36
A3266	2	-20.78	-20.60(25)	0.21	A2147	19	-20.99	-20.97(09)	0.39
A 496	9	-21.08	-21.03(12)	0.36	A2151	22	-20.99	-20.97(08)	0.40
A3381	4	-21.07	-21.06(18)	0.12	A2256	8	-20.95	-20.91(12)	0.33
A3407	8	-20.97	-20.88(21)	0.58	A2295b	4	-20.95	-20.86(18)	0.36
A 569	13	-20.88	-20.85(10)	0.30	A2295	10	-20.83	-20.81(12)	0.39
A 634	8	-20.87	-20.85(12)	0.35	A3656	6	-20.90	-20.88(14)	0.28
A 671	9	-20.95	-20.89(12)	0.34	A3667	4	-20.63	-20.54(18)	0.28
A 754	3	-20.98	-20.89(42)	0.73	A3716	14	-20.99	-20.96(09)	0.22
A 779	14	-20.90	-20.88(09)	0.27	A3744	11	-20.94	-20.88(11)	0.37
A 957	6	-20.83	-20.77(14)	0.16	A2457	9	-20.93	-20.89(12)	0.32
A1139	11	-21.08	-21.03(12)	0.39	A2572	5	-21.02	-20.99(16)	0.13
A1177	6	-21.01	-20.92(15)	0.37	A2589	6	-20.94	-20.87(14)	0.23
A1213	6	-21.03	-21.02(14)	0.33	A2593	12	-20.82	-20.77(10)	0.30
A1228	13	-20.87	-20.79(10)	0.33	A2657	5	-20.93	-20.91(16)	0.26
A1314	8	-20.94	-20.88(12)	0.31	A4038	7	-20.96	-20.92(13)	0.35

The Abell/ACO clusters do not represent a homogeneously distributed population. Thus, the application of a homogeneous Malmquist bias correction may appear incorrect. However, a correction that takes into account the clustering properties of clusters differs from the homogeneous Malmquist bias correction only in the second order. Given the miniscule size of the correction and the uncertainty of a possible "inhomogeneous" Malmquist bias correction, we consider the application of a homogeneous Malmquist bias correction a satisfactory approach. It was shown in G97b that such a correction for clusters of galaxies is rather small, almost to the point of being negligible (of order 1% on individual cluster distances). This is due to reduced fractional distance errors for systems with N estimates of the distance: $\Delta = 10^{0.2\sigma/\sqrt{N}} - 1$, where σ is the TF scatter for the system. However, the SCI cluster sample is considerably closer, and the membership counts for their clusters are more enhanced than for the SCII clusters. The result is that this correction may have more impact on our work. The influence of the homogeneous Malmquist bias on cluster peculiar velocities will be discussed in Chapter 7 when cluster peculiar velocities and distances are derived.

6.3.3 Cluster Size

In calculating absolute magnitudes, we assume that each cluster member within one Abell radius of the cluster center is at a distance equal to the average of all the redshifts available for the cluster from the literature. It is unlikely that a given galaxy will actually be at this distance, but it is a useful approximation if the distance to the cluster is significantly larger than the cluster's virial size, i.e. the velocity dispersion is much less than the redshift. For all but a handful of our clusters this is the case, so cluster size biases play a small role in our analysis.

Our concern here is the method of averaging used. The calculation of a cluster offset involves averaging over absolute magnitudes. Thus, averages of the logarithms of the distances are computed, when the logarithm of the average distance is actually desired. This results in a systematic underestimate of cluster distances. We can use either the angular distribution on the sky of the cluster galaxies or the Abell radius to infer the approximate physical size of the each cluster. Simple analytic calculations using either estimate of the cluster size show that the amplitude of the bias is at most of order 0.001 magnitudes for even our closest clusters, so we shall not concern ourselves with this effect any further. A more serious concern, the morphological dependence on the TF relation, is investigated next.

6.3.4 Morphology

Ideally, scientific models are simple and are thus constructed with the fewest number of free parameters the data demand. In TF work, it would be preferable to limit the range of morphologies sampled, since physical parameters are known to vary along the Hubble sequence (Roberts & Haynes 1994). For example, it has been shown that, for a given (optical) luminosity distribution, the velocity width distribution for early-type galaxies is shifted to higher rotational speeds with respect to the distribution for later types (Roberts 1978). There is evidence, however, that the TF differences between morphological types appear to diminish at wavelengths longer than I band (e.g. Aaronson & Mould 1983). Regardless, we are fortunate that one sample selection criterion of ours, that of disks being rich in ionized gas, encouraged a rather homogeneous sample comprised mainly of Sc types (see figure 5.2). Our sample has the following population properties: 14% are of type earlier than Sb, 16% are type Sb, and 70% are classified as Sbc or later. The majority (52%) of the galaxies are type Sc.

One luxury of our large sample is that it affords statistically significant tests of TF morphological dependencies. We plot in Figure 6.4 the TF parameters with symbols differentiated according to morphological class. Filled circles symbolize

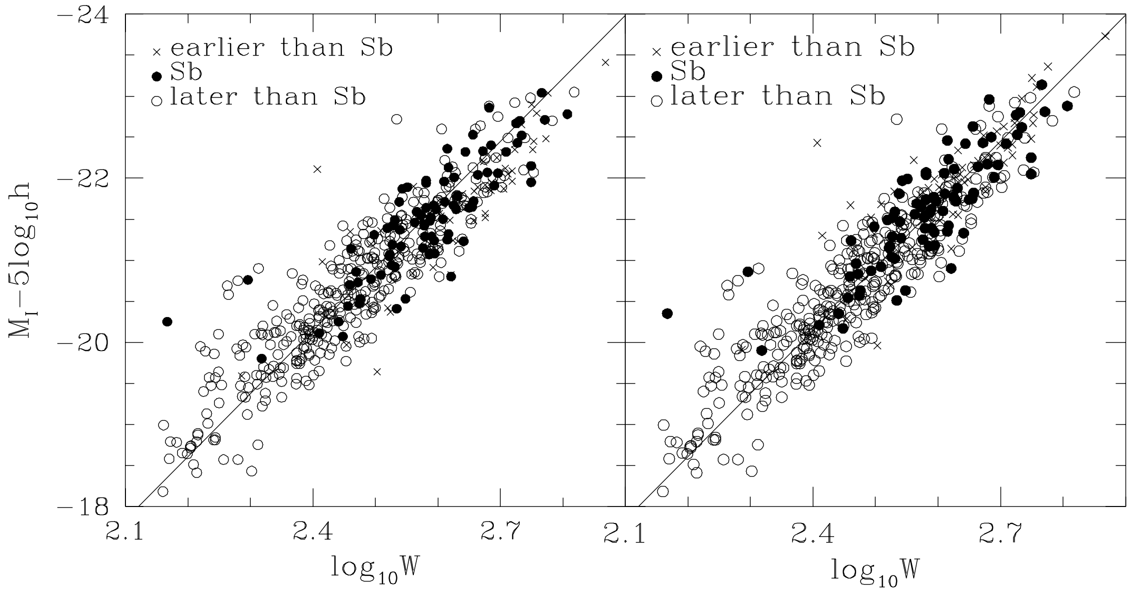

Figure 6.4 The TF diagram differentiated according to morphological class. Asterisks represent galaxies earlier than Sb, filled circles symbolize type Sb, and open circles are for Sbc and later. The data have been corrected for all the effects discussed in Chapters 3 and 4 and also for cluster peculiar motions.

Sb types, whereas open circles and asterisks represent types later and earlier than Sb, respectively. The plot includes the data for all galaxies deemed to have reliable velocity widths, with each cluster member corrected for cluster peculiar motion. The solid line drawn uses the fiducial TF slope of -7.68, a figure derived in G97b and assumed throughout this work. As found in G97b, a clear distinction is evident between the three Hubble types in the form of a fainter offset for earlier types. The error-weighted averages of the offsets Δm_T for the three morphological classes differ in the following ways for our sample:

Types earlier than Sb: -0.23 (-0.32) mag

Type Sb: -0.11 (-0.10) mag

Other types: unchanged

The numbers given in parentheses are those from G97b. Since similar trends are seen with this data set and that of G97b, we will continue to utilize the offsets obtained in G97b for consistency.

6.3.5 Environment

Yet another possible bias in our sample is the effect of environment. For instance, the more distant clusters in our sample (and the Abell/ACO catalog in general) tend to be richer. A richer cluster typically has a stronger intracluster medium X-ray flux and a more regular, elliptical-dominated core (see, for example, Sarazin 1986). We note that spiral galaxies predominantly lie in a rich cluster's periphery and that the further a spiral disk is from the cluster center, the more likely it is to contain neutral hydrogen gas (Giovanelli & Haynes 1985). This lack of interstellar gas within clusters of galaxies may be due to evaporation into the hotter intracluster gas, or it may attributed to "stripping" originating from either tidal galaxy–galaxy interactions or ram pressure ablation on intracluster gas. Rubin, Ford, & Whitmore (1988) and Whitmore, Forbes, & Rubin (1988; WFR hereafter) claim that the inner spiral galaxies within clusters exhibit falling RCs, as opposed to the asymptotically flat or rising RCs usually seen in the cluster periphery and field. Furthermore, they find cluster RCs may be of lower amplitude than field RCs. They offer the explanation that the falling (and lower amplitude) RCs arise from mass loss — the inner galaxies have had their dark matter halos stripped — or that the cluster environment simply inhibits halo formation. A related finding by WFR is a monotonic increase in the mass to light ratio, with cluster radius, which they ascribe to the changing RC shape with cluster radius. This view has been contested, however, by Amram *et al.* (1993) and Vogt (1995) who find little evidence for any gradients in the outer portions of RCs. If RCs in the inner regions of rich clusters do indeed differ from RCs in other environments, the ramifications are significant. The dependence of the TF relation and/or its dispersion on environment are possible consequences. Finally, we point out that rich clusters represent high density peaks and may thus be home to a recent merger; at least one third of all rich clusters are home to a recent inhomogeneous superposition of two or more separate systems (Girardi *et al.* 1997). The implications of frequent mergers on TF work is unclear, but in any event, it is prudent to verify whether environment plays a significant role in our data.

Figure 6.5 displays one such test of environmental bias. For each cluster member we have plotted residuals from the TF relation as a function of projected distance from the nominal cluster center. Panel (a) displays the data for all cluster members, while panels (b) and (c) differentiate between Abell cluster richness. All data are corrected for peculiar velocity and morphological offsets. We see no apparent trend with projected cluster radius in any of the panels. This is in agreement with the work of Biviano *et al.* (1990) and G97, which showed no change in the TF relation for different environments. We consequently do not consider environmental bias to be a serious concern with our data.

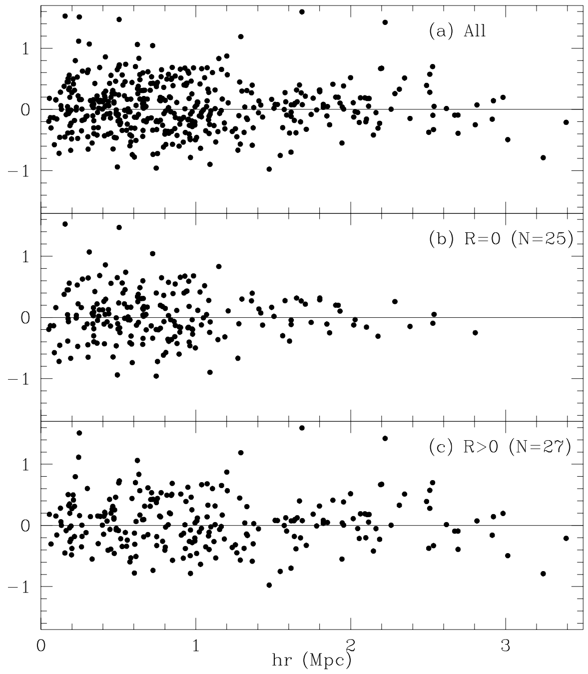

Figure 6.5 A test of environmental bias is displayed. TF residuals are given versus projected physical distance from the cluster center. The data are corrected for peculiar velocity and morphological offsets. Panel (a) displays all the cluster data, whereas panels (b) and (c) differentiate between cluster richness.

6.4 Results

6.4.1 Template Fitting Procedures

Let a_k be the TF offset for cluster k and $\Delta y_{\rm pec} = a_k - a_{\rm tf}$ be the shift due to the cluster's peculiar motion. The $i^{\rm th}$ cluster member's absolute magnitude can then be expressed as

$$y_i = y_{{\rm cor},i} - \Delta y_{\rm icb,i} - \Delta y_{\rm pec} \tag{6.7}$$

where $\Delta y_{\rm icb}$ is the cluster's incompleteness bias correction described in Section 6.3.1 and $y_{{\rm cor},i} = m_{\rm cor} - 5\log_{10}({\rm c}z_{\rm clus}/100) - 25$, $m_{\rm cor}$ being the corrected apparent magnitude given by Equation 3.3 and ${\rm c}z_{\rm clus}$ is the cluster systemic recessional velocity in units of km s^{-1}. We compute the $k^{\rm th}$ cluster's offset by averaging the individual cluster members, i.e.

$$a_k = \frac{\sum_i^{N_k}(y_i - bx_i)/\epsilon_i^2}{\sum_i^{N_k} 1/\epsilon_i^2}, \quad \epsilon_i^2 = (\epsilon_{x,i}b)^2 + \epsilon_{y,i}^2 + \epsilon_{\rm int}^2 \tag{6.8}$$

with N_k representing the number of cluster members in the $k^{\rm th}$ cluster. The uncertainty of the above offset computation is represented by

$$\epsilon_k = \frac{\sum_i^{N_k}(y_i - bx_i)^2/\epsilon_i^2}{\sum_i^{N_k} 1/\epsilon_i^2}. \tag{6.9}$$

The calculation of the template offset follows. It can be found in various ways, namely

$$a_{\rm tf} = \frac{\sum_k N_k a_k}{\sum_k N_k} \quad \text{or} \quad \frac{\sum_k a_k/\epsilon_k^2}{\sum_k 1/\epsilon_k^2} \quad \text{or} \quad \frac{\sum_i^N (y_i - bx_i)/\epsilon_i^2}{\sum_i^N 1/\epsilon_i^2}. \tag{6.10}$$

The first two computations are averages over the individual cluster offsets, weighted either by the number of cluster members or by the cluster offset uncertainties. The third calculation is a simple average over all N cluster galaxies, with each galaxy weighted by its total uncertainty. All of these methods give a global offset that agrees within the estimated errors (0.02 magnitudes); we shall hereafter quote results from the third computation. We point out that this definition of the TF offset implies that our sample as a whole approximates rest. This fact played a guiding role in our cluster sample selection: to approximate rest we needed a relatively distant, all-sky survey. Note that even in the presence of a large dipole, our calculation should adequately recover the rest frame, provided the data quality in our sample is not drastically inhomogeneous.

6.4.2 The Template and its Residuals

Table 6.2 lists results for several subsets of the data and for two different Shecter LFs: $\alpha = -0.50, M^* = -21.6$ and $\alpha = -0.75, M^* = -22.0$. A few fit parameters are listed, including the number of galaxies used, the TF offset and its associated uncertainty, an estimate of the scatter, and chi squared divided by the number of degrees of freedom. Notice that the dispersion and the offset error remain relatively unchanged across all subsets. The fact that the offset differs slightly for late and early type galaxies is somewhat expected – we saw earlier that the morphological type correction of -0.32 magnitudes advocated in G97 for Sa and Sab galaxies is possibly too large for our sample by a tenth of a magnitude. We should also point out that the slightly brighter offset seen for objects beyond 10,000 km s^{-1} works against recent claims by Tammann (1998) and Zehavi (1998) that the Hubble constant is higher within $\sim$10,000 km s^{-1} than it is beyond this distance. For our purposes, a fractional decrease of ϵ_H in $H_\circ$ beyond 10,000 km s^{-1} would yield an offset that is brighter by $\epsilon_H 5 \log_{10} e$, or 0.04 mags for $\epsilon_H = 0.02$.

Residuals from the template relation are plotted in Figure 6.6 as a function of several different parameters. A slight trend is seen in the residuals with axial ratio, in the sense that more inclined galaxies are more likely to lie above the template. Most likely this implies a too conservative approach to measuring disk ellipticities; corrections for the seeing-induced circularization of the isophotes are too small for more edge-on galaxies. This could impact not only inclination-based deprojections of velocity widths and internal extinction corrections, but it may as well influence corrections for slit smearing effects. An alternative explanation for the residual trend is a systematic variation in how we measure inclination as a function of inclination; the ellipticities of the more inclined galaxies may be underestimated, for example. In any event, the trend is slight and may in fact only

Table 6.2 Template Fit Parameters

Sample	N	a	ϵ_a	σ_a	χ^2/dof
no incompleteness bias	441	-20.96	0.02	0.39	1.1
$\alpha_{\rm LF} = -0.50, M^* = -21.6$					
	441	-20.91	0.02	0.38	1.1
2.5σ clip	425	-20.91	0.02	0.34	0.9
$60° < i < 80°$	252	-20.91	0.02	0.38	1.2
$i > 45°$	429	-20.91	0.02	0.38	1.1
$W > 150, y < -18.5$	428	-20.92	0.02	0.37	1.1
$T \leq Sb$	139	-20.95	0.03	0.38	1.3
$T > Sb$	302	-20.89	0.02	0.37	1.0
c$z > 10,000$ km s^{-1}	325	-20.92	0.02	0.38	1.1
$N_{\rm mem} \geq 5$	413	-20.92	0.02	0.38	1.1
$\theta_{\rm proj}$ <1 $R_{\rm A}$	347	-20.91	0.02	0.39	1.1
$\|cz - cz_{\rm clus}\| < 1000$ km s^{-1}	368	-20.91	0.02	0.38	1.1
includ. foreground & background	510	-20.90	0.02	0.39	1.2
$\alpha_{\rm LF} = -0.75, M^* = -22.0$					
	441	-20.90	0.02	0.38	1.1
2.5σ clip	425	-20.90	0.02	0.34	0.9
$60° < i < 80°$	252	-20.90	0.02	0.38	1.2
$i > 45°$	429	-20.90	0.02	0.37	1.1
$W > 150, y < -18.5$	427	-20.91	0.02	0.37	1.1
$T \leq Sb$	139	-20.95	0.03	0.38	1.3
$T > Sb$	302	-20.88	0.02	0.37	0.9
c$z > 10,000$ km s^{-1}	325	-20.91	0.02	0.38	1.1
$N_{\rm mem} \geq 5$	413	-20.91	0.02	0.34	1.1
$\theta_{\rm proj}$ <1 $R_{\rm A}$	347	-20.90	0.02	0.38	1.1
$\|cz - cz_{\rm clus}\| < 1000$ km s^{-1}	368	-20.90	0.02	0.38	1.1
includ. foreground & background	510	-20.89	0.02	0.39	1.2

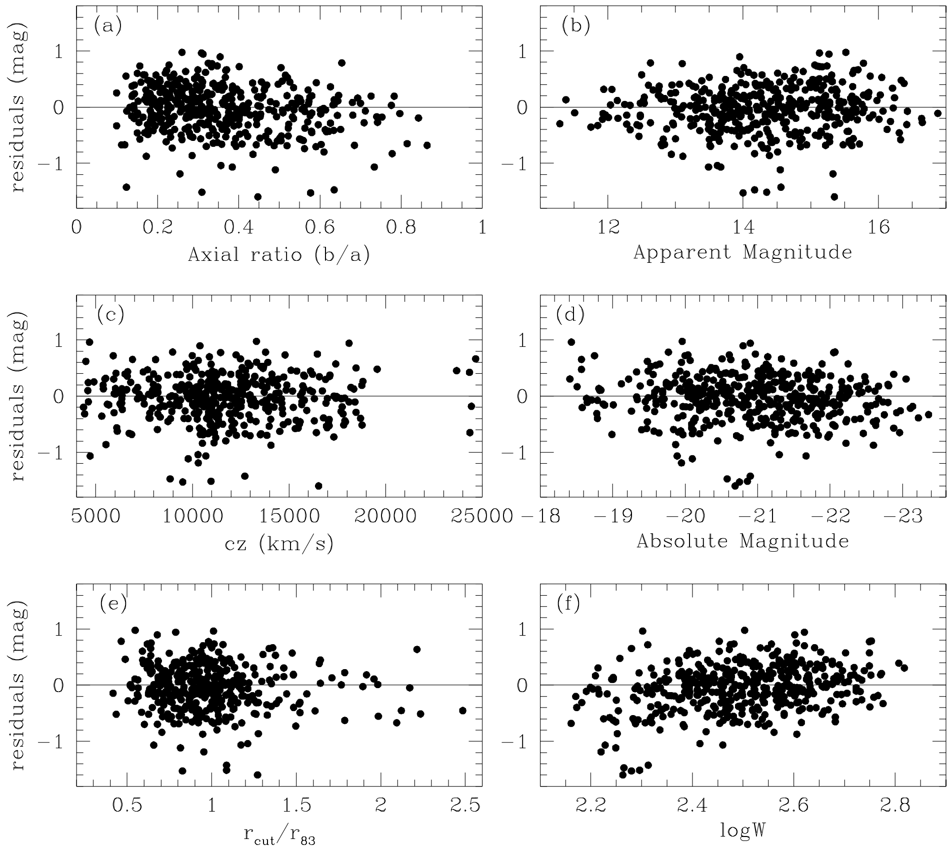

Figure 6.6 A sampling of residuals.

exist for the less reliable, face-on galaxies ($b/a \gtrsim 0.7$). The only other notable deviations from randomness in the residuals are the upturn/downturn trends for the low luminosity/rotational velocity galaxies in panels (d) and (f). This is expected since the fitting procedure did not minimize perpendicular distances to the template. Thus, it is inevitable that we see an "S"-shaped signature in the residuals for the ordinate and abscissa data.

We leave this section with the combined TF plot for all cluster galaxies in Figure 6.7. The plot is similar to that in Figure 5.4, except the data are corrected for both cluster incompleteness and cluster peculiar motion, in accordance with

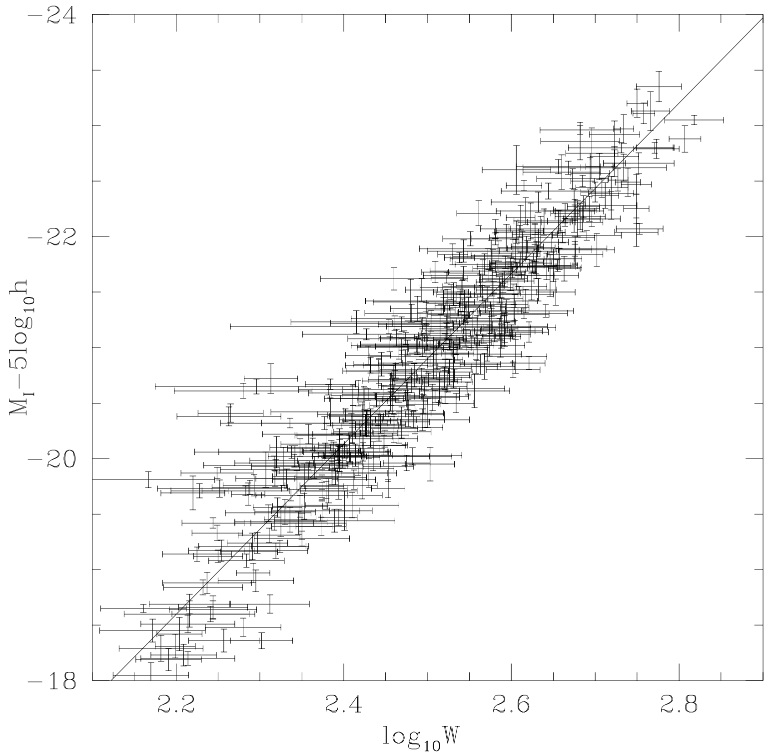

Figure 6.7 Plotted are the TF data for the member galaxies of all clusters. Each luminosity is corrected for cluster incompleteness and cluster peculiar velocity. The new TF template relation is drawn as a reference.

Equation 6.7. The new TF template is drawn as well:

$$y = -7.68x - 20.91. \tag{6.11}$$

Marginal evidence is now seen for a quadratic TF relation, most notably by the underluminous galaxies at slow rotation velocities. We caution the reader that this departure from linearity was not seen before correcting for cluster incompleteness. Furthermore, this correction has altered exactly this deviant subset the most; the slowest rotators have the largest incompleteness bias corrections. Rather than plunge ahead with a quantitative estimate of the template's apparent quadratic nature, we prefer instead to concentrate on the simplest model the data strongly warrant.

6.4.3 Results for Individual Clusters

The residuals given in Figure 6.8 are indicators of the quality of cluster membership assignment. A global version is provided in Figure 6.9 where we collapse

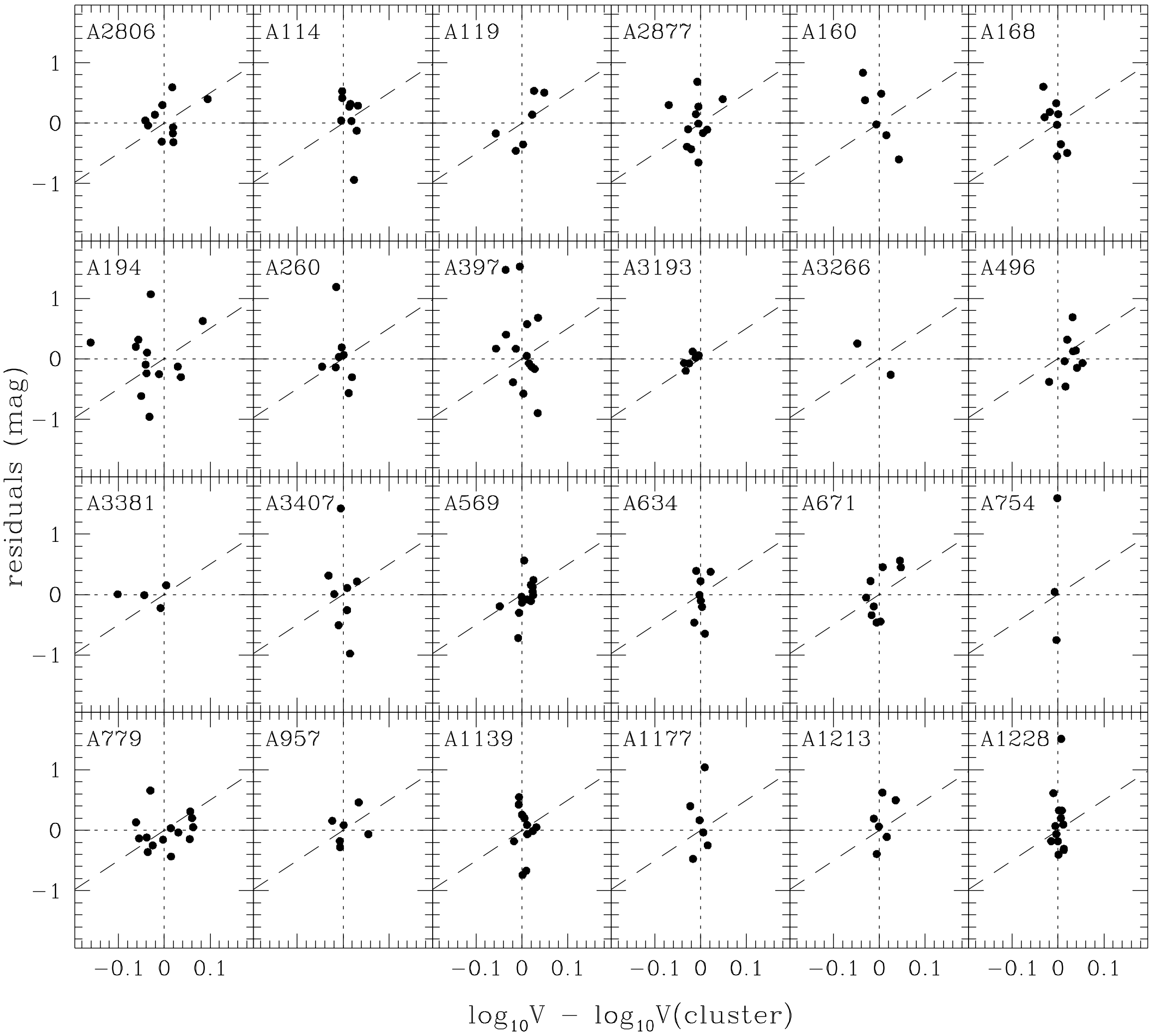

Figure 6.8 A test of cluster membership is displayed in the form of TF residuals as a function of separation from the cluster redshift. A line of slope 5 is given, the relation on which field galaxies incorrectly assumed to be cluster members should lie.

all the residuals for the sample into one plot. Since the abscissa is the difference between individual and cluster redshifts, residuals from field galaxies incorrectly

Figure 6.8 (Continued)

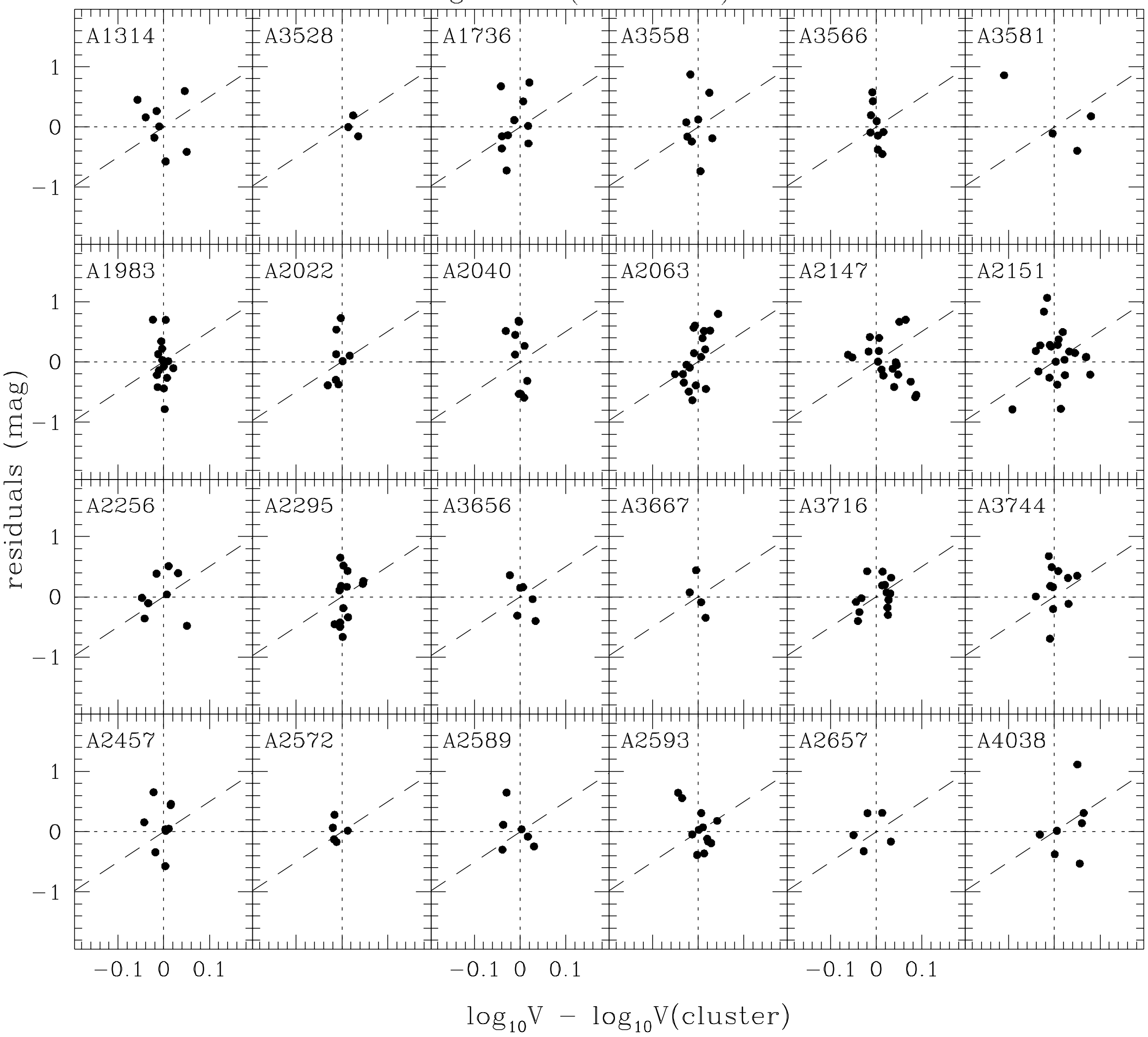

associated with a cluster should on average lie on the line of slope 5. There is no clear evidence for a significantly large subsample of improperly assigned memberships.

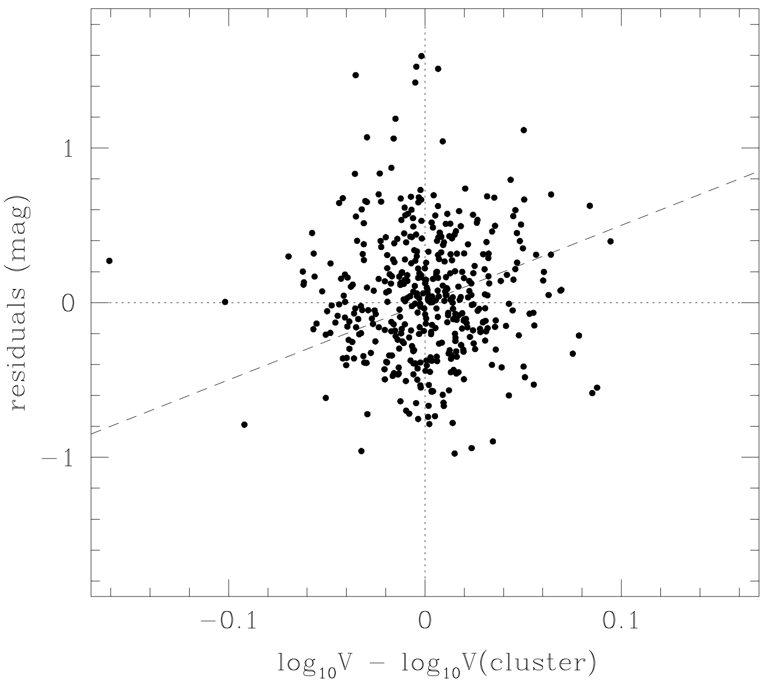

Figure 6.9 Similar to Figure 6.8, collapsed into one plot.

Chapter 7

The Bulk Flow of the Local Universe

7.1 Introduction

The motion of the Local Group of galaxies is imprecisely known. Typically, workers start from the inside and work their way out by using one vector that is known to great accuracy: the motion of the Sun in the CMB reference frame, most recently measured by COBE (Kogut *et al.* 1993). At that point further, less certain vectors must be incorporated to extract the Local Group motion. Estimates of the solar motion in the Local Standard of Rest, the Local Standard of Rest's rotation about the Galactic center, and the approximate trip the Milky Way is making within the Local Group all need to be made. The motion of the Local Group in the CMB reference frame has been estimated by several groups to be of order 600 km s^{-1} in the general direction of Galactic coordinates $(l, b) = (270°, 30°)$ (de Vaucouleurs *et al.* 1976; Yahil, Sandage, & Tammann 1977;

Lynden-Bell & Lahav 1988). We will use the result of Lynden-Bell & Lahav to convert heliocentric velocities to the Local Group frame by adding the vector $(-30, 297, -27)$ km s^{-1} in Galactic Cartesian coordinates. This result, coupled with the COBE result yields a Local Group velocity of $\mathbf{V}_{\rm lg-cmb} = 620 \pm 22$ km s^{-1} towards $(l, b) = (271°, 29°) \pm 3°$.

The Local Group motion can be considered, at least on a relatively small scale, a "bulk flow." In other words, the Local Group constituents move together as a whole. The volume over which this coherent motion persists is unknown. It can be estimated, however, by measuring the reflex motion, with respect to the Local Group, of spherical shells of increasing radii. The "convergence depth" is the distance at which the shells' dipole motions begin to mirror the Local Group motion in the CMB frame. An alternative interpretation is that the the shells at and beyond the convergence depth define a cosmic inertial rest frame. Accomplishing such a measurement ideally involves, for each shell, a large number of uniformly distributed objects with accurate peculiar motions. In this chapter we tackle the issue of the local convergence depth using accurate redshift-independent TF distances for the SCII sample of 52 Abell clusters of galaxies scattered about the sky with distances up to $\sim 200h^{-1}$ Mpc. To fortify our results, we also consider the SCI sample of G98 for which nearby cluster peculiar motions have been computed using a comparable TF kinematical offset. In the following section we present the peculiar velocities for the SCII clusters and summarize their global properties. Section 7.3 deals with dipole calculations of the cluster sample and Section 7.4 reviews tests of the dipole robustness using a variety of statistical techniques. We review and discuss our results in Section 7.5.

7.2 The Peculiar Velocity Sample

We interpret TF data found not to lie along the template relation as an indication of peculiar motion, with larger departures from the template implying larger amplitude peculiar velocities. Quantitatively, for a cluster at a redshift z with a zero-point offset ΔM from the TF template, we write the peculiar velocity as

$$V = cz(1 - 10^{0.2\Delta M}). \tag{7.1}$$

A 1σ confidence interval for the peculiar velocity can be extracted by inputting $\Delta M \pm \epsilon$, where ϵ is the error estimate for the cluster offset. We compute peculiar velocities and a measure of their errors for our SCII cluster sample and display the results in Table 7.1 and Figure 7.1, an Aitoff projection of Galactic coordinates. The symbols plotted in the figure reflect both the radial directions of the peculiar velocities and the strengths of the measurements – in the CMB reference frame, open (filled) circles represent approaching (receding) clusters and the circle size is inversely proportional to the accuracy of the measurement. A few cluster peculiar velocities, namely those for A3266 and A3667, are extremely large. We stress that these clusters, along with the few others that exhibit large velocities, are poorly sampled; as few as two or three data points are used to compute the motion. However, these large peculiar velocities are accordingly quite uncertain, with most being only 1σ results.

Our sample includes the central portions of various high density peaks and/or superclusters in the local Universe. It is significant to note that their motions are consistent with small departures from rest in the CMB frame, within the quoted error. For instance, the Shapley Supercluster, represented here by its

Table 7.1 Cluster Peculiar Velocities

Cluster	ΔM	$cz_{\rm hel}$	$cz_{\rm lg}$	$cz_{\rm cmb}$	$cz_{\rm tf,cmb}$	$V_{\rm cmb}$	Cluster	ΔM	$cz_{\rm hel}$	$cz_{\rm lg}$	$cz_{\rm cmb}$	$cz_{\rm tf,cmb}$	$V_{\rm cmb}$
A2806	-0.132(112)	8019	7918	7867	7403	464(0382)	A3528	0.179(203)	16458	16224	16770	18211	-1441(1703)
A114	0.072(136)	17436	17487	17144	17722	-578(1111)	A1736	0.010(179)	10397	10186	10690	10739	-49(0887)
A119	0.045(160)	13470	13607	13141	13416	-275(0988)	A1736b	-0.029(176)	13724	13513	14017	13831	186(1121)
A2877	0.032(150)	7165	7097	6974	7078	-104(0489)	A3558	-0.103(153)	14343	14122	14626	13948	678(0981)
A2877b	-0.075(157)	9231	9163	9040	8733	307(0634)	A3566	-0.033(118)	15370	15147	15636	15400	236(0837)
A160	-0.051(180)	12390	12577	12072	11792	280(0977)	A3581	0.042(197)	6865	6681	7122	7261	-139(0659)
A168	-0.116(127)	13365	13496	13049	12370	679(0725)	A1983b	-0.258(125)	11332	11340	11524	10233	1291(0589)
A194	0.091(125)	5343	5460	5037	5253	-216(0302)	A1983	-0.069(190)	13526	13537	13715	13286	429(1165)
A260	0.227(153)	10925	11135	10664	11839	-1175(0835)	A2022	0.137(125)	17262	17327	17412	18546	-1134(1067)
A397	-0.129(151)	9803	9916	9594	9041	553(0630)	A2040	-0.034(136)	13440	13429	13616	13404	212(0839)
A3193	-0.095(144)	10558	10381	10522	10072	450(0668)	A2063	-0.144(087)	10444	10448	10605	9925	680(0398)
A3266	0.307(248)	17774	17564	17782	20482	-2700(2345)	A2147	-0.063(090)	10493	10558	10588	10285	303(0427)
A496	-0.129(121)	9860	9779	9809	9243	566(0513)	A2151	-0.062(085)	11005	11079	11093	10781	312(0424)
A3381	-0.156(176)	11410	11196	11510	10712	798(0868)	A2256	-0.007(125)	17442	17673	17401	17345	56(0998)
A3407	0.030(205)	12714	12450	12861	13040	-179(1235)	A2295b	0.047(181)	18701	18945	18633	19041	-408(1587)
A569	0.056(099)	5927	5998	6011	6168	-157(0280)	A2295	0.099(122)	24622	24868	24554	25699	-1145(1448)
A634	0.060(125)	7822	7917	7922	8144	-222(0469)	A3656	0.028(144)	5750	5746	5586	5658	-72(0375)
A671	0.017(118)	15091	15046	15307	15427	-120(0838)	A3667	0.367(176)	16581	16491	16477	19511	-3034(1582)
A754	0.012(426)	16282	16052	16599	16691	-92(3294)	A3716	-0.058(095)	13764	13701	13618	13259	359(0581)
A779	0.030(095)	6967	6929	7211	7311	-100(0320)	A3744	0.029(111)	11386	11465	11123	11273	-150(0578)
A957	0.132(144)	13464	13261	13819	14685	-866(0974)	A2457	0.018(118)	17643	17845	17280	17424	-144(0946)
A1139	-0.127(119)	11851	11665	12216	11522	694(0629)	A2572	-0.084(157)	11857	12106	11495	11059	436(0803)
A1177	-0.011(149)	9755	9661	10079	10028	51(0689)	A2589	0.035(144)	12289	12531	11925	12119	-194(0804)
A1213	-0.116(144)	14006	13952	14304	13560	744(0899)	A2593	0.133(102)	12415	12651	12049	12810	-761(0605)
A1228	0.118(099)	10517	10489	10794	11397	-603(0517)	A2657	-0.006(157)	12028	12239	11662	11630	32(0844)
A1314	0.029(125)	9764	9815	9970	10104	-134(0582)	A4038	-0.017(134)	9012	9062	8713	8645	68(0534)

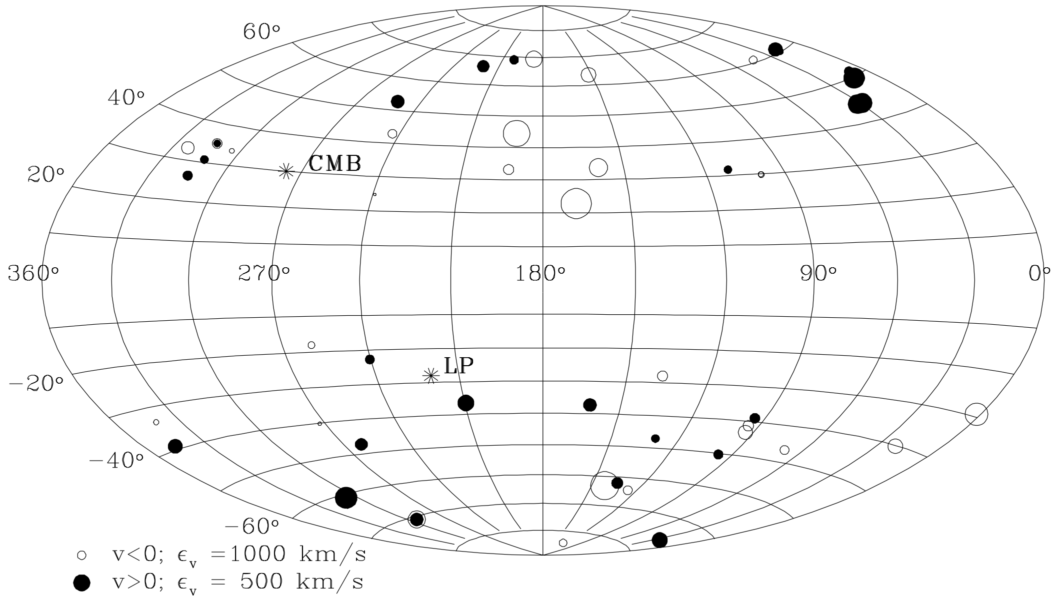

Figure 7.1 The all-sky distribution of the SCII peculiar velocity sample in Galactic coordinates. The symbol sizes are inversely proportional to the peculiar velocity uncertainties. The two examples in the lower left give the scale. Filled (open) circles refer to positive (negative) peculiar velocities in the CMB frame. Asterisks mark the apices of the motion of the Local Group with respect to the CMB and the LP cluster inertial frame.

core (A3558) and some peripheral members (A1736, A3528, and A3566), has an average CMB velocity of 118 ± 495 km s^{-1}. The Hercules region (A2147 and A2151) and the A2572/2589/2593/2657 supercluster are also slow movers, with average peculiar velocities of 307 ± 301 km s^{-1} and -222 ± 372 km s^{-1}, respectively. It is encouraging that the velocity fields centered on such massive systems, which one would expect to best represent "kinematic anchors," appear to be quiescent.

7.2.1 Homogeneous Malmquist Bias Corrections

As explained in Section 6.3.2, the homogeneous Malmquist bias in our sample tends to underestimate the distances to clusters. This in turn results in overestimated peculiar velocities. To correct for this effect we apply the factor $\exp(3.5\Delta^2)$ to the cluster distances inferred, where $\Delta = (10^{0.2\sigma/\sqrt{N}} - 1)$ is the fractional error in the distance measurement, σ the cluster TF dispersion, and N the number of cluster members with reliable TF data. In the language of Section 6.3.2,

$$V = cz - H_\circ R_\mathrm{m} \rightarrow cz - H_\circ R_\mathrm{m} e^{3.5\Delta^2}. \tag{7.2}$$

In practice we take the maximum of [0.35,σ] to be the cluster scatter to avoid chance alignments of cluster data. The inclusion of this correction factor in later computations changes results appreciably in very few of the cases discussed further below. As a result, only for those cases will we explicitly tabulate separate results that include homogeneous Malmquist bias corrections. We must remark, however, that it is not clear if this form of the correction is appropriate. It is likely that a more complicated, but harder to quantify, inhomogeneous bias correction is necessary. However, the variance between the inhomogeneous and the homogeneous forms of the correction is likely to be a second order effect.

7.2.2 The One-Dimensional Peculiar Velocity Distribution

It is useful to estimate the line-of-sight distribution of peculiar velocities since the parameter assists in delineating which cosmological models are probable (see, for example, Bahcall & Oh 1996). Our SCII cluster sample is relatively distant and the cluster membership counts are relatively anemic when compared to the SCI sample of G97. Consequently, our cluster peculiar velocities are much less certain and the overall distribution is significantly broadened by measurement errors. Figure 7.2 displays the peculiar velocity distribution for our sample. The peculiar velocities are represented by equal area Gaussians centered at the peculiar velocity with amplitudes scaled by the measurement uncertainty ($A_i \propto 1/\epsilon_i$) and dispersions equal to the estimated peculiar velocity errors. The thick dashed line superimposed on the plot is the sum of the individual Gaussians (its amplitude has been rescaled for plotting purposes). The 1σ dispersion in the observed

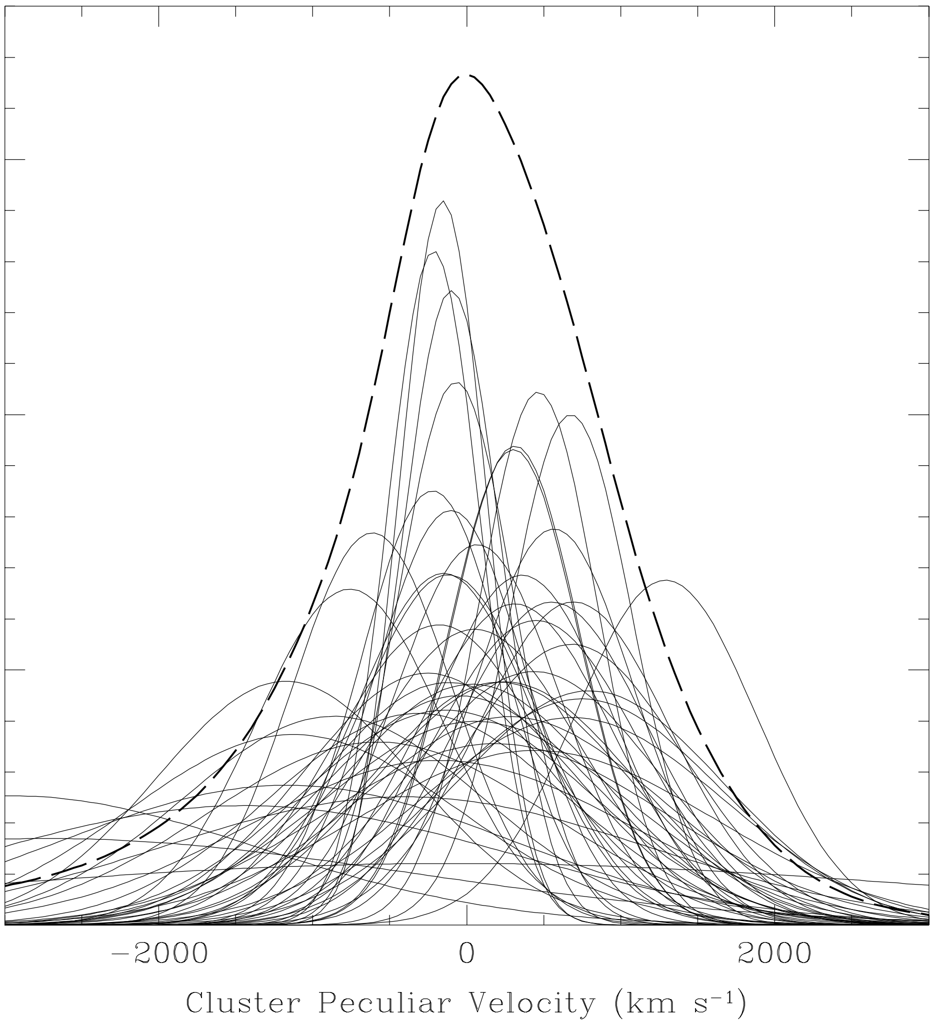

Figure 7.2 A display of equal area Gaussians representing the peculiar velocity sample. Each Gaussian is centered at the value of a cluster peculiar velocity, has a dispersion given by the uncertainty in the peculiar velocity measurement, and has an amplitude that is inversely proportional to the error. The sum of the Gaussian profiles is given by the thick dashed line.

distribution of peculiar velocities is found from a Gaussian fit to the dashed line: $\sigma_{\rm 1d,obs} = 796$ km s^{-1}. This value, however, is biased high by measurement errors. Deconvolving, or recovering an estimate of the true value, is performed through Monte Carlo work. We estimate the true peculiar velocity dispersion to be $\sigma_{\rm 1d} = 341 \pm 43$ km s^{-1}. The error estimate comes from a further Monte Carlo simulation: A simulated peculiar velocity sample is generated from random deviates of $A_i \exp[-(V - V_i)^2/2\epsilon_i^2]$. This is done for 10^3 simulated data sets, with each distribution fit by a Gaussian. The dispersion in the 1σ values characterizes the uncertainty in the rms peculiar velocity.

It is beyond the scope of this work to delve into how our value for $\sigma_{\rm 1d}$ constrains cosmological models, but we remark that our value lies between lower values that suggest a low density Universe, or small $\Omega_\circ$ models (G98a; Bahcall & Oh 1996; Borgani *et al.* 1997; Watkins 1998), and higher estimates that favor $\Omega_\circ = 1$ models (Bahcall, Gramann, & Cen 1994a; Croft & Efstathiou 1994).

7.2.3 A Test of the Zehavi Hubble Bubble

Utilizing peculiar velocities determined from Type Ia supernovae, current work by Zehavi *et al.* (1998) suggests a variable local Hubble constant. Specifically, they suggest that we appear to be residing at the center of a spherical volume of radius $\sim 70h^{-1}$ Mpc that is underdense by 20%, resulting in a local Hubble constant that is inflated by 6%. Furthermore, it seems that the Hubble constant then changes to being undervalued by a similar amplitude between 70 and $105h^{-1}$ Mpc, though this effect is not as strongly advocated by the authors. Our sample of 52 peculiar velocities, supplemented by the 24 SCI velocities, can provide a useful test of such a scenario. Zehavi *et al.* have 44 peculiar velocity measurements between 20 and $300h^{-1}$ Mpc, each distance accurate to ~6%. We have 76 cluster peculiar velocities (of accuracy ~4–6%) between 10 and $200h^{-1}$ Mpc, affording excellent coverage of the domains claimed to exhibit variable cosmic expansion rates. It should be noted that the cluster peculiar velocities for the SCI and the SCII samples derive from their own TF templates. However, the two templates use the same slope, and the offsets agree to within 0.01 magnitudes, well within the quoted errors.

Plotted in Figure 7.3 are the peculiar velocities, scaled by their distances, as a function of distance: $\delta H/H \equiv V/cz_{\rm tf,cmb}$ versus $cz_{\rm tf,cmb}$. The size of a dot

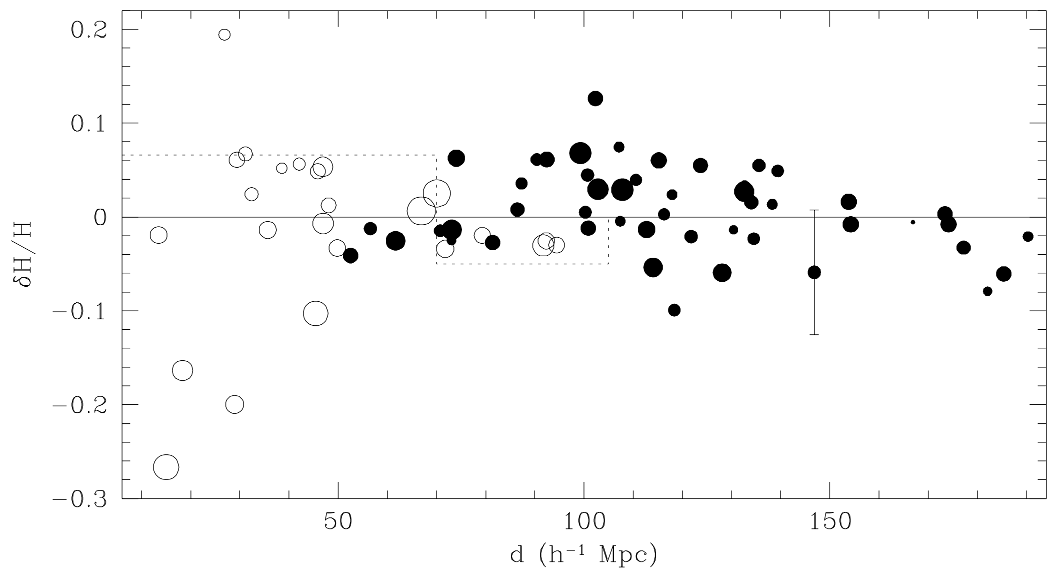

Figure 7.3 A test of the Zehavi Hubble bubble. The departures from smooth Hubble expansion are given as a function of distance. The sizes of the data points are proportional to the certainty of the peculiar motion; one set of error bars set the scale. Filled circles are from the SCII sample, open circles derive from the SCI data.

is inversely proportional to the error on the peculiar velocity; one set of error bars are given for scale reference. Included in the plot as dotted lines are the Zehavi *et al.* estimates for an accelerated expansion rate below $70h^{-1}$ Mpc, and a decelerated expansion rate between 70 and $105h^{-1}$ Mpc. Our points do not lie about these lines and hence do not support the purported Hubble bubble.

If the Hubble constant did not vary, we would expect the data to be evenly distributed about $\delta H/H = 0$ in the event the sample sky coverage is uniform. This is generally the case except for the data within $30h^{-1}$ Mpc, where the distribution of the six innermost clusters is skewed to southern declinations. Beyond this distance, however, and apart from the expected scatter in the data due to peculiar motions, the data point to a quiescent Hubble flow. Indeed, the 16 clusters between 30 and $70h^{-1}$ Mpc have an average $\delta H/H$ of 0.006 ± 0.011, and the 20 clusters in the range 70 to $105h^{-1}$ Mpc show only a 1.6% increase in $H_\circ$: $\langle \delta H/H \rangle = 0.016 \pm 0.010$. The average fractional change in the Hubble constant for all 70 clusters beyond $30h^{-1}$ Mpc is 0.000 ± 0.006. Our data do not only exclude the scenario put forth by Zehavi and collaborators, they also indicate, to a high degree, that the local Hubble constant varies minimally.

7.3 Dipole Calculations

7.3.1 The Abell Cluster Inertial Reference Frame

The sky and redshift distributions of our cluster sample play important roles in this study. Adequate sky coverage is necessary for any dipole measurement and we have tailored our redshift distribution to test claims of bulk flows on large scales. It is thus useful to supplement our data with peculiar velocity measurements of other relatively distant clusters, so long as they have been obtained in a manner consistent with our approach. The distant members ($cz > 4500$ km s^{-1}) of the SCI sample affords such an opportunity. The SCII data have been processed according to the precepts outlined for the SCI data and, as mentioned beforehand, both samples use a similar TF template relation to extract peculiar velocities. To ensure uniform sky coverage and a redshift overlap with the SCII sample, we restrict the following dipole computations to involve only the distant half of the SCI sample, the 12 clusters beyond $45h^{-1}$ Mpc. We shall refer to the combined sample of 64 clusters as the Abell cluster inertial frame, or the ACIF.

7.3.2 The Abell Cluster Dipole

The estimate of the reflex motion of the Local Group with respect to the ACIF, $\mathbf{V}_{\rm lg-acif}$, follows from a chi-squared minimization of the dipole vector with respect to the cluster sample's peculiar velocity field *in the Local Group frame*, i.e. the $\mathbf{V}_{\rm lg-acif}$ that minimizes

$$\chi^2 = \sum_{i=1}^{N} \frac{1}{s_i}\Big(\frac{V_i + \hat{\mathbf{r}}_i \cdot \mathbf{V}_{\rm lg-acif}}{\epsilon_i}\Big)^2 \qquad (7.3)$$

where $\hat{\mathbf{r}}_i$ is the unit vector in the direction of the $i^{\rm th}$ cluster. The factor $1/s_i$ allows us to vary the weighting scheme; we assume $1/s_i$=1 in what immediately follows, and we will henceforth call this "Case a." A straightforward application of this equation yields $\mathbf{V}_{\rm lg-acif} = (V_x, V_y, V_z) = (-25, 508, 245)$ km s^{-1}, or alternatively, 564 km s^{-1} towards $(l, b) = (267°, 26°)$ (in Galactic Cartesian coordinates, the $x - y$ plane lies along the disk of the Galaxy ($b = 0°$) with the x-axis pointing to the Galactic center; the z-axis is oriented towards the Galactic North Pole). A robust approach to estimating the uncertainty in the dipole is to utilize the characteristics of the cloud of solutions generated from Monte Carlo simulations. Like the other Monte Carlo simulations described in this work, we generate a Monte Carlo trial sample by adding random Gaussian deviates of the peculiar velocity errors to the original peculiar velocities. The dipole solution is calculated, and the process is repeated for a large number of realizations to construct a Monte Carlo cloud. The dispersions in the dipole components are (93,119,80) km s^{-1}, implying an error-bias corrected dipole of 538 ± 113 km s^{-1} towards $(l, b) = (267°, 26°) \pm 11°$ (error bias systematically inflates the dipole amplitude: $V_{\rm cor}^2 = V_x^2 + V_y^2 + V_z^2 - \epsilon_x^2 - \epsilon_y^2 - \epsilon_z^2$). Figure 7.4 displays in Galactic Cartesian coordinates the error cloud of 10^3 points, projected onto the three planes. We can also use this cloud to better understand the statistical likelihood domains of the measurement; the contours plotted enclose 68% and 95% of the data, respectively representing 1σ and 2σ confidence regions. Note that the components of the direct solution (marked by crosses) are located near the centroids of the ellipses, indicating agreement with the average Monte Carlo solution. The filled circles indicate the dipole motion of the Local Group with respect to the CMB, whereas the open, crossed circles with the accompanying error bars show the value as determined by LP. Table 7.2 summarizes the dipole results, parenthetically including the dipole amplitudes corrected for error biasing.

A $\Delta\chi^2$ analysis can be another approach to understanding the dipole result. The difference in χ^2 using our solution and one with a null reflex Local Group motion is $\Delta\chi^2 = 51.4$ (or $\Delta\chi^2 = 38.5$ if we account for the errors on the CMB dipole). For a three parameter fit this implies we can guarantee non-zero Local Group motion with 99.999% confidence. More importantly, we can test for agreement with the COBE solution for Local Group motion, $\mathbf{V}_{\rm lg-cmb} = (9, -542, 301)$ km s^{-1}. In this case $\Delta\chi^2 = 1.4$; our results for the Local Group motion agree with that of COBE to well within 1σ — the COBE solution lies within our 68%

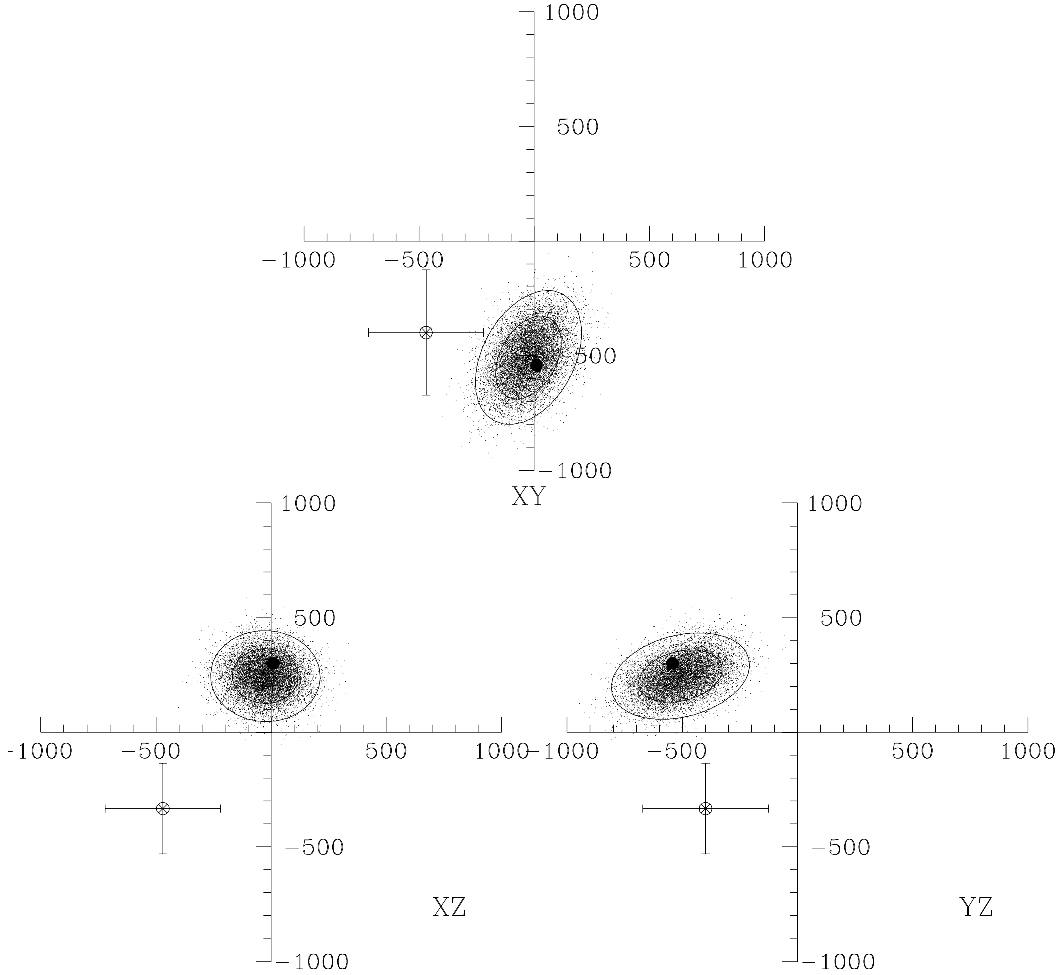

Figure 7.4 Galactic Cartesian coordinate representation of the motion of the Local Group with respect to the Abell cluster inertial reference frame. The small dots plotted are Monte Carlo realizations of the peculiar velocity data set, and the ellipses drawn represent the 1σ and 2σ confidence regions of the dipole. The large filled circles indicate the motion of the Local Group with respect to the CMB and the open, crossed circle shows the dipole motion with respect to the LP reference frame, along with the quoted uncertainty.

confidence region. Conversely, $\Delta\chi^2 = 17.8$ in a comparison between our solution and that of LP (computed including the LP error estimate); we disagree with the LP result to better than 99.9% (a 3.5σ difference). We discuss next the ingredients necessarily included in other relevant dipole computations.

Table 7.2 Cluster Dipole

SCI+SCII	N_c	V	(l, b)
cz_{tf} >4500 km s^{-1}		km s^{-1}	$^\circ$
Case a: $s_i \equiv 1$			
	64	564(538)±113	(267,+26)±11
incl. HMBC[a]	64	564(537)±113	(265,+27)±11
incl. ZoA clusters	80	447(416)±101	(273,+39)±15
excl. A3266,A3667	62	560(529)±112	(266,+27)±11
Case b: $s_i\epsilon_i^2 \equiv 1$			
	64	572(408)±279	(278,+21)±22
incl. HMBC[a]	64	761(647)±285	(270,+16)±16
incl. ZoA clusters	80	428(296)±196	(280,+29)±26
excl. A3266,A3667	62	499(320)±217	(256,+45)±36

[a] homogeneous Malmquist bias correction

7.3.3 The Dipole Under Equal Volume Weighting

The previous formalism does not weigh equal volumes equally, but rather tends to weigh nearby regions more heavily. This unequal volume weighting exists because the completeness of our cluster sample and the accuracy of our peculiar velocities fall with increasing distance. Compounding the problem is the fact that the nearer clusters have slightly richer member counts, also leading to higher peculiar motion uncertainties. In short, both the density and the accuracy of the sampling falls with redshift. Figure 7.5 portrays the relative cluster distribution versus redshift for our sample and the Abell catalog. Clearly, the completeness drops beyond $120h^{-1}$ Mpc; an exponential fit to the completeness function of the SCI+SCII sample follows $\exp(-cz[\mathrm{km/s}]/4700)$. To accomplish equal volume weighting, or more precisely *equal spherical shell weighting*, we construct the factor $1/s_i$ in Equation 7.3 to account for the characteristics of our cluster selection function. The resulting combination of our cluster selection function

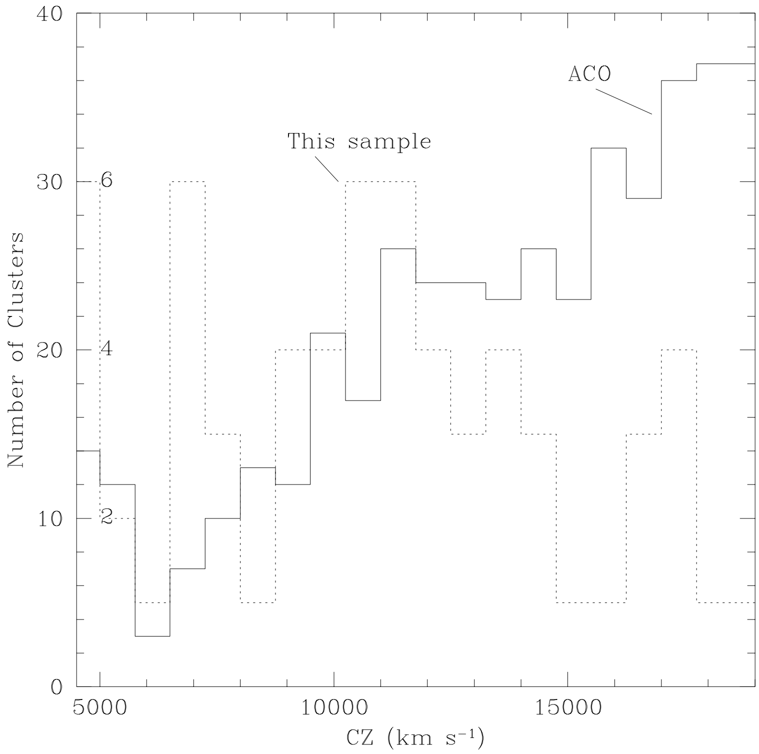

Figure 7.5 The redshift distribution of our SCI+SCII cluster sample (dotted line) and the ACO catalog (solid line). The inner y-axis refers to the SCI+SCII sample.

and the peculiar velocity error distribution yields a roughly flat weighting with redshift: $1/(s_i \epsilon_i^2) \approx 1$, hereafter referred to as "Case *b*." Results for the dipole computations using this fair weighting scheme are also listed in Table 7.2. We remind the reader that the dipole amplitudes corrected for error biasing are included in parentheses. We again find agreement with the COBE solution, though the associated errors are admittedly larger – giving equal weights to near and far clusters inevitably increases the dipole uncertainty since distant clusters have less accurate peculiar velocities. Results are also listed for the dipole computation when the clusters A3266 and A3667 are excluded. In the course of performing jackknife and statistical tests of the Case *b* dipole (Section 7.4), we found these two clusters to unduly alter the results. This is a possible indication that our approach to equal volume weighting is flawed, at least to the extent that A3266 and A3667 are given weights equal to those of other clusters. We shall thus conservatively exclude these two clusters from further Case b results. In Figure 7.6, a display of Monte Carlo realizations for the Case b dipole, we see the LP result is still certainly excluded.

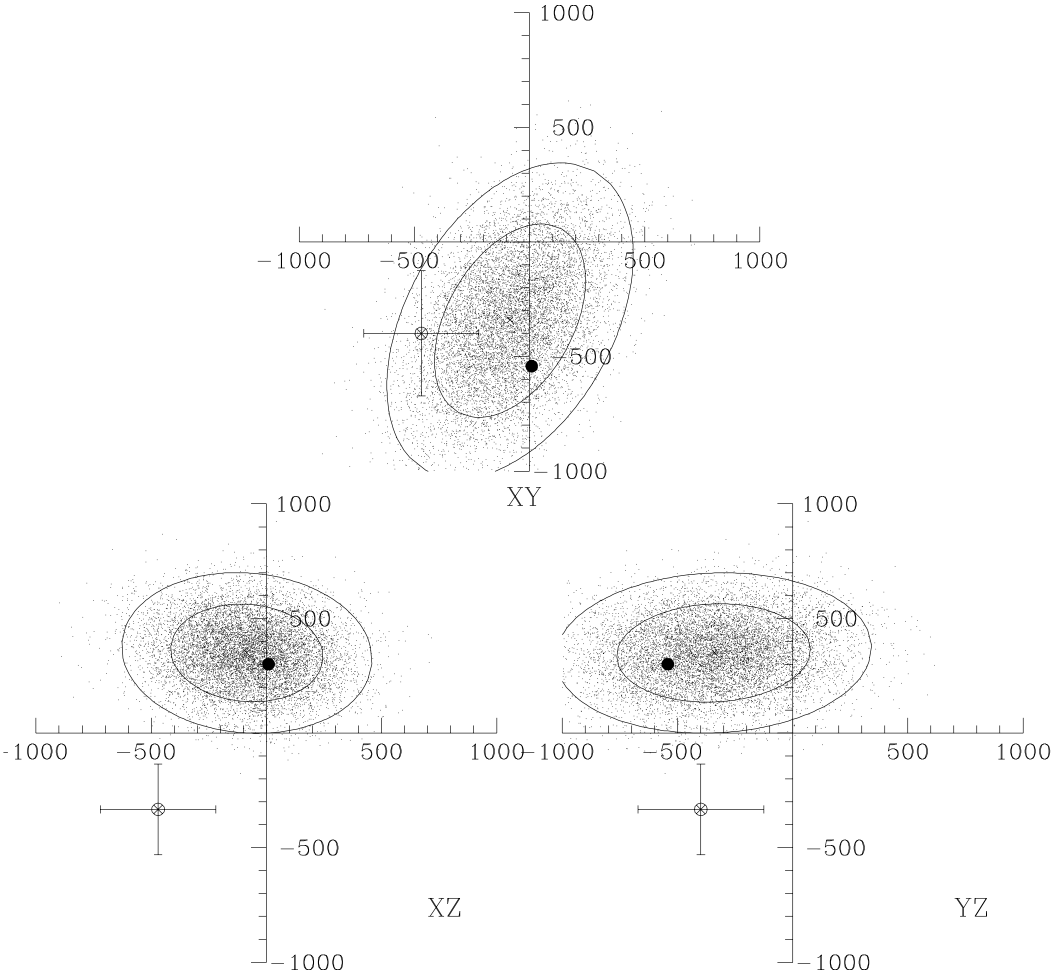

Figure 7.6 Similar to Figure 7.4, but for equal volume weighting: $1/(s_i\epsilon_i^2) = 1$.

It is also useful to project the confidence ellipses onto the sky. Figure 7.7 does so for both Case a (solid lines) and Case b (dashed lines). The plot is in Galactic

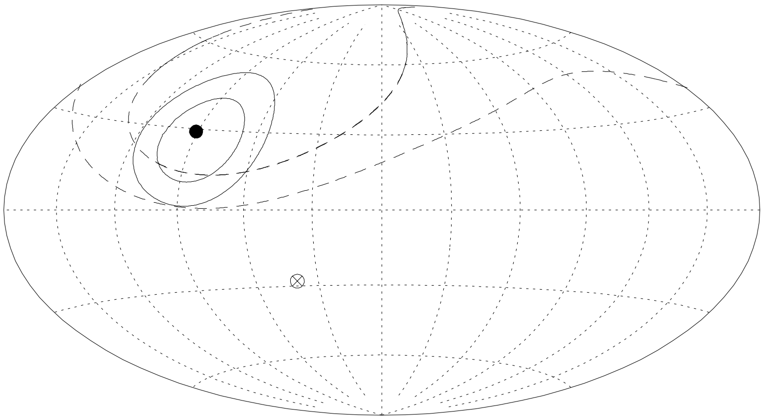

Figure 7.7 The 1σ and 2σ confidence ellipses projected onto the sky. The solid (dashed) lines are for Case a (b). The plot is in Galactic coordinates, centered at $(l, b) = (180°, 0°)$. The two data points follow the format of Figure 7.4.

coordinates, centered at $(l, b) = (180°, 0°)$, and the two circles again represent the Local Group motion with respect to the CMB and the LP ACIF. The apex of our dipole in either case agrees with the apex of $\mathbf{V}_{\mathrm{lg-cmb}}$.

We use these results in concert with the estimate of the Local Group motion in the CMB frame to ascertain the motion of the cluster inertial frame with respect to the CMB itself,

$$\mathbf{V}_{\mathrm{acif-cmb}} \equiv \mathbf{V}_{\mathrm{lg-cmb}} - \mathbf{V}_{\mathrm{lg-acif}}. \tag{7.4}$$

We find the bulk flow amplitude for the two cases $1/s_i = 1$ and $1/(s_i \epsilon_i^2) = 1$ to be 106 ± 93 km s^{-1} and 248 ± 258 km s^{-1}; corrected for error biasing, the amplitudes reduce to a null bulk flow. Table 7.3 summarizes our bulk flow findings. The interpretation is similar to what has already been described: the inertial frame defined by the distant SCI+SCII clusters is determined to be at rest with the fiducial rest frame of the CMB.

As a final remark, we note that the above estimates for the amplitude of

Table 7.3 Abell Cluster Inertial Frame Bulk Flow

SCI+SCII $cz_{\rm tf}$ >4500 km s^{-1}	$N_{\rm c}$	$s_i \equiv 1$ V km s^{-1}	$s_i \epsilon_i^2 \equiv 1$ V km s^{-1}
	64	106(000)±093	106(000)±164
incl. HMBC[a]	64	115(000)±094	218(000)±271
incl. ZoA clusters	80	197(111)±112	194(000)±197
excl. A3266,A3667	62	108(000)±099	248(000)±258

[a] homogeneous Malmquist bias correction

the bulk flow in the local Universe match well what is expected from theoretical considerations. Several parties expect bulk flow motions, on size scales similar to that encompassed by our sample, to be of order ∼100 – 400 km s^{-1} (e.g. Feldman and Watkins 1994; Strauss *et al.* 1995; Moscardini *et al.* 1996).

7.3.4 The Effect of Cosmic Scatter and The Zone of Avoidance

Even if we could measure peculiar motions with infinite accuracy, bulk flow measures would still have an attached uncertainty – density irregularities on scales much smaller than those responsible for the bulk motion should also affect cluster motions. On large scales, the effect of these small scale fluctuations is not coherent; they contribute noise to the bulk flow. The luxury of reducing this uncertainty statistically, through a simple increase in the number of measured peculiar velocities, is unfortunately not so accessible from an observational point of view. Adding to the impreciseness of streaming motion estimations is the presence of the ZoA. The region of the sky that is obscured by the plane of the Galaxy is rather large even in the I band. As we saw in Figure 2.1, the ZoA extends to about ±20° in Galactic latitude, or alternatively, it covers about a third of the sky. An observational approach to limiting the ZoA's effect is to obtain TF data for a few of the low galactic latitude clusters that are visible. We have avoided this approach for reasons of economy and accuracy. Many of the viable candidates in such clusters are precluded because of flux contamination from the Galactic stellar field, but more importantly, we have abstained from working at low Galactic latitudes because Galactic extinction corrections there are highly uncertain.

Dipole Calculations with Artificial ZoA Clusters

Techniques have been developed to account for the effect of the ZoA. In reconstructions of the Abell catalog cluster dipole, Branchini *et al.* (1996) fill in the ZoA by extrapolating cluster properties from nearby regions. This is only possible, though, when there is a statistically large enough sample from which to operate. We thus turn to numerical models and simulations to gauge the effect of the ZoA on bulk motion measures. Tables 7.2 and 7.3 also list results when a set of ZoA clusters are included in the Monte Carlo realizations of the dipole calculations. For each trial we generate $N_{\rm cl}/3$ to $N_{\rm cl}/4$ fake clusters between $-20° < b < 20°$ that mimic the overall characteristics of the observed cluster sample. The amplitudes and apices agree less well with $\mathbf{V}_{\rm lg-cmb}$, but we emphasize that the clusters we have added have, on average, *zero peculiar velocity in the Local Group frame*, an extremely conservative scenario.

Probing ZoA Effects with N-Body Simulations

N-body simulations kindly provided by S. Borgani allow us to further test the impact of the ZoA and the effects of cosmic scatter on our dipole calculations.

Such simulations allow one to gauge uncertainties introduced by blanking large swaths of the sky. In other words, comparisons can be made between dipoles that sample the entire sky and those that are limited by a ZoA. Moreover, simulated peculiar velocities have no "observational errors." Thus, we can test for different effects to a higher accuracy than would otherwise be attainable. As described in Moscardini *et al.* (1996), the simulations use the Zel'dovich approximation to mimic gravitational dynamics. The simulations are carried out on a grid of 256^3 points within a cube of $960h^{-1}$ Mpc sides, a region large enough to contain all the waves responsible for motions on scales of $200h^{-1}$ Mpc. A variety of cosmological models are simulated.

To enable a fair comparison with our cluster observations, we cull the number of density peaks to a density similar to that found in the Abell/ACO catalog: $n_{\rm cl} \simeq 2\times 10^{-5}(h^{-1}{\rm Mpc})^{-3}$, or an average cluster-cluster spacing of $\simeq 40h^{-1}$ Mpc. We also only calculate a cluster dipole for "Local Group-like" observers. In other words, $|V_{\rm lg}| = 620 \pm 44$ km s^{-1} for a top-hat sphere of radius $7.5h^{-1}$ Mpc, and a matter overdensity range of $-0.2 \leq \delta\rho/\rho \leq 1$. Such criteria are satisfied by 10^2 to 10^3 grid points, depending on the cosmological model.

The dipole calculation is executed three times for each Local Group-like observer using a random sample of clusters whose space distribution is fashioned after the combined SCI+SCII cluster sample. The first computation tests only for the effect of cosmic variance in the peculiar velocity field and thus does not involve any sort of masking of the sky. The apex of this first dipole computation can also serve as a working reference point for the "true" dipole. The second calculation includes a randomly placed ZoA for each observer, whereas the third calculation involves a ZoA mask that is oriented, with respect to the true apex, in the same manner we observe our own Local Group motion with respect to the plane of the Milky Way. As previously noted, the dipole calculations are carried out assuming negligible peculiar velocity errors. This is reminiscent of Case b's equal volume weighting. The variance of the dipole solution for the set of Local Group-like observers gives us an idea of how well we can recover intrinsic dipole flows. Table 7.4 gives the sample dipole variance for a wide variety of cosmological scenarios. We do not list separate results for a random and a non-random

Table 7.4 Cosmic Variance and the Cluster Dipole

Model	$N_{\rm obs}$	$\Omega_\circ$	Ω_Λ	σ_v km/s	no ZoA $\sigma_{\rm bf}$ km/s	ZoA $\sigma_{\rm bf}$ km/s
SCDM	380	1.0	0.0	664	167	178
OCDM04	275	0.4	0.0	197	86	95
OCDM06	1048	0.6	0.0	415	128	142
OCDM08	534	0.8	0.0	574	166	159
ΛCDM02	807	0.2	0.8	247	133	144
ΛCDM03	1031	0.3	0.7	388	163	172
ΛCDM04	725	0.4	0.6	504	170	187
ΛCDM06	526	0.6	0.4	570	161	174
ΛCDM08	408	0.8	0.2	623	166	183

ZoA placement, as the differences are minimal. The columns are organized as follows:

Column 1: Cosmological model, as described in Moscardini *et al.* (1996). The models assume cold dark matter (CDM). The 'lambda' models (ΛCDM) and the 'standard' model (SCDM) refer to a flat Universe with and without a cosmological constant, whereas an open Universe (with no cosmological constant) is represented by the OCDM models.

Column 2: Number of Local Group-like observers.

Column 3: Matter density parameter.

Column 4: Cosmological constant density parameter.

Column 5: Line-of-sight rms cluster velocity (Moscardini *et al.* 1996).

Column 6: 1σ variation in bulk flows for ZoA-free samples.

Column 7: 1σ variation in bulk flows for ZoA-masked samples.

The majority of the simulations indicate that the measurement of 60–70 cluster cosmic motions limit bulk flow measurements to an accuracy no better than $\sim$150 km s^{-1}; the presence of a ZoA further confuses dipole measurements by $\sim$60 km s^{-1}, resulting in an overall uncertainty of $\sim$160 km s^{-1}.

7.4 Statistical Tests

We present in this section a suite of statistical tests of the cluster dipole calculation. We do this to further our understanding of the calculation's reliability, and to seek out any latent conceptual or mathematical errors. The first test follows the standard *bootstrapping* technique and involves a large number of resamplings of the original data set. Rather than Monte Carlo–generate new peculiar velocities, one for each of the sample's clusters, bootstrapping instead draws peculiar velocities from the measured distribution itself, but without regard for the number of times a given cluster is selected, i.e. double and triple counting is allowed, at the expense of ignoring some clusters. Typically, a fraction $1/e$ of the sample is not included in each trial sample (Press *et al.* 1992). We do this for 10^4 trials and compute the dipole for each. The information from this resampling technique is displayed in Figure 7.8 for each component of the Local Group motion with respect to the ACIF. The upper row gives histograms of the bootstrapping

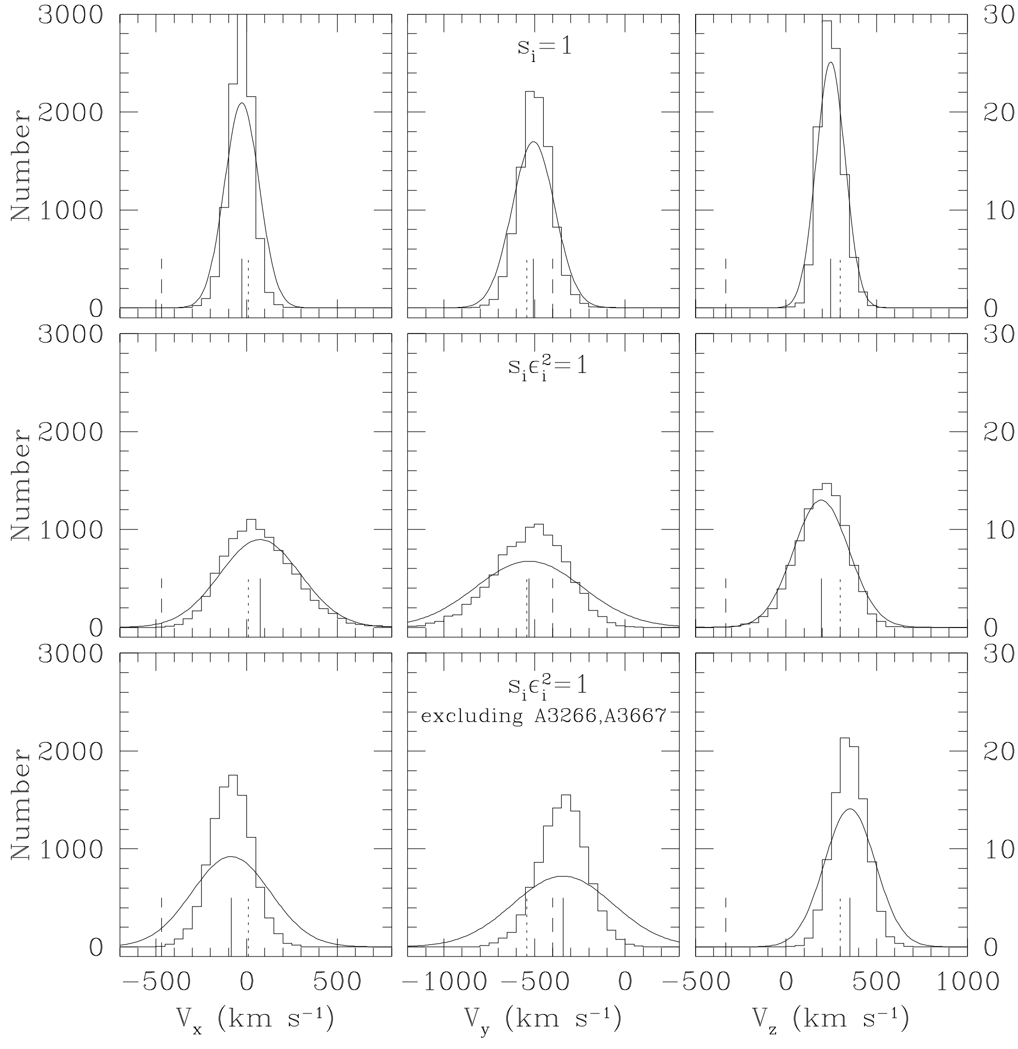

Figure 7.8 Dipole solutions (in Galactic Cartesian coordinates) obtained through bootstrap resamplings of the cluster sample. The vertical lines drawn indicate the vector for Local Group motion with respect to the Abell cluster inertial frame (solid), the CMB (dotted), and the LP ACIF (dashed). The curves overlayed on the bootstrap histograms are equal-area Gaussians with dispersions equivalent to those from the Monte Carlo simulations. The rows differ in weighting scheme and cluster membership: the upper row assumes Case *a* weighting whereas the lower two rows follows Case *b*'s weighting prescription; the data for the bottom row has been calculated ignoring the two clusters A3266 and A3667.

solutions assuming the peculiar velocities are weighted by the square of their errors (Case a). The lower two rows are for equal volume weighting (Case b), with the data for the bottom row computed excluding the clusters A3266 and A3667. The vertical lines drawn indicate the vector for Local Group motion with respect to: the SCI+SCII ACIF (solid), the CMB (dotted), and the LP ACIF (dashed). The curves overlayed on the bootstrap histograms are Gaussians with dispersions equivalent to those from the Monte Carlo simulations. The area under each curve is the same and matches the area covered by the bootstrap histograms. The curves are plotted to give the relative sense of the dipole component errors quoted from the simulations. If the dispersions in the bootstrap resampling solutions can also be considered fair estimators of the errors, it is evident from the figure that the Monte Carlo dispersions are quite conservative error estimators. The z-component of the bulk flow is unsurprisingly accurately determined (i.e. sharply peaked), given the location of the ZoA in this coordinate system. Also equally evident here, as in Figures 7.4 and 7.6, is the broader range of allowable solutions for Case b. The LP solution is disallowed for either Case a or Case b.

A second statistical technique we profit by is that of *subsampling*. In this method we compute the cluster dipole using only a fraction of the sample. Doing this for a large number of randomly selected subsamples can also give an indication of the dipole's reliability. Figure 7.9 shows histograms of our results in a format similar to that displayed in Figure 7.8. Each subsample contains only 40 clusters of the original set. Note that the LP V_x and V_z solutions do not even fall within the scales plotted. The bimodal appearance of the V_x and V_y distributions in the middle row arise from the influence of A3266 and A3667. These clusters

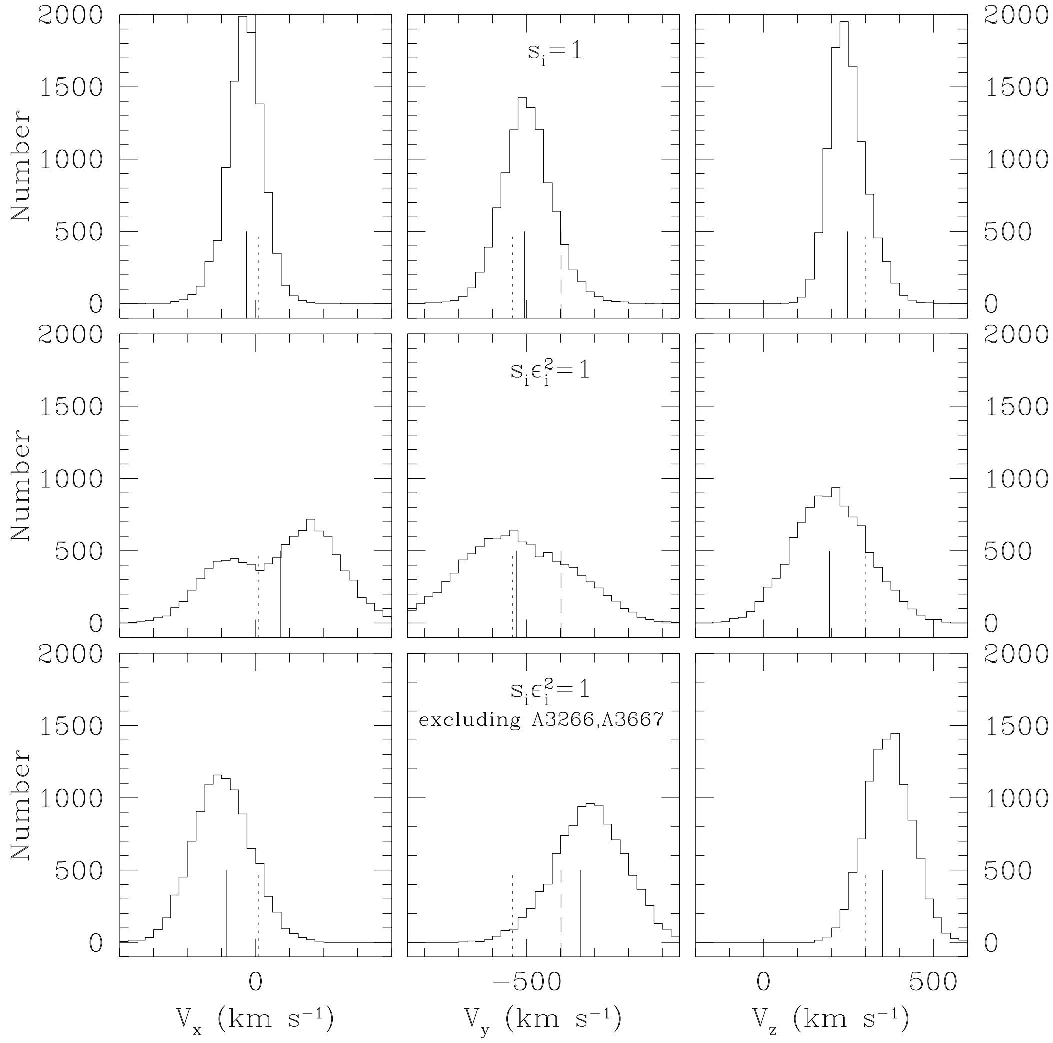

Figure 7.9 Similar to Figure 7.8, except the resampling is done using only a random portion ($N = 40$) of the cluster data set.

have large, highly uncertain peculiar velocities that skew the dipole when they are given the same weight as the other clusters. It is evident from the bottom row, where the Case *b* calculation has been repeated excluding A3266 and A3667, that these clusters are responsible for the distortions of the middle row's histograms.

We can see the impact of A3266 and A3667 more clearly in a different test of the dipole result. The third test is a *jacknife* investigation, whereby individual clusters are excluded to gauge the dipole's reliance on a given cluster. Figure 7.10 gives such a plot for both Case a and Case b weighting schemes. Again, we have included the calculation with and without A3266 and A3667. The dashed lines

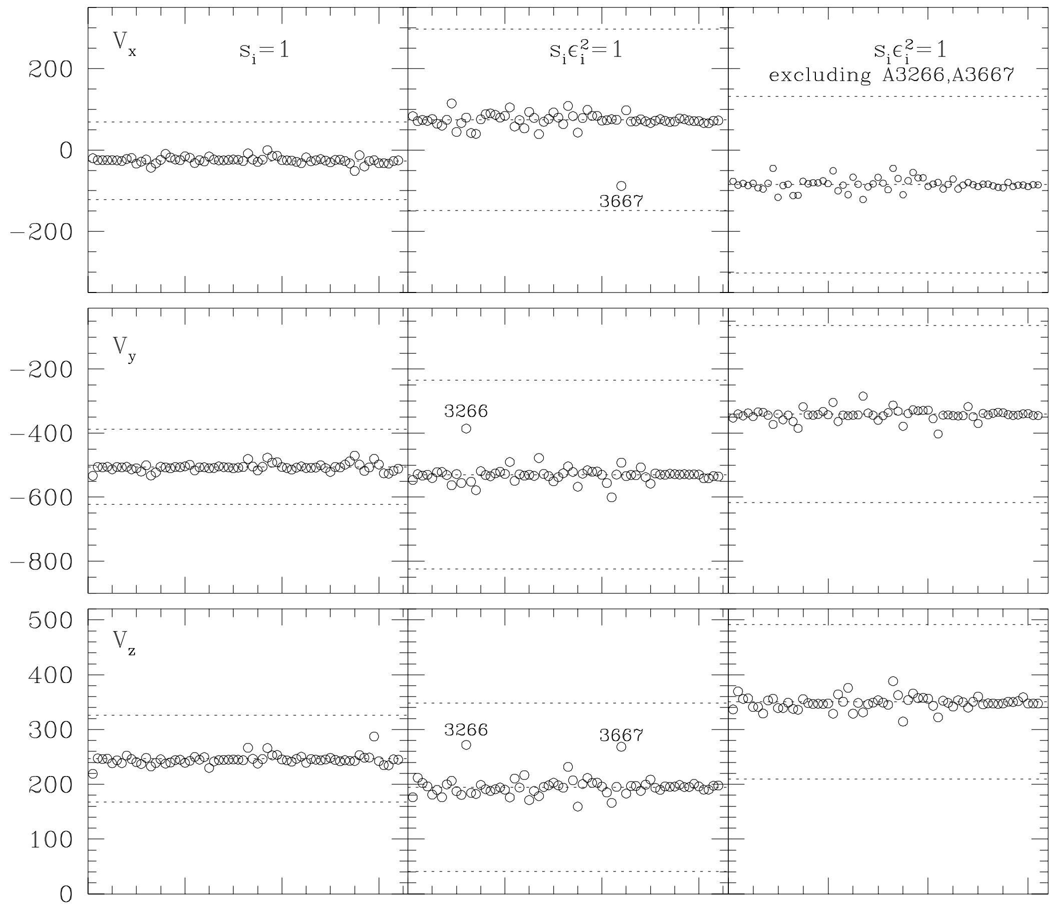

Figure 7.10 A jackknife test of the dipole solutions. The left hand column gives the Galactic Cartesian solutions for Case a, the middle column for Case b, and the right hand column for Case b excluding A3266 and A3667, the two outliers that are labeled. The dipole components and their 1σ confidence regions are indicated by the dashed horizontal lines.

drawn mark $\mathbf{V}_{\mathrm{lg-acif}}$ and its uncertainty. Clearly, the most discrepant outliers are A3266 and A3667, as labeled in the plots comprising the middle column. Though the solutions in this column that exclude A3266 and A3667 are within the 1σ confidence intervals, the discrepancy is large. We thus deem Case b results to be reliable only in the absence of these two clusters.

7.5 Summary

From the beginning, our goal has been to conclusively test claims of high amplitude, large scale bulk motions using Tully-Fisher redshift-independent distances to galaxy clusters. In collaboration with the accurate SCI peculiar velocities from Giovanelli *et al.* (1998a), we have utilized our sample of 52 cluster peculiar velocities to accomplish our goal, and in the process, to establish several other determinations important to astrophysics.

• A popular means to constraining cosmological models has been to infer a plausible range for the cosmological density parameter, $\Omega_\circ$, through measures of cluster peculiar velocities. Since clusters are believed to trace well the underlying peculiar velocity field, reliable measures of the typical cluster motion constitute sensitive probes of large scale structure and hence the cosmology under which such structure formed. We find the rms line-of-sight peculiar velocity for the SCII sample to be 341 ± 43 km s^{-1}. Our value favors a somewhat larger $\Omega_\circ$ than does the estimate for the SCI sample ($\sim$270 km s^{-1}), but other catalogs of less accurate peculiar velocities exhibit even larger rms values than 341 km s^{-1} (e.g. Moscardini *et al.* 1996).

• The combined SCI+SCII sample affords a powerful check of the constancy of the Hubble constant in the local Universe. Following the procedure outlined by Zehavi *et al.* (1998), we have investigated the existence of any distance trends in deviations from Hubble flow. In contrast to the findings of Zehavi and coworkers, who used measurements of 44 SN Ia light curves to demonstrate that $H_\circ$ is inflated by 6% within $70h^{-1}$ Mpc, we find the parameter over this range to match the global value determined from our sample. Our data support an unchanging local Hubble constant.

• The reflex motion of the Local Group has been calculated with respect to the Abell cluster inertial reference frame represented by the distant SCI+SCII sample. Upon weighting peculiar velocities by their error estimates, we determine the Local Group motion to be 564±113 km s^{-1} in the direction $(l, b) = (267°, 26°) \pm 11°$. We have repeated the calculation employing a different weighting scheme, one where equal volumes are treated equally. In this case the dipole motion is 499 ± 217 km s^{-1} towards $(256°, 45°) \pm 36°$. Both results agree with the best estimates for the Local Group motion in the CMB frame. In other words, the bulk motion of the ACIF in the CMB reference frame is rather small, at most 200 km s^{-1}. The spatial distribution of our data has been carefully selected to accurately measure the bulk flow of the local Universe out to an effective depth of $\sim 100h^{-1}$ Mpc. Our data exclude the LP finding for a such a bulk flow with 99.999% confidence.

• Finally, we have applied a variety of statistical tests on our dipole calculations. Bootstrap and subset resamplings in addition to jacknife tests indicate Case *a* dipole determinations to be quite robust. However, there is evidence for A3266 and A3667 to unfairly skew Case *b* dipole computations. The data for these two clusters both show large amplitude but largely uncertain peculiar motions. In all likelihood, our primitive analysis of our cluster selection function is insufficient, and hence these two clusters should not be given weights equal to those of other clusters in attempting to simulate equal volume weighting.

Chapter 8

Summary

Aided by the generous allotment of telescope time and the serendipitous scheduling of observing runs during fair sky conditions, we have completed an ambitious Tully-Fisher program to accurately probe the large-scale motions of clusters of galaxies. Over the last three plus years we have obtained optical rotation curves and photometry for 522 galaxies at the Mt. Palomar 5 m, the CTIO 4 m, and the KPNO and CTI0 0.9 m telescopes; rotational velocity widths from HI profiles supplement the widths extracted from the rotation curve sample. The galaxies originate from an all-sky sample of 52 rich Abell clusters distributed between 50 and $200h^{-1}$ Mpc. We have taken advantage of this rich data set to achieve several important goals.

• We have taken the 52 individual cluster TF relations and collapsed them into one template to determine a precise TF kinematical offset, accurate to 0.02 magnitudes. In conjunction with the robust TF slope extracted from the relatively nearby SCI cluster sample (G97b), we find the I band TF relation to follow

$$M_I - 5\log_{10} h = -7.68(\log_{10} W - 2.5) - 20.91. \tag{8.1}$$

The relation has an average scatter of 0.38 magnitudes. The process of constructing the template required the consideration of various biases; the two most important effects the above template accounts for are the undersampling of the faint end of the luminosity function and the different TF offsets that exist for different spiral morphologies. This TF relation can be used to calibrate the peculiar velocity field out to $200h^{-1}$ Mpc. It may appropriately be applied to inclined galaxies of any spiral type residing in a wide variety of environments, from the sparsely populated field to the cores of rich clusters.

• Each cluster TF relation has been referred to the template relation to produce a sample of 52 peculiar velocities. Since each cluster TF relation has been constructed using N galaxies, the redshift-independent distances derived are more accurate by a factor of $\sqrt{N}$ when compared to like distances for individual galaxies. The rms line-of-sight component of the cluster peculiar velocity for our sample, unbroadened for measurement errors, is 341 ± 43 km s^{-1}.

• A test of the claimed variability in the local Hubble constant has been performed. Zehavi *et al.* (1998) applied their observations of 44 SN Ia within $300h^{-1}$ Mpc to determine a Hubble constant within $70h^{-1}$ Mpc that is 6% larger than the fiducial value they find for the entire sample. We have used to advantage the combined SCI+SCII sample to examine the purported Hubble bubble. Our results point to a rather quiescent Hubble constant beyond $30h^{-1}$ Mpc.

• We have computed the reflex motion of the Local Group with respect to the reference frame defined by our relatively distant SCI+SCII cluster sample. We find the Local Group motion in this frame to be 564$\pm$113 km s^{-1} in the direction $(l, b) = (267^\circ, 26^\circ) \pm 11^\circ$ when peculiar velocities are weighted according to their errors. After optimizing the calculations to sample equal volumes fairly, the vector is 499 ± 217 km s^{-1} towards $(256^\circ, 45^\circ) \pm 36^\circ$. Both results agree with the best estimates for the Local Group motion in the CMB frame to within 1σ, or to a confidence level of 68%. Taken from a different perspective, this implies that the relative motion of the CMB and the cluster sample inertial frames is rather small; the bulk flow of the clusters between 500 and $200h^{-1}$ Mpc is at most $\sim$200 km s^{-1}. This contrasts with the findings of LP, who employed BCG distances to the 115 nearest Abell clusters to find the bulk motion of a similar volume of space to have an amplitude of 689$\pm$178 km s^{-1}. We disagree with the LP result to a high degree (>99.9% confidence).

- We find evidence for a small convergence depth of order $60h^{-1}$ Mpc. It is insightful to first consider recent results from Giovanelli *et al.* (1998a). In their work they use two independent samples of TF distances, one comprised of 24 clusters of galaxies between 10 and $90h^{-1}$ Mpc (the SCI sample) and the other made up of a large sample of spiral field galaxies covering a similar distance regime (the SFI sample). With respect to spherical data shells of increasing radii, they find the reflex motion of the Local Group increasingly mirrors the best estimates of its motion in the CMB frame. Combine this with our supporting evidence for a minimal bulk flow for the distant SCI+SCII sample: negligible bulk flows are found for the distant portions of the SFI and SCI samples and a negligible bulk flow is found for the volume of space beyond, out to $\sim$$200h^{-1}$ Mpc. Taken in its simplest form, our combined results suggest a small local convergence depth.

The local peculiar motion appears to stem from matter inhomogeneities within $60h^{-1}$ Mpc.

Appendix A

Rotation Curves and Data Tables

Figure A.1: displays the optical rotation curves.

Table A.1: lists the results of the spectroscopic observations.

Table A.2: lists the results of the photometric observations.

Table A.1 Galaxy Spectroscopic Parameters

Table A.2 Galaxy Photometric Parameters

References

Aaronson, M. & Mould, J. 1983, Ap. J., 265, 1

Aaronson, M., Bothun, G.D., Mould, J., Huchra, J., Schommer, R., & Cornell, M. 1986, Ap. J., 302, 536

Abell, G. 1958, Ap. J. Suppl., 3, 211

Abell, G., Corwin, H.G., & Olowin, R.P. 1989, Ap. J. Suppl., 70, 1 (ACO)

Amram, P., Sullivan, W.T., Balkowski, C., Marcelin, M., & Cayatte, V. 1993, Ap. J., 403, L59

Andreon, S. 1998 Astr. Ap., in press; astro-ph/9804028

Arbolino, M.V. & Ruffini, R. 1988, Astr. Ap., 192, 107

Bahcall, N.A. & Oh, S.P. 1996, Ap. J., 462, L49

Bahcall, N.A., Gramann, M., & Cen, R. 1994a, Ap. J., 436, 23

Bahcall, N.A., Cen, R., & Gramann, M. 1994b, Ap. J. (Letters), 430, L16

Bardelli, S., Zucca, E., Malizia, A., Zamorani, G., Scaramella, R., & Vettolani, G. 1996, Astr. Ap., 305, 435

Bardelli, S., Zucca, E., Vettolani, G., Zamorani, G., Scaramella, R., Collins, C.A., & MacGillivray, H.T. 1994, M. N. R. A. S., 267, 665

Barmby, P. & Huchra, J.P. 1998, A. J., 115, 6

Bautz, L.P. & Morgan, W.W. 1970, Ap. J. (Letters), 162, L49

Bernstein, G.M., Guhathakurta, P., Raychaudhury, S., Giovanelli, R., Haynes, M.P., Herter, T., & Vogt, N.P. 1994, A. J., 107, 1962

Bird, C.M., Davis, D.S., & Beers, T.C. 1995, A. J., 109, 920

Bird, C.M., Dickey, J.M., & Salpeter, E.E. 1993, Ap. J., 404, 81

Biviano, A., Giuricin, G., Mardirossian, F., & Mezzetti, M. 1990, Ap. J. Suppl., 74, 325

Borgani, S., da Costa, L.N., Freudling, W., Giovanelli, R., Haynes, M.P., Salzer, J.J., & Wegner, G. 1997, Ap. J. (Letters), 482, L121

Borgani, S., Plionis, M., Coles, P., & Moscardini, L. 1995, M. N. R. A. S., 277, 1191

Bosma, A., Byun, Y., Freeman, K.C., & Athanassoula, E. 1992, Ap. J., 400, L21

Branchini, E. & Plionis, M. 1996, Ap. J., 460, 569

Branchini, E., Plionis, M., & Sciama, D.W. 1996, Ap. J. (Letters), 461, L17

Briel, U.G., Henry, J.P, Schwarz, R.A., Bohringer, H., Ebeling, H., Edge, A.C., Hartner, G.D., Schindler, S., Trumper, J., & Voges, W. 1991, Astr. Ap., 246, L10

Brodie, J.P., Bowyer, S., & McCarthy, P. 1985, Ap. J. (Letters), 293, L59

Broeils, A. & Rhee, M.–H. 1997, Astr. Ap., 324, 877

Burbidge, E.M., Smith, H.E., Junkkarinen, V.T., & Hoad, A.A. 1985, Ap. J., 288, 82

Burstein, D. & Heiles, C. 1978, Ap. J., 225, 40

Campusano, L.E., Kneib, J., & Hardy, E. 1998, Ap. J. (Letters), 496, L79

Canizares, C.R., Markert, T.H., & Donahue, M.E. 1988, in Cooling Flows in Clusters and Galaxies, ed. A.C. Fabian (Dordrecht: Kluwer), 53

Cen, R., Bahcall, N.A., & Gramann, M. 1994, Ap. J. (Letters), 437, L51

Chamaraux, P., Cayatte, V., Balkowski, C., Fontanelli, P. 1990, Astr. Ap., 229, 340

Chapman, G.N.F., Geller, M.J., & Huchra, J.P. 1988, A. J., 95, 999

Chiba, M. & Yoshii, Y. 1995, Ap. J., 442, 82

Corbelli, E., Schneider, S., & Salpeter, E. 1989 A. J., 97, 390

Courteau, S. 1997, A. J., 114, 2402

Courteau, S., Faber, S., Dressler, A., & Willick, J. 1993, Ap. J., 412, L51

Crampton, D. & Parmar, P. 1983, P. A. S. P., 95, 127

Croft, R.A.C. & Efstathiou, G. 1994, M. N. R. A. S., 268, L23

Dale, D.A., Giovanelli, R., Haynes, M.P., Scodeggio, M., Hardy, E., & Campusano, L. 1997, A. J., 114, 455 (D97)

Dale, D.A., Giovanelli, R., Haynes, M.P., Scodeggio, M., Hardy, E., & Campusano, L. 1998, A. J., 115, 418 (D98a)

Dale, D.A., Giovanelli, R., Haynes, M.P., Hardy, E., & Campusano, L. 1998, in preparation (D98b)

Dantas, C.C., de Carvalho, R.R., & Capelato, H.V. 1997, Ap. J., 485, 447

Davis, D.S. & Mushotzky, R.E. 1993, A. J., 105, 409

de Vaucouleurs, G. & Corwin, H.G. 1986, Ap. J., 308, 487

de Vaucouleurs, G. & Corwin, H.G. 1985, Ap. J., 297, 23

de Vaucouleurs, G., de Vaucouleurs, A., & Corwin, H.G. 1976, *Second Reference Catalogue of Bright Galaxies.* New York: Springer

de Vaucouleurs, G., de Vaucouleurs, A., Corwin, H.G., Buta, R.J., Paturel, G., & Fouqué, P. 1991, *Third Reference Catalogue of Bright Galaxies.* New York: Springer

Dickey, J.M. & Salpeter, E.E. 1984, Ap. J., 284, 461

Dickey, J.M., Keller, D.T., Pennington, R., & Salpeter, E.E. 1987, A. J., 93, 788

Disney, M.J. 1976, Nature, 263, 573

Dressler, A. 1978, 223, 765

Dressler, A. 1980, Ap. J., 236, 351

Dressler, A. & Schectman, S.A. 1988, A. J., 95, 985

Dressler, A., Thompson, I., & Shectman, S. 1985, Ap. J., 288, 48

Dressler, A., Faber, S.M., Burstein, D., Davies, R.L., Lynden-Bell, D., Terlevich, R.J., & Wegner, G. 1987, Ap. J. (Letters), 313, l37

Ebeling, H., Mendes, de Oliveira, C., & White, D.A. 1995, M. N. R. A. S., 277, 1006

Egikian, A.G., Kalloglian, A.T., Nanni, D., Trevese, D., & Vignato, A. 1984, Astrofizika, 21, 21

Eisenstein, D.J. & Loeb, A. 1996, Ap. J., 459, 432

Escalara, E. & Mazure, A. 1992, Ap. J., 388, 23

Fabian, A.C. & Daines, S.J. 1991, M. N. R. A. S., 252, 17

Fabricant, D., Beers, T.C., Geller, M.J., Gorenstein, P., Huchra, J.P., & Kurtz, M.J. 1986, Ap. J., 308, 530

Fabricant, D.G., Kent, S.M., & Kurtz, M.J. 1989, Ap. J., 336, 77

Fabricant, D., Kurtz, M., Geller, M., Zabludoff, A., Mack, P., & Wegner, G. 1993, A. J., 105, 788

Fabricant, D., Rybicki, G., & Gorenstein, P. 1984, Ap. J., 286, 186

Fanti, C., Fanti, R., Feretti, L., Ficarra, A., Gioia, I.M., Giovannini, G., Gregorini, L., Mantovani, F., Marano, B., Padrielli, L., Parma, P., Tomasi, P., & Vettolani, G. 1982, Astr. Ap., 105, 200

Feldman, H.A. & Watkins, R. 1994, Ap. J. (Letters), 430, L17

Feretti, L., Giovannini, G., Gregorini, L. Padrielli, L., Roland, J., & Valentihj, E.A. 1985, Astr. Ap., 247, 321

Flin, P., Trevese, D., Cirimele, G., & Hickson, P. 1995, Astr. Ap., 110, 313

Freeman, K.C. 1970, Ap. J., 160, 811

Freudling, W. Astr. Ap., 112, 429

Freudling, W., Haynes, M.P., Giovanelli, R. 1992, Ap. J. Suppl., 79, 157

Freudling, W., Martel, H., & Haynes, M.P. 1991, Ap. J., 377, 349

Freudling, W. 1990 PhD thesis, Cornell University.

Freudling, W., Haynes, M.P., & Giovanelli, R. 1988, A. J., 96, 1791

Gilmore, G., Hodge, P., & van der Kruit, P.C. 1990 in The Milky Way as a Galaxy, Mill Valley: Univer. Sci. Books

Girardi, M., Escalara, E., Fadda, D., Guiricin, G., Mardirossian, F., & Mezzetti, M. 1997, Ap. J., 482, 41

Giraud, E. 1987, Astr. Ap., 180, 50

Giovanelli, R., Chincarini, G.L., & Haynes, M.P. 1981, Ap. J., 247, 383

Giovanelli, R., Dale, D.A., Haynes, M.P., & Hardy, E. 1998, in preparation (G98b)

Giovanelli, R. & Haynes, M.P. 1985, Ap. J., 292, 404

Giovanelli, R., Haynes, M.P., Salzer, J J., Wegner, G., Da Costa, L.N., & Freudling, W. 1998, in preparation (G98a)

Giovanelli, R., Haynes, M.P., Salzer, J J., Wegner, G., Da Costa, L.N., & Freudling, W. 1994, A. J., 107, 2036 (G94)

Giovanelli, R., Haynes, M.P., Wegner, G., da Costa, L.N., Freudling, W., & Salzer, J.J. 1996, Ap. J. (Letters), 464, L99

Giovanelli, R., Haynes, M.P., Herter, T., Vogt, N.P., Wegner, G., Salzer, J.J., da Costa, L.N., & Freudling, W. 1997, A. J., 113, 22 (G97a)

Giovanelli, R., Haynes, M.P., Herter, T., Vogt, N.P., da Costa, L.N., Freudling, W., Salzer, J.J., & Wegner, G. 1997, A. J., 113, 53 (G97b)

Giovannini, G., Feretti, L., & Gregorini, L. 1987, Astr. Ap. Suppl., 69 171

Goad, J. W. & Roberts, M.S. 1981, Ap. J., 250, 79

Gramann, M., Bahcall, N.A., Cen, R., & Gott, J.R. 1995, Ap. J., 441, 449

Han, M. 1992, Ap. J. Suppl., 81, 35

Harris, D.E., Costain, C.H., & Dewdney, P.E. 1984, Ap. J., 280, 532

Haynes, M.P. & Giovanelli, R. 1991, Ap. J. Suppl., 77, 331

Haynes, M.P., Giovanelli, R., Herter, T., Vogt, N.P., Freudling, W., Maia, M., Salzer, J.J., & Wegner, G. 1997, A. J., 113, 1197

Haynes, M.P., Giovanelli, R., Salzer, J.J., Wegner, G., Freudling, W., da Costa, L.N., Herter, T., & Vogt, N.P. 1998, in preparation

Haynes, M.P., Herter, T., & Vogt, N.P. 1994, A. J., 107, 1962

Henriksen, M.J. & Markevitch, M.L. 1996, Ap. J. (Letters), 466, L79

Henry, J.P., Briel, U.G., & Nulsen, P.E.J. 1993, Astr. Ap., 271, 413

Henry, J.P. & Briel, U.G. 1991, 246, L14

Henry, J.P. & Briel, U.G. 1995, Ap. J. (Letters), 443, L9

Hoffman, L. & Salpeter, E.E. 1996, in *The Extragalactic Distance Scale*, edited by M. Livio, M. Donahue, and N. Panagia (Cambridge University Press, Cambridge)

Huang, Z. & Sarazin, C.L. 1996, Ap. J., 461, 622

Hubble, E. 1926, Ap. J., 64, 321

Hudson, M.J. 1993, M. N. R. A. S., 265, 72

Karachentsev, I. 1989, A. J., 97, 1566

Kennicutt, R.C. 1989, Ap. J., 344, 685

Kim, K.T. 1995, Journal of the Korean Astronomical Society, 28 1

Knopp, G.P., Henry, J.P., & Briel, U.G. 1996, Ap. J., 472, 125

Kogut, A. *et al.* 1993, Ap. J., 419, 1

Lahav, 0., Lynden-Bell, D., & Rowan-Robinson, M. 1988, M. N. R. A. S., 234, 677

Landolt, A. 1992, A. J., 104, 340

Lauer, T. & Postman, M. 1994, Ap. J., 425, 418 (LP)

Lynden-Bell, D., Faber, S.M., Burstein, D., Davies, R.L., Dressler, A., Terlevich, R.J., & Wegner, G. 1988 Ap. J., 326, 19

Lynden-Bell, D., Lahav, O., & Burstein, D. 1989 M. N. R. A. S., 241, 325

Lynden-Bell, D. & Lahav, O. 1988, in *Large Scale Motions in the Universe: A Vatican Study Week*, ed. by V.C. Rubin and G.V. Coyne, S.J., Princeton, U. Press, Princeton, p. 199

Maccagni, D., Garilli, B., & Tarenghi, M. 1995, A. J., 109, 465

MacKenzie, M., Schlegel, E.M., & Mushotzky, R. 1996 Ap. J., 468, 86

Markevitch, M. & Vikhlinin, A. 1997, Ap. J., 474, 84

Marinoni, C., Monaco, P., Giuricin, G., & Costantini, B. 1998, astro-ph/9805081

Mathewson, D.S. & Ford, V.L. 1996, Ap. J. Suppl.107, 97 (MF)

Mathewson, D.S., Ford, V.L., & Buckhorn, M. 1992, Ap. J. Suppl., 81, 413

Maza, J. *et al.* $http://cfa-www.harvard.edu/iauc/06500/06531.html\#Item2$

Mazure, A., Gerbal, D., Proust, D., & Capelato, H.V. 1986, Astr. Ap., 157, 159

McGaugh, S.S., Schombert, G.D., & Bothun, J.M. 1995, A. J., 110, 573

Melnick, J., & Quintana, H. 1981, A. J., 86, 1567

Miyaji, T., Mushotzky, R.F., Loewenstein, M., Serlemitsos, P.J., Marshall, F.E., Petre, R., Jahoda, K.M., Boldt, E.A., Holt, S.S., Swank, J., Szymkowiak, A.E., & Kelley, R. 1993, Ap. J., 419, 66

Mohr, J.J., Fabricant, D.G., & Geller, M.J. Ap. J., 413, 492

Moles, M., del Olmo, A., & Perea, J. 1985, M. N. R. A. S., 213, 365

Moscardini, L., Branchini, E., Tini–Brunozzi, P., Borgani, Plionis, M., & Coles, P. 1996, M. N. R. A. S., 282, 384

Myers, S.T., Baker, J.E., Readhead, A.C.S., Leitch, E.M., & Herbig, T. 1997, Ap. J., 485, 1

Mushotzky, R.F. & Szymkowiak, A.E. 1988, in Cooling Flows in Clusters and Galaxies, ed. A.C. Fabian (Dordrecht: Kluwer), 53

Navarro, J.F., Frenk, C.S., & White, S.D.M. 1996, M. N. R. A. S., 281, 703

Nemiroff, R.J., Ftaclas, C., & Struble, M.F. 1985, 90, 163

Nulsen, P.E.J., Stewart, G.C., Fabian, A.C., Mushotzky, R.F., Holt, S.S., Ku, W.H., & Malin, D.F. 1982, M. N. R. A. S., 199, 1089

O'Dea, C.P., Gallimore, J.F., Baum, S.A. 1995, A. J., 109, 1669

Oegerle, W.R., Ernst, R.M., Hoessel, J.G. A. J., 1986, 91, 697

Oegerle, W.R., Jewison, M.S., & Hoessel, J.G. 1987, A. J., 92, 519

Oemler, A. 1974, Ap. J., 194, 1

Oke, J.B. & Gunn, J.E. 1982, P. A. S. P., 94, 586

Peebles, P.J.E. 1993, in *Principles of Physical Cosmology*, Princeton University Press

Persic, M. & Salucci, M. 1991, Ap. J., 368, 60

Persic, M. & Salucci, M. 1995, Ap. J. Suppl., 99, 501

Persic, M., Salucci, M., & Stel, F. 1996, M. N. R. A. S., 283, 1102

Pistinner, S. & Sarazin, C.L. 1994, Ap. J., 433, 577

Plionis, M. & Kolokotronis, V. 1998, Ap. J., 500, 1

Plionis, M. & Valdarnini, R. 1991, M. N. R. A. S., 249, 46

Postman, M., Huchra, J.P., & Geller, M.J. 1992, Ap. J., 384, 404

Prada, F., Beckman, J. E., McKeith, C. D., Castles J., & Greve, A. 1994, Ap. J., 423, L35

Press, W.H., Teukolsky, S.A., Vetterling, W.T., & Flannery, B.P. 1992 in *Numerical Recipes* 2nd edition (Cambridge: Cambridge University Press)

Prestwich, A.H, Guimond, S., Luginbuhl, C.B., & Joy, M. Ap. J., 438, L71

Quintana, H., Melnick, J., Infante, L., & Thomas, B. 1985 A. J., 90, 410

Quintana, H., Melnick, J., Proust, D., & Infante, L. 1997, Astr. Ap. Suppl., 125, 247)

Quintana, H. & Ramirez, A. 1990 A. J., 100, 1424

Quintana, H., Ramirez, A., & Way, M.J. 1996, A. J., 112, 36

Raychaudhury, S., von Braun, K., Bernstein, G.M., & Guhathakurta, P. 1997, A. J., 113, 2046

Reid, A.D., Hunstead, R.W., & Pierre, M.M. 1998, M. N. R. A. S., 296, 531

Riess, A., Press, W., & Kirshner, R. 1995, Ap. J. (Letters), 445, L91

Rix, H.–W., Guhathakurta, P., Colless, M. & Ing, K. 1997, M. N. R. A. S., 285, 779

Roberts, M.S. 1978, A. J., 83, 1026

Roberts, M.S. & Haynes, M.P. 1994, Ann. Rev. Astr. Ap., 32, 115

Rowan-Robinson, M., Lawrence, A., Saunders, W., Crawford, J., Ellis, R., Frenk, C.S., Parry, I., Xiaoyang, X., Allington-Smith, J., Efstathiou, G., & Kaiser, N. 1990, M. N. R. A. S., 247, 1

Roettiger, K., Stone, J.M., & Mushotzky, R.F. 1998, Ap. J., 493, 62

Roettiger, K., Burns, J.O., & Pinkney, J. 1995, Ap. J., 453, 634

Rottgering, H., Snellen, I., Miley, G., de Jong, J.P., Hanisch, R.J., & Perley, R. 1994, Ap. J., 436, 654

Rubin, V.C., Roberts, M.S., Thonnard, N., & Ford, W.K. 1976, A. J., 81, 719

Rubin, V.C., Kenney, J., Boss, A., & Ford, W.K. 1989, A. J., 98, 1246

Rubin, V.C., Ford, W.K., & Whitmore, B.C. 1988, Ap. J., 333, 522

Saglia, R. P., Bertschinger, E., Baggley, G., Burstein, D., Colless, M., Davies, R.L., McMahan Jr, R.K., & Wegner, G. 1993, M. N. R. A. S., 264, 961 (S93)

Salpeter, E.E. & Dickey, J.M. 1985, Ap. J., 292, 426

Sandage, A. 1994a, Ap. J., 430, 1

Sandage, A. 1994b, Ap. J., 430, 13

Sandage, A., Tammann, G., & Federspiel, M. 1995, Ap. J., 452, 1

Sarazin, C. 1986, Rev. Mod. Phys., 58, 1

Scaramella, R., Vettolani, G., & Zamorani, G. 1994, Ap. J., 422, 1

Schindler, S. 1996, M. N. R. A. S., 280, 309

Schlegel, D.J., Finkbeiner, P.F., & Davis, M. 1998, Ap. J., 499, in press

Sodre, L., Capelato, H.V., Steiner, J.E., Proust, D., & Mazure, A. 1992, M. N. R. A. S., 259, 233

Strauss, M.A., Cen, R., Ostriker, J.P., Lauer, T.R., & Postman, M. 1995, Ap. J., 444, 507

Strauss, M.A., Yahil, A., Davis, M., Huchra, J.P., & Fisher, K. 1992, Ap. J., 397, 395

Tammann, G.A. 1998, astro-ph/9805013

Tarenghi, M., Garilli, B., & Maccagni, D. 1994, A. J., 107, 1629

Tarenghi, M., Chincarini, G., Rood, H.J., & Thompson, L. 1980, Ap. J., 235, 724

Teerikorpi, P. 1997, Ann. Rev. Astr. Ap., 35, 101

Tini–Brunozzi, P., Borgani, S., Plionis, M., Moscardini, L., & Coles, P. 1995, M. N. R. A. S., 277, 1210

Tomita, A., Nakamura, F.E., Takata, T., Nakanishi, K., Takeuchi, T., Ohta, K., & Yamada, T. A. J., 1996, 111, 42

Trevese, D., Cirimele, G., Cenci, A., Appodia, B., Flin, P., & Hickson, P. 1996, Astr. Ap. Suppl., 125, 459

Tully, R.B. & Fisher, J.R. 1977, Astr. Ap., 54, 661 (TF)

Ulmer, M.P., Wirth, G.D., & Kowalski, M.P. 1992, Ap. J., 397, 430

Valentijn, E.A., Moorwood, A.F.M. 1985, Astr. Ap., 143, 46

Vallee, J.P. & Roger, R.S. 1989, Astr. Ap. Suppl., 77, 31

Vallee, J.P. & Roger, R.S. 1987, A. J., 94, 1

van der Kruit, P. 1990, in *The Milky Way as a Galaxy*, eds. R. Buser & I.R. King, University Science Books, California, p. 212

van der Kruit, P.C. & Searle, L. 1981, Astr. Ap. 95, 105.

Vogt, N.P. Ph.D. thesis, Cornell University

Wakamatsu, K., Heudier, J., Watanabe, T., & Sadaki, M. 1986, A. J., 92, 700

Wang, J., Heckman, T.M. & Lehnert, M.D. 1997, Ap. J., 491, 114

Watkins, R. 1998, M. N. R. A. S., in press

Watkins, R. & Feldman, H. 1995, Ap. J. (Letters), 453, L73

White, R.E., Day, C.S.R., Hatsukade, I., & Hughes, J.P. 1994, Ap. J., 433, 583

Whitmore, B.C., Forbes, D.A., & Rubin, V.C. 1988, Ap. J., 333, 542

Willick, J.A. 1990, Ap. J., 351, 5

Willick, J.A., Courteau, S., Faber, S.M., Burstein, D., & Dekel, A. 1995, Ap. J., 446, 12

Wilson, A.S. & Vallee, J.P. 1982, Astr. Ap. Suppl., 47, 601

Woolf, N. J., 1982, Ann. Rev. Astr. Ap., 20, 367

Xilouris, E.M., Kylafis, N.D., Papamastorakis, J., Paleologou, E.V. & Haerendel, G. 1997a, Astr. Ap., 325, 135

Xilouris, E.M., Alton, P.B., Davies, J.I., Kylafis, N.D., Papamastorakis, J., & Trewhella, M. 1997b, Astr. Ap., 331, 894

Yahil, A., Tammann, G.A., & Sandage, A. 1977, Ap. J., 217, 903

Young, E., Low, F.J., Soifer, B.T., Neugebauer, G., Rowan-Robinson, M., Clegg, P.E., Miley, G., DeJong, T., & Gautier, T.N. 1984, Ap. J., 278, L75

Zabludoff, A.I. & Zaritsky, D. 1995, Ap. J. (Letters), 447, L21

Zehavi, I., Riess, A.G., Kirshner, R.P., & Dekel, A. 1998, astro-ph/9802252